Micromagnetic Modeling and Demonstration of Wide Bandwidth and Ultralow Power Skyrmion-based Spintronic Devices and Circuits

By

Arash Mousavi Cheghabouri

A Dissertation Submitted to the Graduate School of Sciences and Engineering in Partial Fulfillment of the Requirements for the Degree of

Doctor of Philosophy

in

Electrical and Electronics Engineering

KOÇ ÜNİVERSİTESİ

Aug 14, 2023

Micromagnetic Modeling and Demonstration of Wide Bandwidth and Ultralow Power Skyrmion-based Spintronic Devices and Circuits

Koç University

Graduate School of Sciences and Engineering

This is to certify that I have examined this copy of a doctoral dissertation by

Arash Mousavi Cheghabouri

and have found that it is complete and satisfactory in all respects, and that any and all revisions required by the final examining committee have been made.

Committee Members:

____

Asst. Prof. Mehmet Cengiz Onbaşlı (Advisor)

____

Prof. Hakan Ürey

____

Prof. Özhan Özatay

____

Asst. Prof. Talip Serkan Kasırga

____

Asst. Prof. Murat Kuşcu

Date: ____

ABSTRACT

Micromagnetic Modeling and Demonstration of Wide Bandwidth and Ultralow Power Skyrmion-based Spintronic Devices and Circuits

Arash Mousavi Cheghabouri
Doctor of Philosophy in Electrical and Electronics Engineering
June 23, 2023

The scaling of microelectronics faces two major issues: memory bottleneck and power consumption. These issues prompted the proposal of in-memory computation that encodes information in spins. Using spins allows for nonvolatile logic and data manipulation functionalities. Skyrmions, which are nanoscale, topologically protected, chiral and surface spin textures, could be used for these functions. Skyrmions can be driven by charge or spin currents and have stability against stray magnetic fields and thermal noise. Using magnetic films that stabilize skyrmions might reduce the power consumption with respect to conventional microelectronics by several orders of magnitude. Despite the progress in experimental demonstrations and theoretical studies on skyrmion initialization, detection, and manipulation, using skyrmions for their promising digital logic applications has remained elusive. A set of new device designs based on skyrmion logic processing, and the investigation of their device physics is necessary.

In this thesis, we designed a comprehensive skyrmion logic gate system, which includes a skyrmion clock generator and the essential connecting blocks including the duplicator, junction, and deflector. Then, all the logic gates AND, OR, inverter, NAND, NOR, XOR, and XNOR gates have been designed and their functionalities have been verified using computational micromagnetics. Each block has been investigated thoroughly in terms of their energy consumptions, Joule heating, temporal delay and transient response, bandwidth, cascadability, stability against thermal noise and external magnetic fields as well as functional sensitivity with respect to the geometric (sidewall roughness, notch size/feature, channel width), material (Gilbert damping, non-adiabaticity of spin transfer torques) and temperature variations.

Skyrmions need to be generated and propagated using charge currents for integrated ultra-wideband spintronics. We introduce a device design for initialization and generation of periodic skyrmions from 114 MHz to 21 GHz using spin-polarized direct current. We demonstrate in micromagnetic simulations that skyrmion generation frequencies can be controlled reversibly over more than seven octaves of frequencies by changing DC current density. Thus, a non-volatile current-driven digital clock source has been established.

The inverter can be driven with spin polarized current pulses, operate with wide bandwidth, low energy consumption (~1350 k_BT/bit at room temperature), small footprint (~300 nm), no or very limited need for external magnetic fields, cascadability and room temperature thermal stability owing to substrate's thermal conduction. Using magnetic insulators to eliminate Joule heating hints that the power consumption could be even further reduced by 3-4 orders of magnitude. These analyses suggest that the inverter block could be cascaded and operated as part of digital spintronic circuits without loading or thermal drift effects.

We presented a bit-slice circuit for a digital skyrmion full adder. This circuit could in principle be scaled to larger numbers of bits. As the skyrmion logic circuit designs might be integrated to electronic design automation workflows, a new protocol for the emulation of skyrmion signals with a tiled geometry is devised. The study presents a new comprehensive emulation and simulation software, featuring different elements of micromagnetic modeling, a Python package for automated simulation script development, and a library of block sets. A user-friendly web-based version of the emulator has been developed. The findings presented in this study suggest that skyrmionics has reached a milestone enabling a new area of ultralow power and ultra-wideband digital skyrmionics for in-memory computation.

ÖZETÇE

Geniş Bantlı ve Ultradüşük Güç Tüketen Skyrmion Temelli Spintronik Aygıt ve Devrelerin Mikromanyetik Modellenmesi ve İspatlanması

Arash Mousavi Cheghabouri
Elektrik ve Elektronik Mühendisliği, Doktora
23 Haziran 2023

Mikroelektronik aygıt ölçeklendirme iki ana sorunla karşı karşıyadır: bellek darboğazı ve güç tüketimi. Bu sorunları gidermek amacıyla, bilgiyi spinlere kodlayan bellek içi hesaplama önerildi. Spinlerin kullanılması, bilgiyi depolayan mantık uygulaması ve veri işlemeye izin verir. Nano ölçekli, topolojik olarak korunan, kiral ve yüzey spin yapıları olan Skyrmion'lar bu işlevler için kullanılabilir. Skyrmion'lar, yük veya spin akımlarıyla çalıştırılabilir ve dış manyetik alan gürültülerine ve termal gürültüye karşı kararlıdır. Skyrmion'ları stabilize eden manyetik filmler kullanılarak, geleneksel mikroelektroniğe göre güç tüketimi on binlerce kata kadar azaltılabilir. Skyrmion başlatma, algılama ve manipülasyona ilişkin deneysel çalışmalar ve teorik araştırmalardaki ilerlemeye rağmen, skyrmion'ları gelecek vaat eden dijital mantık uygulamaları için kullanmak bugüne kadar gösterilememiştir. Skyrmion mantık işlemeye dayalı yeni cihaz tasarımları ve bunların cihaz fiziğinin araştırılması gereklidir.

Bu tezde, bir skyrmion saat üreteci ve çoğaltıcı, bağlantı ve saptırıcı gibi temel bağlantı bloklarını içeren kapsamlı bir skyrmion mantık devresi sistemi tasarladık. Daha sonra AND, OR, inverter, NAND, NOR, XOR ve XNOR kapılarının tüm mantık devreleri tasarlanmış ve hesaplamalı mikromanyetik ile işlevsellikleri doğrulanmıştır. Her bir blok; enerji tüketimleri, Joule ısınması, gecikme, bant genişliği, basamaklandırılabilirlik, termal gürültüye ve harici manyetik alanlara karşı kararlılık ve ayrıca işlevsel hassasiyetleri geometrik (yan duvar pürüzlülüğü, çentik boyutu, kanal genişliği), malzeme (Gilbert sönümleme, spin transfer torklarının adyabatiksizliği) ve sıcaklık değişkenlikleri açısından kapsamlı incelenmiştir.

Tümleşik ultra geniş bant spintronik devreler için, skyrmion'ların yük akımları ile üretilmesi ve ilerletilebilmesi gerekir. Spin-polarize doğru akım kullanarak 114 MHz'den 21 GHz'e kadar periyodik skyrmion'lar oluşturmak için bir skyrmion başlatma ve kontrollü üretim aygıtı sunuyoruz. Mikromanyetik simülasyonlarda, skyrmion üretim frekanslarının, DC akım yoğunluğunu değiştirerek yedi oktavdan fazla frekans üzerinden tersinir olarak kontrol edilebileceğini gösteriyoruz. Böylece kalıcı ve akımla çalışan bir dijital kaynak hazırlanmıştır.

İnvertör, spin polarize akım darbeleriyle sürülebilir, geniş bant, düşük enerji tüketimi (oda sıcaklığında ~1350 k_BT/bit), az yer kaplama (~300 nm), dış manyetik alanlara ihtiyaç duymaması, basamaklandırılabilirlik ve alttaşın termal iletimi sayesinde oda sıcaklığında termal kararlılık gösterilmiştir. Joule ısıtmasını ortadan kaldırmak için manyetik yalıtkanların kullanılması, güç tüketiminin 1000 ila 10000 kat daha azaltılabileceğine dair ipuçları verir. Bu analizler, invertör bloğunun, yüklenme veya termal sürüklenme etkileri olmaksızın daha büyük dijital spintronik devrelerde kullanılabileceğini göstermektedir.

Dijital bir toplayıcı devresi için bir bit dilim devresi sunulmaktadır. Bu devre prensipte daha fazla sayıda bit için ölçeklendirilebilir. Bu skyrmion mantık devresi tasarımları, elektronik tasarım otomasyon iş akışlarına entegre edilebileceğinden, skyrmion sinyallerinin döşemeli bir geometri ile emülasyonu için yeni bir protokol tasarlanmıştır. Çalışma, mikromanyetik modellemenin farklı öğelerini, otomatik simülasyon komut dosyası geliştirme için bir Python paketini ve bir blok kümeleri kitaplığını içeren kapsamlı bir emülatör, simülasyon yazılımı ve emülatörün kullanıcı dostu web tabanlı bir sürümü geliştirilmiş ve sunulmuştur.

Bu çalışmada elde edilen bulgular, skyrmionların bellek içi hesaplama için yeni bir ultra düşük güç ve ultra geniş bantlı dijital skyrmion uygulamalarının önünü açan bir dönüm noktasına ulaştığını göstermektedir.

ACKNOWLEDGMENTS

This PhD research has been funded by the following project grants and institutions:

a. TÜBA-GEBİP Award in 2019 by the Turkish Academy of National Sciences
b. TÜBİTAK Grant No. 120F230,
c. European Research Council (ERC) Starting Grant SKYNOLIMIT No. 948063.
d. ERC Proof of Concept Project SuperPHOTON No. 101100718.
e. Huawei Fellowship (2019-2023).

TABLE OF CONTENTS

LIST OF TABLES

LIST OF FIGURES

ABBREVIATIONS

STT	Spin Transfer Torque
SHE	Spin Hall Effect
PMA	Perpendicular Magnetic Anisotropy
DMI	Dzyaloshinskii-Moriya Interaction
SOT	Spin-Orbit Torque
LLG	Landau-Lifshitz-Gilbert equation
FPGA	Field Programmable Gate Array
FM	Ferromagnetic Material
AFM	Antiferromagnet
SAF	Synthetic Antiferromagnet
HM	Heavy Metal
DW	Domain Wall
VCMA	Voltage Controlled Magnetic Anisotropy

SYMBOLS

$\underline{\boldsymbol{H}}$	Magnetic field intensity (A/m)
$\boldsymbol{B}$	Magnetic flux density (T: (Kg s^2)/A)
$\boldsymbol{M}$	Magnetization (A/m)
$\boldsymbol{I}$	Electric current (A)
J	Electric current density (A/m^2)
Q	Electric charge (Coulombs: As)
$\boldsymbol{\mu}$	Magnetic moment (A m2)
χ	Magnetic susceptibility (dimensionless)
δ_{ij}	Kronecker Delta Function ($= 1$ if $i = j$, and $= 0$ if $i \neq j$)
$\hbar$	Planck's constant (= 1.0546×10^{-34} J s)
A_{ex}	Heisenberg Exchange(J/m)

Chapter 1

INTRODUCTION

1.1 Background and Motivation

The Moore's Law, which guided the microelectronics industry and its device scaling over the past half century, is now starting to break down due to the limitations caused by quantum effects like leakage current and high power dissipation density [1, 2]. Thus, there is a growing interest in finding alternative or supplementary technologies to complementary metal-oxide-semiconductor (CMOS), the state-of-the-art technology of the modern computers. Spintronics, particularly the topological spin textures of magnetic skyrmions, has gained a lot of attention as a potential solution since 2000s [3].

A major step of spintronics that boosted the research into magnetic texture memory and logic was the Giant Magnetoresistance (GMR) reported by Albert Fert and Peter Grünberg [4]. GMR consists of a large change in electrical resistance in response to a magnetic field in a thin-film structure composed of two ferromagnetic layers separated by a non-magnetic layer. GMR has been used in the development of spintronic devices, such as read heads for hard disk drives. The discovery of GMR led to the awarding of the Nobel Prize in Physics in 2007.

Skyrmions are topologically protected magnetic structures that exhibit many advantageous properties for computing. They are non-volatile, they require low energy and can reach high speeds [5]. These merits make them suitable for use in logic gates, memory elements, and other computing components. Furthermore, skyrmions can be generated and manipulated using spin polarized electric currents, allowing integration with conventional electronics.

The potential of skyrmionic logic is not limited to traditional computing applications but extends to other fields, such as neuromorphic computing, where skyrmions can be used as artificial neurons. Moreover, skyrmionic logic can also enable the development of energy-efficient and robust computing systems, which are crucial for the growing demand for data-intensive applications.

The use of moving magnetic textures for information processing and memory roots back to magnetic bubble RAM. Magnetic bubble RAM was developed in the

1970s and 1980s. It utilized magnetic bubbles and magnetic fields to store and manipulate data [6-8]. The bubbles were created and moved by magnetic fields. Magnetic bubble memory once considered a promising alternative to semiconductor-based memory technologies was eventually superseded by other technologies like flash memory, which offered even higher densities and faster access times.

Bubble memory's primary weakness lied in its requirement for an external magnetic field, which significantly limited its density and scalability. However, magnetic skyrmions can be created in thin films and ferromagnetic bulks without the need for an external magnetic field, as they can be stabilized by DMI and anisotropy effects. Additionally, magnetic skyrmions are typically much smaller than magnetic bubbles, with sizes down to several nanometers, making a skyrmion-based memory capable of higher storage density. Electric current or an electric field can manipulate magnetic skyrmions, which is more efficient than applying an external magnetic field. These features make skyrmions much more promising than magnetic bubbles for future electronic applications.

The shortcoming of the current electronics is the high energy consumption and leakage currents, the volatility of the memory and logic signals, and the lower memory bandwidth of the von-Neumann architecture that can be mitigated by replacing the current architecture with in-memory computation schemes that embed non-volatile elements. Using skyrmions as non-volatile signals can lead to in-memory computation schemes. Furthermore, their nanometer sizes and topological protection lead to higher storage density and signal propagation density, thus improving the temporal and spatial bandwidth. While most of the literature emphasizes these benefits and some studies present logic gates based on skyrmions, a comprehensive system for making arbitrary logic operation is yet to be shown.

This study presents the modular design, emulation software and micromagnetic modeling of an extensive skyrmionics logic system. As skyrmionics logic is still in its beginning steps and a scalable logic system is missing, presenting such a system is a required stage for the next steps of the skyrmionics. Moreover, presenting experimental demonstration of the modules and systems is very challenging with the current technology and beyond the scope of a Ph.D. thesis. Since micromagnetic modeling has proven accurate as experimental studies have confirmed, we use micromagnetics to model our system. To have a more accurate modeling, we consider the finite temperature effects and spatial or parameter noises in our designs too. Micromagnetic modelling allows for systematic computational investigations of different material, geometric and external bias conditions that would not otherwise be feasible (or could take much longer time) in experiments.

In this chapter, we first go through the literature leading up to and beyond the start of this work. The chronological order of the developments in the field of skyrmionics are discussed. The studies with a similar scope and goal are then discussed and the differences and shortcomings of the existing studies along with the solution of this thesis are presented.

1.2 Thesis Question and the Literature Review

The thesis question is: Can skyrmions be used to construct non-volatile, ultralow power and ultra-wideband digital logic elements and circuits with topological protection? The hypothesis of the thesis is that "Using an appropriate device geometry, confinement, and current pulse profile, arbitrary skyrmion logic and digital device functionality can be achieved."

The main topic of this thesis is the design of a scalable and a universal skyrmion logic system. We will break down the problem by using a modular design. The endeavors of this thesis constitute three main parts: block design, emulation software, and simulation management software. Through these endeavors we answer the question of whether a modular skyrmionics system can be designed, emulated, and tested easily using existing micromagnetic software. To have a firmer grasp on the subject, a literature review is necessary. Here we go through the existing literature. Some of the studies in this literature review are published during and after the results of this thesis were finalized. The results of this thesis are novel after considering these studies too.

The first theoretical description of magnetic skyrmions was proposed by Bogdanov et al. in 1989 [9]. The capability of Dzyaloshinski-Moriya Interaction (DMI) for skyrmion stabilization was then proposed in theory for multilayers in 2001 [10] and for the bulk materials in 2006 [11]. These theoretical predictions along with the experimental demonstration of skyrmions in bulk MnSi using small-angle neutron scattering (SANS) in 2009 [12] and the real-space imaging of skyrmion lattices in FeCoSi using Lorentz transmission electron microscopy (LTEM) [13] triggered intensive research into the application of skyrmions for technological use. Later on, the observation of the current driven motion of skyrmions in room or near-room temperature added to the interest of the field of skyrmionics [14, 15]. These current induced motions of skyrmions or their ensembles were also established by computational micromagnetic studies [16].

Using spin-polarized currents as driving stimulus is not exclusive to skyrmions and has been used for the magnetic domain walls before it was used for skyrmions. Since this work also contains the domain wall motion and dynamics, we first review the studies related with domain wall dynamics and uses.

1.2.1 Propagation of Magnetic Domain Walls by Spin Polarized Current

Magnetic domain walls are boundaries between regions in a magnetic material where the magnetization direction changes from one domain to another. Domains, consist of groups of atoms with similar magnetization direction. The existence of magnetic domain walls minimizes the thermodynamic energy of the system. Magnetic domain walls can be displaced by means of external magnetic fields or spin-polarized currents.

The magnetic domain-wall motion due to in-plane electric current in metals with large Hall angle was proposed by L. Berger in 1974 [17]. This study explored the impact of uneven current distribution near a wall in metals with large Hall angle such as cobalt and nickel. The research considered the extremes of very low and very high Hall angles using both the Williams, Shockley, and Kittel single-wall model, as well as Herring's stratified medium model. Later on, the domain wall motion was experimentally studied for Néel walls in ferromagnetic alloys such as $Ni_{81}Fe_{19}$ [18]. This demonstrated that the movement of walls in films was not the result of stray magnetic fields, but rather the s-d exchange forces produced by conduction electrons. The wall displacement was also later shown for Bloch type domain walls in the same ferromagnetic alloy [19]. The mechanism for domain wall motion by vertical spin current was also later proposed by Slonczewski [20].

The study of the spin polarized motion of domain walls took off in late 1990s and early 2000s [21-30]. Although the experiments confirmed this motion, theoretical description and prediction was necessary. Micromagnetic framework rendered a reliable modeling approach this prediction and description [31, 32]. The higher stability and current-driven motion of Dzyaloshinskii-Moriya domain walls, which are the domain walls that exist in media with Dzyaloshinskii-Moriya Interaction was also emphasized in some studies [33-35].

1.2.2 Domain Wall Logic and Memory

The electric current induced motion, lower energy, non-volatility, and integrability of domain walls with the MRAM technology made them interesting for memory and logic operations. In one of the early experimental studies a NOT gate and a shift register were implemented with magnetic domain walls [36]. Another study used sub-micron planar magnetic wires to perform NOT and AND gates with domain walls [37]. Later on a magnetic domain wall memory based on horizontal or vertical nano-wires on silicon chip was also proposed [38]. The idea of using perpendicular magnetic anisotropy to mitigate the effects of random noise in platinum/cobalt/platinum films by producing unidirectional domain wall motion was also proposed 2012 [39]. A recent study also uses the chirality of Dzyaloshinskii-Moriya domain walls to perform the Boolean operations first by providing an inverter gate and then producing AND and NAND gates [40].

1.2.3 Early Skyrmionics

While the domain wall memory and logic research was enjoying great interest, the study of skyrmions became popular in 2000s. Magnetic skyrmions were studied before and the effects of their topological properties such as the topological charge on their dynamics were already known and modeled [41, 42] while an experimental demonstration of magnetic skyrmions was lacking. Skyrmions once thought to not to form spontaneously were shown theoretically to have spontaneous existence in certain non-centrosymmetric materials in 2006 [11]. The observation of a skyrmion lattice in MnSi by small angle neutron scattering bolstered the position of skyrmions as real objects and boosted their potential [12].

Real space imaging of skyrmions was important to better understand their dynamics. A 2010 study used Lorentz transmission electron microscopy (LTEM) for the real-space observation of skyrmions. This study shed light on the properties of skyrmions and also showed the increased stability and range of parameters in which skyrmions can be stabilized [13]. These studies used external magnetic field for stabilizing skyrmions. Despite the spontaneity of skyrmion lattice was shown in theory, an experimental demonstration of spontaneous skyrmions was yet to be shown. In 2011 another study showed the spontaneous atomic scale skyrmions as the magnetic ground state of a hexagonal Fe film of one-atomic-layer thickness on the Ir(111) surface. This study used spin-polarized scanning tunnelling microscopy for imaging skyrmions [43]. Skyrmions were also observed in near room temperature in FeGe material another study in 2011 [44]. The observation of skyrmions in doped semiconductor $Fe_{1-x}Co_xSi$ in 2010 also increased the range of material parameters where skyrmions could be stabilized [45].

The availability of skyrmions in different materials, their spontaneity, stability in room temperature, and the possibility to move with lower current values than domain walls made them interesting candidates for next generation spintronic logic. Demonstration of the movement of skyrmions in room temperature with ultralow current densities in 2012 [46] and proposition of the effect of emergent electrodynamics of skyrmions on lowering their sensitivity to pinning sites in 2012 [47] further increased their potential for application purposes.

Because of the complexity of skyrmion dynamics, the potentials of using new materials, and the unknown effects of material parameters and geometries, numerical modeling was necessary for more accurate description of skyrmion behavior under different material parameters, stimuli, and geometries. The universal current-velocity equation of motion for skyrmions which rendered independent of the external noises and other non-adiabatic effects was deduced by numerical methods in 2013 [48].

1.2.4 Skyrmion Generation and Dynamics

Although the spontaneous existence of skyrmions and their lattices was established, the generation of single skyrmions with different stimuli was yet to be demonstrated. The first proposal for skyrmion generation using spin polarized current was put forward in 2012 [49]. The publication is based on a micromagnetic modeling study, and it demonstrated that the spin polarized current injected to a chiral ferromagnetic material can produce individual skyrmions. In that study the spin polarized current was perpendicularly injected into ferromagnetic material in a patch with a radius comparable to the skyrmion size. The effects of Gilbert damping and non-adiabaticity of spin transfer torque were studied in the formation process of skyrmions. Figure 1.1 shows different skyrmion shapes created in that study.

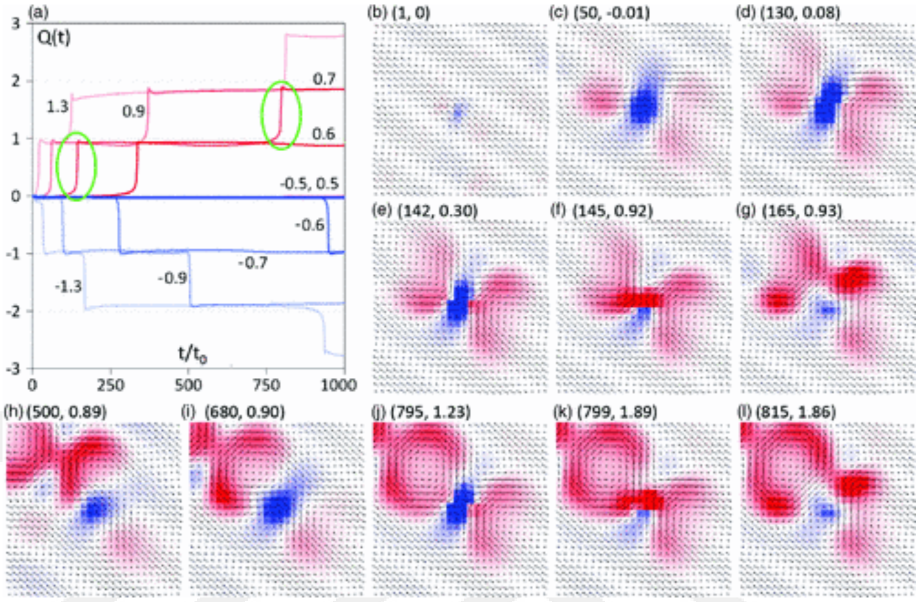

Figure 1.1. Skyrmion generation by circulating spin current. (a) the topological charge of the skyrmion Q(t) for different current values (b)–(l) magnetic configuration of the system for Q = 0 → 1 and Q = 1 → 2 for the green circles of part a (reprinted with permission by APS [49]).

The experimental stability and current-driven motion of near-room temperature skyrmions by ultra-low currents below 100 A cm^{-2} in FeGe, using Lorentz transmission electron microscopy was also shown in 2012 [46]. Another study for room temperature stability and current driven motion of skyrmions in ultrathin Co presented similar results [50]. A 2017 study also shows the room temperature current induced nucleation and motion of skyrmions in $Co_8Zn_9Mn_3$ [51]. Electric field nucleation and annihilation of skyrmions is also shown experimentally in Pt/Co/oxide [52] and Fe on Ir(111) multilayers [53]. Another study from 2016 also shows the creation of skyrmions by means of engineering the uniaxial anisotropy and DMI at room temperature [54]. A 2015 experimental study shows that irregular spins at the rough edges of a nanotrack can generate a chain of skyrmions [55]. Another experimental study that investigates the movement of skyrmions in a non-rectangular geometry provides more insight into the dynamic behavior of skyrmions and ascribes a mass to the skyrmions related to the topological protection of skyrmions [56].

Another micromagnetic paper regarding the creation and movement of skyrmions was published in 2013 [16]. This study demonstrated through numerical investigations that isolated skyrmions can be stable configurations in nanostructures. Additionally, they can be locally nucleated by injecting spin-polarized currents and displaced by current-induced torques, even in the presence of large defects. This paper also explored the movements of a single skyrmion and a chain of skyrmions in thin rectangular films with and without geometric defects. The importance of this highly cited study is the demonstration of different aspects of skyrmions such as creation, stability, and motion in the presence of geometric defects. Figure 1.2 shows a phase diagram from this study that show the current dependence pinning of skyrmions to the triangular notch.

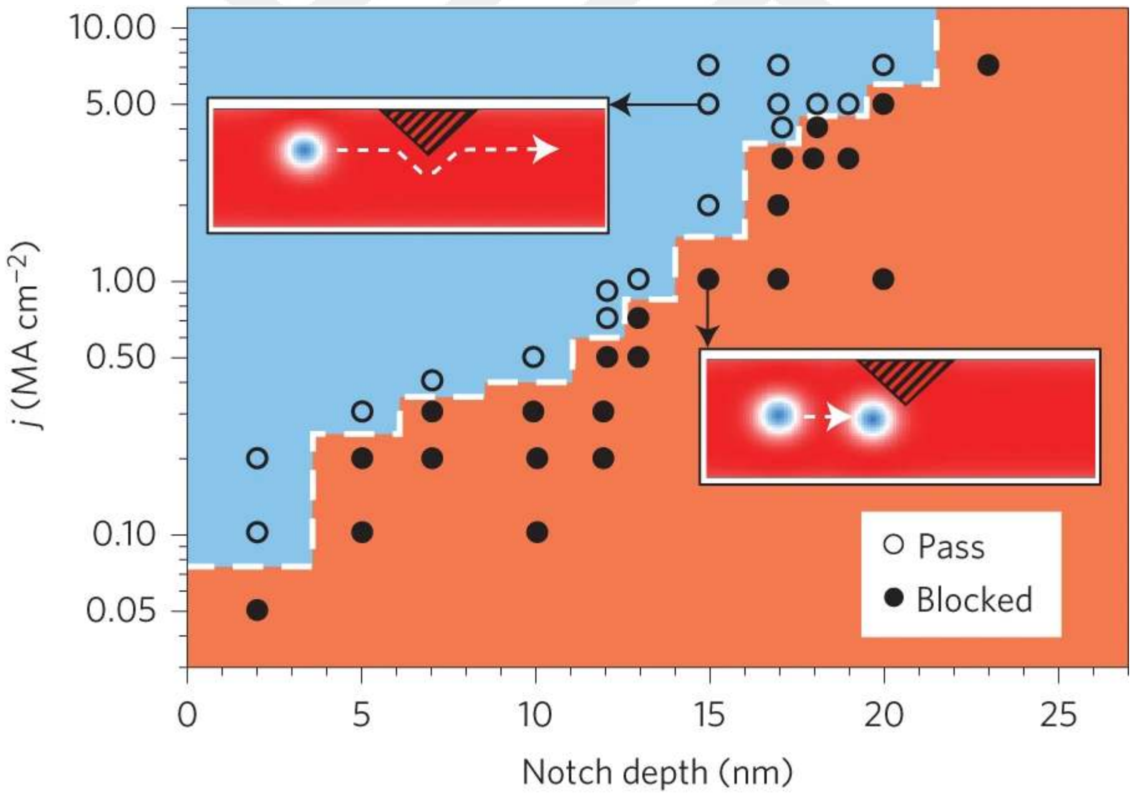

Figure 1.2. Triangular notch effect in skyrmion motion. The triangular notch has a different uniaxial anisotropy (0.8 MJ m^{-3}) than the rest of the track (K = 1.2 MJ m^{-3}) [16].

Because of the high impact of geometry in the skyrmion motion, the next studies focused on the effect of geometry in the creation and motion of skyrmions.

A 2013 micromagnetic modeling paper researched the effect of geometric constrictions in the generation and motion of skyrmions [57]. This study also showed the possibility of skyrmion creation using a rectangular notch in a track. The type and shape of the notch of this study is different from the last study as it is a rectangular indentation in the track rather than a triangular part of the material with different parameters. Figure 1.3 shows the skyrmion generation and motion of this study.

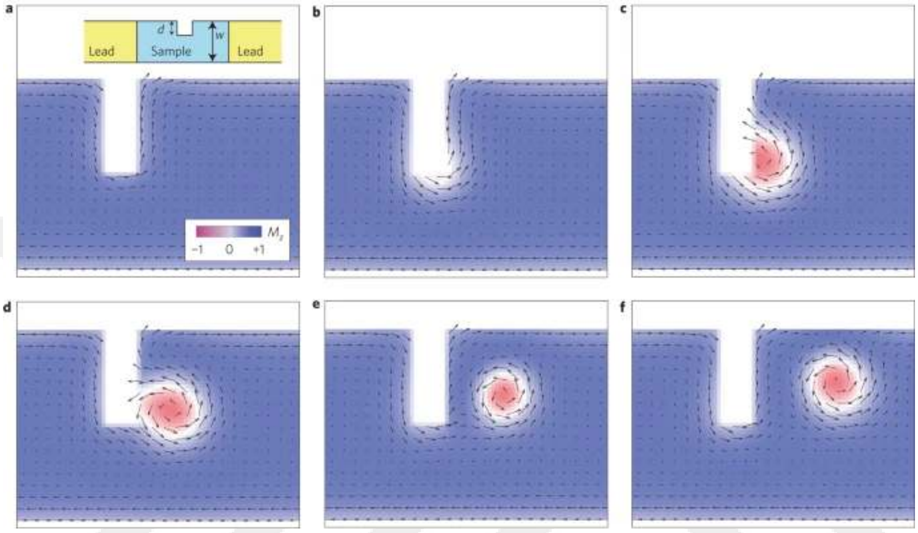

Figure 1.3. Skyrmion generation and movement by spin polarized current. Current density is $j = 3.6 \times 10^{11}$ A m^{-2}. (a), $t = 9.10 \times 10^{-11}$ s (b), $t = 18.89 \times 10^{-11}$ s (c), $t = 28.60 \times 10^{-11}$ s (d), $t = 38.35 \times 10^{-11}$ s (e) and $t = 48.10 \times 10^{-11}$ s (f). Inset of a: The blueprint of the notched track for skyrmion creation [57].

After these studies, the role of spin polarized current in creation of skyrmions was established. But introducing other types of stimuli can also overcome the potential barrier of skyrmion creation. A 2014 study focuses on the local heating and uses micromagnetic modeling to research the possibility to use laser-induced local heating to produce skyrmions. This study showed that local heating is capable of creating individual skyrmions [58]. Another non-geometric skyrmion generation modeling study from 2017 focuses on the changes in local magnetization and uniaxial anisotropy to create skyrmions by flowing DC spin polarized current in a media without DMI [59]. A 2017 experimental and modeling study that presents the generation and motion of skyrmions smaller than 100 nanometers in a media with non-uniform magnetization also provides insights on the physical behavior of skyrmions and confirms the validity of modeling results [60].

The study of skyrmion generation and motion is not limited to single layers of ferromagnets. Antiferromagnets also have been proposed to be able to sustain skyrmions. A modeling study from 2016 shows the potential of antiferromagnets in hosting skyrmions by either injecting a spin-polarized current or a domain for skyrmion conversion [61]. A 2017 experimental and modeling study shows a pair of coupled skyrmions of opposite chiralities in a symmetric magnetic bilayer system by combining DMI and dipolar coupling [55]. A 2018 experimental and modeling study focuses on compensated ferrimagnet thin films of $Pt/Gd_{44}Co_{56}/TaO_x$ to show ~10nm stable room-temperature skyrmions and domain walls with ~ $1.3\ \mathrm{km\,s^{-1}}$ speed[62]. Another 2017 study shows <50 nm room temperature skyrmions in Ir/Fe/Co/Pt multilayer and presents the tuning of skyrmion properties by changing the composition of the magnetic layer [63].

One of the undesirable effects of skyrmion motion is the lateral movement of skyrmion called skyrmion Hall effect (SKHE). SKHE happens because of skyrmion's non-zero topological charge. Thiele described this effect and ascribed it to the precession like term in Landau-Lifshitz-Gilbert (LLG) equation in his 1973 paper [41]. The experimental evidence of SKHE has been presented in 2017 [64]. Different studies have tried to quantize or suggest ways to eliminate or mitigate this effect. A 2016 micromagnetic study suggests the use of synthetic antiferromagnetically coupled bilayers (SAF) to eliminate SKHE as the two skyrmions in stacked layers have opposite deflection directions and attract each other because of the dipolar force. The strong dipolar attraction stops the skyrmion pair from deflecting from the straight line [65]. Other studies show that skyrmions stabilized in antiferromagnetic media do not have SKHE [66]. Later on, the room temperature isolated skyrmions have been shown on SAF layers in 2020 [67].

1.2.5 Skyrmion Interactions and Conversions

The advancements of studies for presenting isolated room temperature skyrmions, their spin-polarized motion and creation, and the effect of materials and geometries on the motion and stabilization of skyrmions led to the next phase of skyrmionics studies. Now skyrmions were being viewed as reliable signal and memory carriers. For skyrmions to be used as real signal carriers, more research was to be done. One of the important aspects of skyrmion manipulation was the ability to convert skyrmions into other types of magnetic textures such as magnetic domains. A 2013 study shows the reversible conversion between skyrmions and magnetic domains [68]. The study found that the track's geometric width is the deciding factor in determining whether the texture is a magnetic domain or a skyrmion. If the width of the track is less than the diameter of the skyrmion, then a magnetic domain is created. However, if it is larger than the diameter, a skyrmion is formed. A magnetic domain from a narrow track pushed into a wider track becomes a skyrmion and a skyrmion pushed into a narrower track becomes a magnetic domain. The conversion is one-to-one and deterministic i.e., it happens for each skyrmion or magnetic domain and exactly one skyrmion/domain is produced for each domain/skyrmion. This study paved the way for skyrmionic logic proposals that use geometry as a deciding factor for performing memory and logic operations. It also bridges between the domain wall devices and skyrmion devices. Figure 1.4 shows the interconversion between skyrmions and magnetic domains.

Figure 1.4.The skyrmion domain conversion in a track with varying width. The domain walls in the narrow left channel turn into skyrmions when move into the wider part and then the skyrmions turn into domains when move to the narrow right channel [68].

While the domain-to-skyrmion conversion was shown with micromagnetic simulations, a later experimental study in 2015 demonstrated the role of a channel constriction in creating skyrmions from larger magnetic textures [69]. This study confirmed the skyrmion generation from bigger domains and the role of geometric constrictions in generation of skyrmions from larger domains. Figure 1.5 shows the skyrmion generation process of this study.

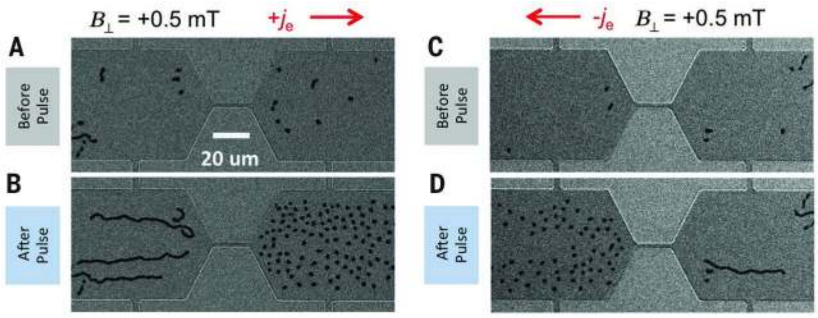

Figure 1.5. Skyrmion generation from larger domain structures. Skyrmions are generated through geometric constriction from larger irregular Sparse domains at a perpendicular magnetic field of $B\perp$=+0.5 with right flowing and left flowing current $j_e = +5 \times 10^5$ A/cm^2 [69]

Another 2016 experimental study suggests the electrical writing and shifting skyrmions with spin polarized current with the difference that skyrmions are produced not from the larger domains but with electrical current [70]. Figure 1.6 shows this scheme.

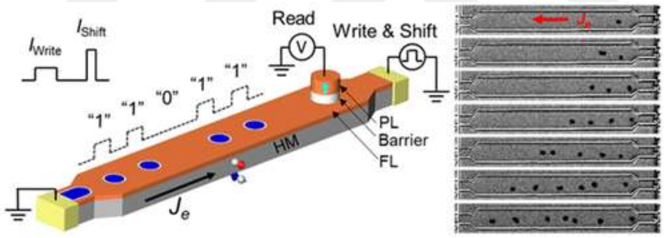

Figure 1.6. The skyrmion nucleation and shift in room temperature. Skyrmions are generated by spin polarized current by the conductive contact at one end and are moved towards the other side where a magnetic tunnel junction reads them [70].

A 2015 micromagnetic modeling explores the interaction between skyrmions and between skyrmions and geometric elements more thoroughly [71]. Since skyrmions repel each other, there is a limit to the density of skyrmions in a racetrack and after reading a skyrmion and when the skyrmion is no longer needed, annihilation is required to make room for the other skyrmions. That study introduces a triangular notch with sharp tip to annihilate skyrmions. Another 2019 study explores the dynamics of skyrmions in nanotubes to eliminate edge effects for researching the behavior of skyrmions in edgeless systems. That study also presents insights about designing non-planar track geometries to host skyrmions[72].

1.2.6 Skyrmion Detection

Skyrmion detection is crucial for feasibility of skyrmionic devices. Although neutron scattering, x-ray microscopy, and Lorentz transmission electron microscopy have been used to image skyrmions in different media, a fast and reliable method for skyrmion detection technique must be present for the skyrmionics technology to realize. A 2016 study proposes the purely electrical detection for skyrmions by measuring Hall conductance of a racetrack with finite width [73]. The perpendicular resistance as the change in the magnetoresistance in presence/absence of skyrmions has also been proposed in 2015 [74]. An electrical detection of <100 nm skyrmions combining magnetic force microscopy (MFM) and Hall resistance measurements is shown in a 2018 experimental study [75]. Nano-SQUID techniques could also be used for skyrmion detection.

1.2.7 Skyrmion Applications for Memory and Logic

After the realization of isolated skyrmions, their generation proposals, and exploration of their interaction, movement, and detection, the question of their technological use cases was up for answers. Since bubble memory and logic and domain wall memory and logic were presented before, the use of skyrmions for memory and logic operations was attracting attention. One of the first proposals of using skyrmionics logic was a 2015 paper by Zhang et al. This paper introduces the notion of AND, OR and DUPLICATOR gates. Figure 1.7 shows the AND gate of this study [76]. Although the paper also proposes a NOT gate, the fact that the type of skyrmion changes after passing through the NOT gate, makes is not possible to use the NOT gate in this study along with the other gates presented. Also, the geometric designs of the gates do not possess proper symmetries for cascadability of the gates. The synchronization of the inputs for the AND gate is also another limiting aspect of this study. Figure 1.7 shows the AND gate of this study.

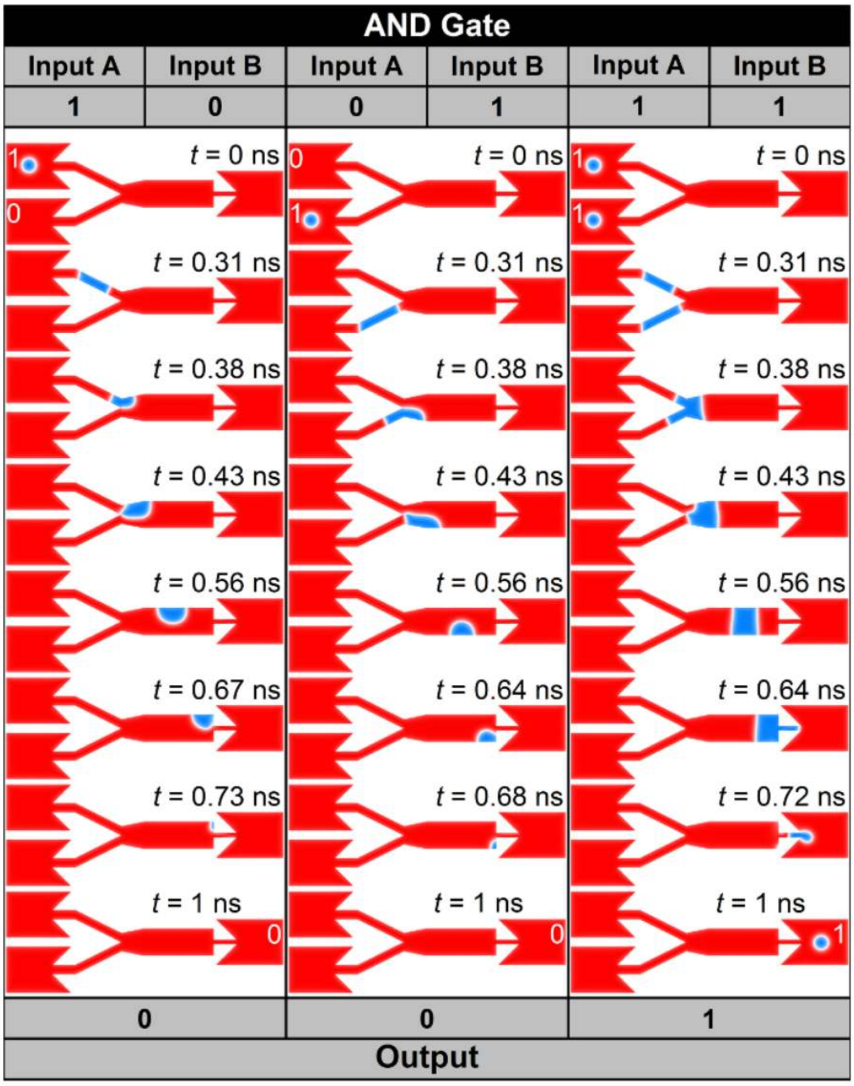

Figure 1.7. Skyrmionics AND gate. Two skyrmions can enter from the left side of the gate. If both skyrmions enter synchronously they can make a domain wall in the middle wider channel. If domain wall forms in the middle, a skyrmion can exit from the output of the gate at the right side. This means that the output is “1” and otherwise “0” [76].

A 2016 study introduces the concept of domain wall gating for skyrmionics logic [77]. In this study the domain wall is used as the logic input and the skyrmion is used as the probing signal. The domain wall is injected by an MTJ. The fact that the domain wall is injected by electrical means undermines the usability of skyrmions as data signals. This study does not provide cascadability and the use of electrical signals are crucial as the domain walls are injected by electric current. Figure 1.8 shows the gating of a skyrmion by a domain wall in this study. A 2017 majority gate is also proposed on the similar principles of this this study [78].

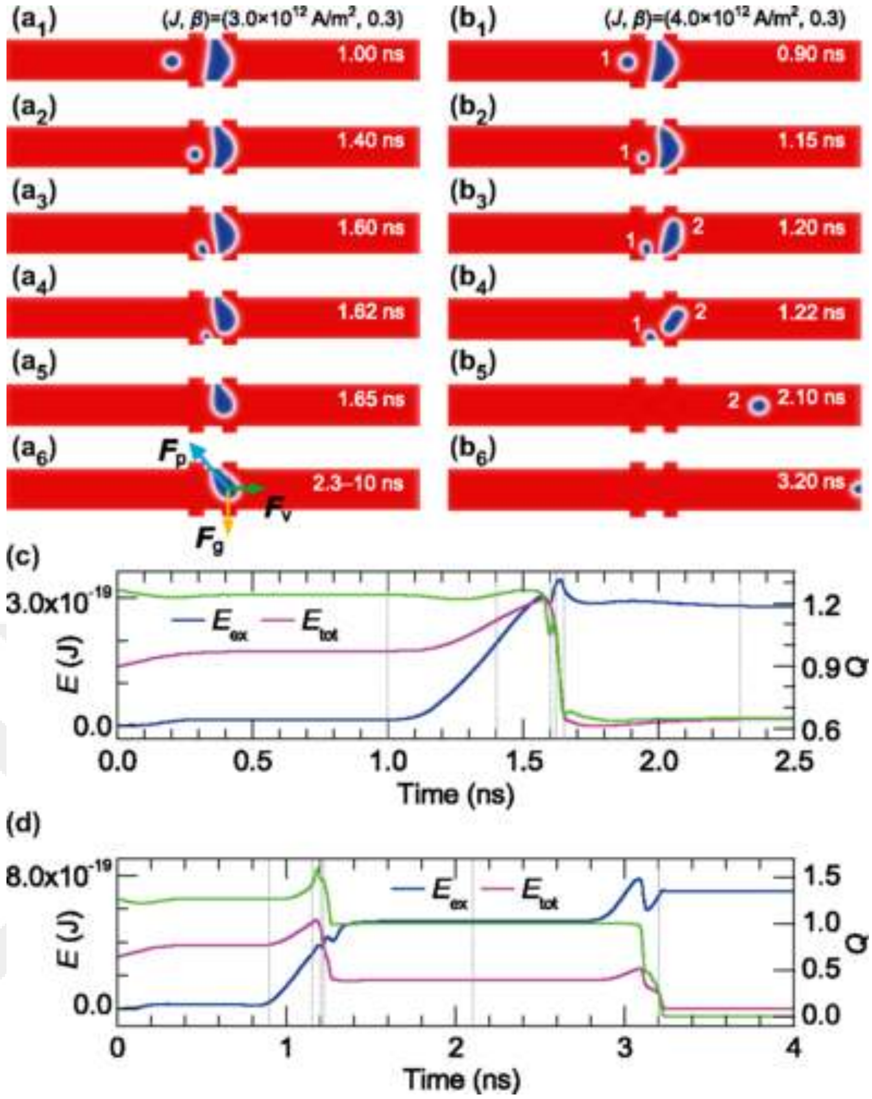

Figure 1.8. Domain wall gated skyrmion. The existence of a domain wall in the notched area of the track can prevent the motion of the skyrmion. Thus, this gate is a NOT gate if the skyrmion is always present (reprinted with permission by APS [77]).

A change in material parameters specially the perpendicular magnetic anisotropy (PMA) can hinder the motion of skyrmions. The perpendicular magnetic anisotropy can change by applying a perpendicular electric field. This effect is called voltage controlled magnetic anisotropy (VCMA). VCMA has been proposed for use in memory and logic operations. One 2016 study suggests using VCMA to gate the skyrmion motion. According to this study an abrupt increase in the PMA produces an energy barrier that in turn increases the current density required to push the skyrmion from the barrier. When using a constant current density, the increase in the PMA stops the skyrmion from moving forward [66]. Figure 1.9 shows the suggested gate for the voltage controlled skyrmion motion.

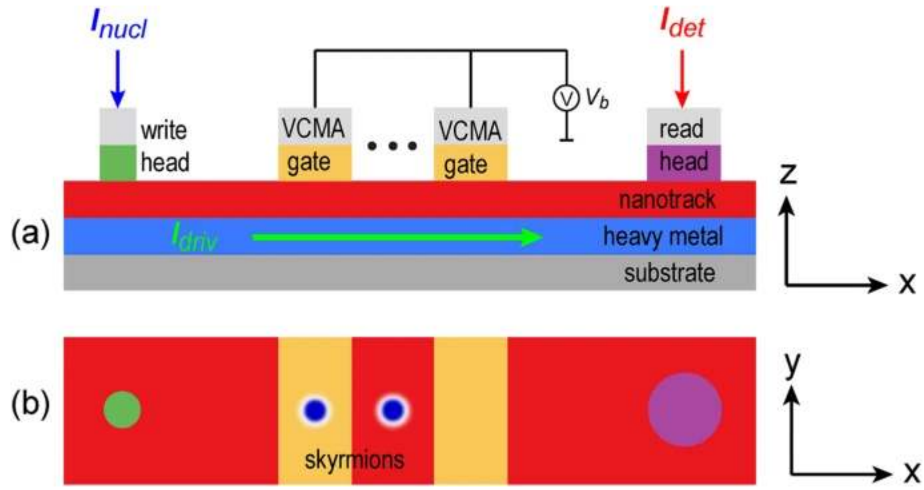

Figure 1.9.The geometry and components of the voltage gated skyrmion track. The voltage applied to the VCMA gates increases the current requirement for the motion of skyrmions [66].

The change in PMA also have been suggested for the skyrmion motion in a study in 2018. In this modeling study a VCMA gradient is shown to be able to move skyrmions [79].

Since the control of skyrmions with the VCMA is straightforward, the use of VCMA is expected to be suggested for logic operations. Another 2019 modeling study suggests the use of VCMA for making different logic gates. The study is composed of VCMA patches with different angles and configurations on the track for making different logic gates. Different contacts are activated together to produce different logic operations [80]. A 2021 study also proposes the role of VCMA hinderance in skyrmion motion for the synchronization of skyrmion in skyrmionics logic gates [81].

A 2018 study uses VCMA, SKHE and skyrmion repulsion to make reconfigurable skyrmion logic gates [82]. In this study the reading magnetic tunnel junction (MTJ) is configured to interpret a skyrmion as either '0' or '1' and thus each gate is its complemented logic gate too i.e., by changing the signal interpretation AND gate can be read as a NAND gate and OR gate can be read as a NOR gate. Figure 1.10 shows one of the reconfigurable gates of this study. No cascadability is shown in the device and sharp synchronization is needed for the operation. The fact that the Boolean complement is produced by interpretation of the skyrmion signal and not by annihilation of skyrmions highly compromises the device scalability as a cascaded NOT gate is not present.

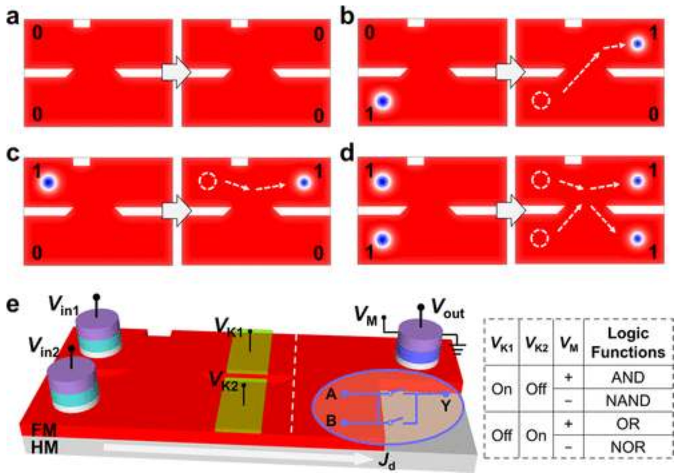

Figure 1.10. Reconfigurable skyrmion logic gates. The VCMA patches produce energy barriers to make AND and OR gates. The reading MTJ can be configured to read the presence of a skyrmion by as either "1" or "0". This makes the complement gates[82].

A 2019 study provides a scheme for different Boolean logic functions utilizing SKHE and skyrmion repulsion [83]. In this study synchronized skyrmions move in parallel tracks with merging crosses at specified points. When a skyrmion reaches the merger track, it deflects to the adjacent track if there is not a skyrmion there. On the other hand, if a skyrmion exists at the adjacent track, it is shifted to the track left of it. The initial skyrmion continues its course of motion. Figure 1.11 shows this process.

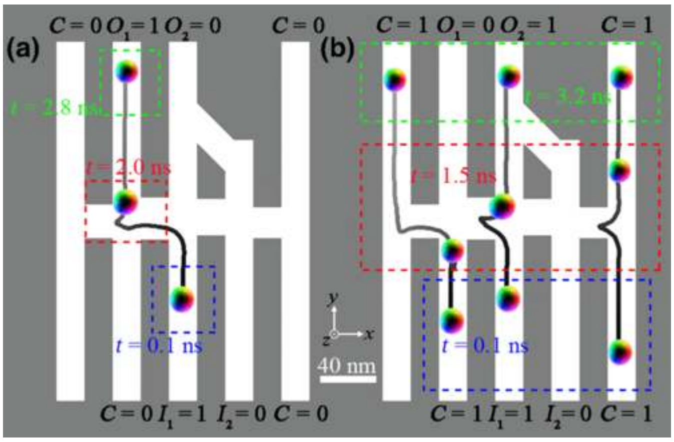

Figure 1.11. Skyrmion gate based on track change. The track change of skyrmions with and without the existence of a skyrmion at the adjacent track (reprinted with permission by APS [83]).

A 2021 study uses the same principles of SKHE and geometric notches to annihilate skyrmions to produce logic operations. This study offers a half-adder and a full adder for the operation. The working principle of the offered device is utilizing SKHE and skyrmion repulsion for driving skyrmions towards triangular notches that destroy them [84]. Figure 1.12 shows this device. If the skyrmion is present in the top input channel, it can move past the triangular notch and reach the SUM output. If the skyrmion is present in the bottom input channel, the SKHE drives the skyrmion to the SUM channel and if both input channels have skyrmions, the repulsion between skyrmions pushes the top skyrmion into the triangular notch and annihilates it and prevents the bottom skyrmion to move to the SUM output. Two main limitation of this study is the need for sharp synchronization of skyrmions and the dependence on SKHE. This dependence means that with changes in non-adiabatic spin transfer torque, the operation of the device might be compromised. There is also no demonstration for arbitrary gates, no cascadability and no fan-out elements in this study.

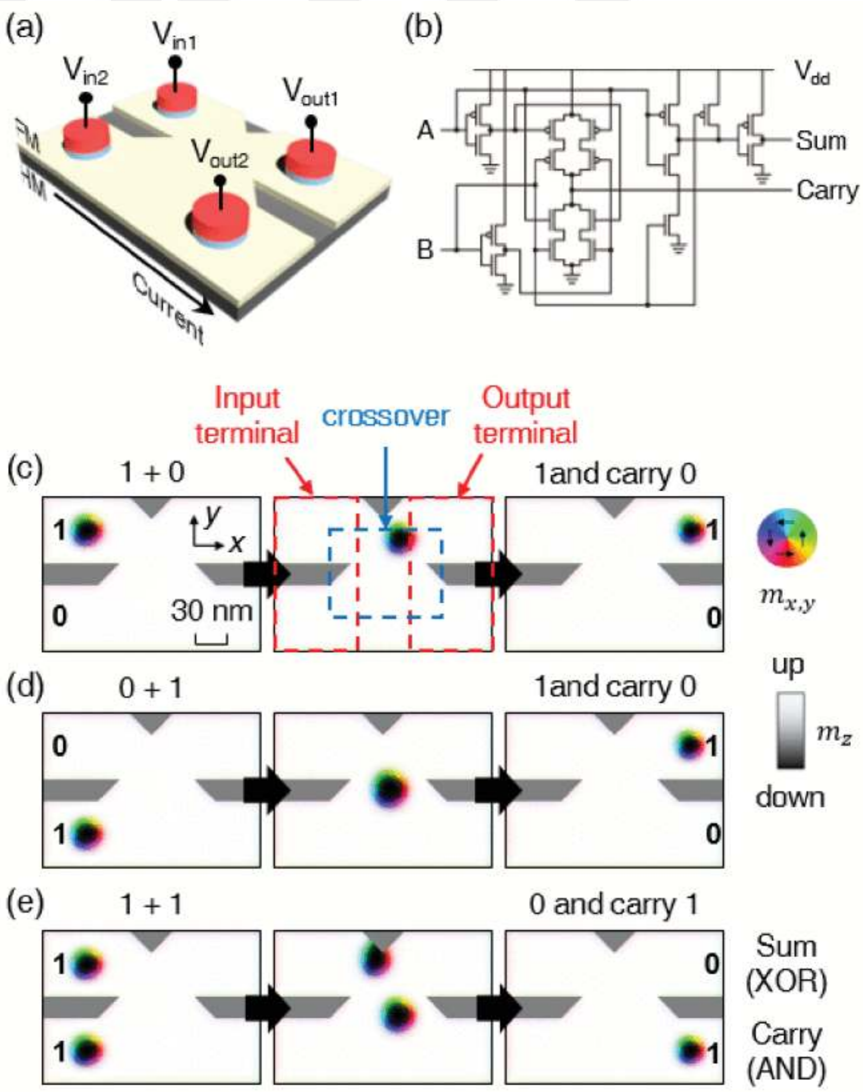

Figure 1.12. Full adder based on skyrmion annihilation. (a) shows the

device geometry and electrical interface. (b) shows the equivalent CMOS circuitry. (c-e) show the full adder operation with different inputs. The SKHE is important for the part (d) and the skyrmion repulsion is important for the functioning of part (e) [84]

Non-Boolean computational applications of skyrmions

A discussion about the logic and computation applications of skyrmions is not complete without touching other areas of their application in computation such as neuromorphic computation. A 2017 study proposes the gradient of perpendicular magnetic anisotropy for a spring-like motion of skyrmions which mimics the “leaky-integrate” behavior of biological neurons [85]. Another 2017 study proposes VCMA to bring an energy barrier potential to the moving skyrmions. The combination of the applied current and the VCMA strength to control the accumulation of skyrmions in one side of the track can potentially mimic the behavior of biological neurons [86]. The non-linear impact of a skyrmion on anisotropic magnetoresistance have been proposed for reservoir computing in 2018 [87]. A 2020 study also proposes the current induced accumulation of skyrmions as synapse weights and shows by simulation that this interpretation can lead to pattern recognition [88].

Antiferromagnetic skyrmionics logic

Antiferromagnetic materials present attractive opportunities for skyrmion devices such as higher speed, zero stray field, and elimination of SKHE. The design principles for antiferromagnetic skyrmion devices are like their ferromagnetic counterpart. A 2021 micromagnetic modeling study proposes skyrmionic gates based on antiferromagnetic materials. The study utilizes the VCMA, skyrmion-skyrmion repulsion and skyrmion-edge repulsion for the design [89]. Because of the role of exchange length in the validity of micromagnetic modeling, the results of the micromagnetic models for antiferromagnet materials need to be taken with more caution.

Summary of skyrmion logic gate proposals

Skyrmion logic gate proposals in the literature are diverse and innovative. Each of them solves problems that help pushing forward the skyrmion logic towards technology realization. While these innovations are important, still a system for skyrmionics logic is missing. As we have seen earlier, these studies look at the specific gates and solve the problem for these gates, but a systematic approach is missing. One requirement is the skyrmion clock source. The other requirement is the cascadable gate designs. Another requirement is the minimum number of spin-to-charge current conversion steps (or vice versa) to minimize power dissipation and interconversion inefficiencies. A systematic approach needs customized software tools for design and test. While the micromagnetic simulation software are comprehensive and accurate in solving the simulation problem, meta-software tools for scaling and automation of the simulation geometries and scripts are missing. This prevents the researchers of the skyrmionics whom most of which are from non-computer science background to go beyond the gate level proposals.

Since there is a lack of systemic view in the skyrmionics literature, each of the studies lack some aspects that prevents them from scaling. For example, [76] lacks the universality of Boolean operation. Ref. [82] can be universal but since the universality is only achieved by changing the interpretation of skyrmion existence from ‘1’ to ‘0’, a cascaded version of the gates will not be able to achieve universality. Other studies that only show a full adder which is a very valuable component of logic signals also lack the universality aspect.

Some studies rely on electrical signals as logic signals. For example the gating domain wall in [78] must be nucleated by electric current. All the studies that use VCMA gating for skyrmions such as [66] also have this issue. Without taking the geometric possibility of cascading the gates, an output of a gate needs to be read, interpreted, and then injected to the other gate by electrical means. This requires the peripheral technology for interconversion and nucleation of magnetic textures or VCMA signals.

Another issue with some of the proposals such as [77] and [84] is their reliance on SKHE. This means that these gates cannot be implemented on antiferromagnetic, synthetic antiferromagnets, or ferrimagnetic materials. Moreover, since SKHE is highly dependent on the non-adiabatic spin transfer torque which might change with material type. Thus, this highly limits the material choices for these gates.

The need for synchronization of skyrmions in many studies such as [76], [77], [82], [84] also limits their scalability and synchronizers are required when using these gates in cascade.

Specifications for a scalable skyrmionics logic

A scalable skyrmionics logic should be composed of modules that can be cascaded easily. This ease of cascading necessitates geometric symmetries and independence of operations between modules (i.e., loading) such that the activation of different modules does not hinder the operation of the subsequent gates. One other important aspect of such a system is the software for design, emulation, and simulation of such system. Without this software, the claims of scalability would not be reliable, and the design and verification will become exponentially difficult for larger systems.

The separation of duty between skyrmion signals and electric signals is necessary for a fully skyrmionic system. The electric signals should only be used to nucleate initial skyrmions and the rest of the operation for the system until skyrmion detection must be mostly independent from electric charge current signals. In other words, the drive of the system must be the injected spin-polarized current but the timing of the pulses of this current must be independent from the skyrmion content of the system. The electric signals must be unaware of the existence of skyrmions, the application of current pulses must not change based on the inputs. This is the difference between the VCMA controlled logic gates or current induced domain wall gating studies and the system that this thesis provides.

1.3 Contributions of This Thesis

While this thesis is an electrical engineering thesis, the focus of the work covers both the engineering and the scientific aspects of the area. In this work first, the logic gates are designed based on physical principles of magnetism and skyrmion. For finding the material window of successful operation of the devices, a software for organizing and running batches of simulations is developed. Then, the scalability, testing and design of the logic gates are carried out. This stage needs two other software. First, the concatenation and simulation maker software are designed. Since the micromagnetic simulations have high computational complexity, an emulator software for prediction the behavior of the designed gates is essential. This software is also developed in this thesis.

1.3.1 Journal Papers

As of June 2023, two journal papers are published in this thesis. The first journal paper is devoted to the periodic generation of skyrmions with DC current [90]. This paper is published in Scientific Reports journal in 2019. Chapter 3 of this thesis is based on this publication. The skyrmionics INVERTER gate as an important part of this thesis. A journal paper about this gate is published in Physical Review B journal [91] in 2022. Chapter 4 of this thesis is based on this publication. Besides these two publications, 6 more manuscript drafts are currently in preparation for submission in 2023:

1- The effect of polycrystallinity on magnetotransport and skyrmion logic devices: We report on the tight tolerance window of material parameters (saturation magnetization and uniaxial anisotropy) for feasible operation.
2- Skyrmion logic gates and circuits: The results presented in Chapter 5 of this thesis are going to be published.
3- A perspective paper on topological nanospintronics: Opportunities for robust, low power and wideband spintronic logic device designs, new science and the merits of topological properties, scaling, and integration into electronic design automation.
4- Low power and topological Hall effect-free stabilization and magnetotransport of skyrmion pairs: Using synthetic antiferromagnetic coupling, two skyrmions along two parallel interfaces of magnetic/nonmagnetic layers are driven with low power and no skyrmion Hall effect.
5- Logic gates with no skyrmion Hall effect: This thesis mainly focuses on skyrmions along a magnetic/nonmagnetic bilayer, but the study takes these results further by constructing logic gates to process skyrmion pairs that are coupled antiferromagnetically and by eliminating skyrmion Hall effect.
6- Stabilization and transport of skyrmion pairs along EuS/Bi_2Se_3/EuS interfaces: Skyrmions are stabilized along both top and bottom interfaces of magnetic EuS and topological insulator Bi_2Se_3. These interfaces help minimize Joule heating by tuning the Fermi level on the topological insulator interfaces and insulating TI bulk.

1.3.2 Conference Papers

Parts of this thesis and the related work have been presented in conferences. The conference presentations of the works are:

1- Oral presentation at 2022 Joint MMM-INTERMAG conference: Arash Mousavi Cheghabouri, M.C.O. *Domain Wall-Gated, Cascaded and Low-Power Skyrmion Logic Gates with Robust Operation*. in *2022 Joint MMM-INTERMAG*. 2022. Underline Science Inc. [92].

2- Poster at the APS March Meeting 2022: Onbasli, M.C. and A. Mousavi Cheghabouri. *Paving the way for Boolean logic by skyrmion based programmable logic devices*. in *APS March Meeting Abstracts*. 2022. [93]

3- Oral presentation at APS March Meeting 2023: Onbasli, M.C., A. Mousavi Cheghabouri, and F. Katmis, *The Effect of Polycrystallinity on Skyrmion Logic Devices*. Bulletin of the American Physical Society, 2023 [94].

1.3.3 Repositories and Tools

The software of this thesis has been posted on the following repository:

https://github.com/arash-mc/skyrmion_gates_project

The supplementary materials are posted on the following repository:

https://github.com/arash-mc/thesis_suplementary

1.3.4 Scientific Contributions

The publication that has come out of this thesis have shown that scalable skyrmionics systems are possible. The finite temperature modeling, the detailed study of the forces acting on the magnetic textures, and the geometric sweeps contain novel aspects in the literature of micromagnetic.

The skyrmion generator paper offers skyrmion generation for rates up to 21 GHz. The reversible control of the frequency of skyrmion generation and spanning more than seven octaves of frequency range are of the most prominent scientific and figure-of-merit achievements of that part of the work [90].

The inverter gate paper shows a non-synchronized universal gate for skyrmionics logic. The detailed energy and force analysis, Joule heating and thermal conditions are also studied in this paper [91].

The findings of this thesis come together into a coherent skyrmionics logic picture towards the end of this thesis.

The insights of working through this thesis helped the author participate in the book chapter "Theory and Modeling of Spintronics Nanomagnets" [95].

1.3.5 Technical and Engineering Contributions

Micromagnetic modeling and Landau-Lifshitz-Gilbert differential equation reached maturity in solving a chiral magnetic spin profile under hydrodynamic and classical length-scale assumptions. However, the micromagnetic software are not very advanced in facilitating the researchers to conduct systematic simulations. A part of the work of this thesis is about making the systematic and high scale micromagnetic simulations accessible to researchers. The 2D simulation software brings automation of script generation, integration with High Performance Computing (HPC) and viewing and post processing more accessible.

This thesis brings about the first engineering approach to skyrmionics logic. By the results of this thesis the field of skyrmionics logic has been brought up one level in the technology readiness levels (TRL) from TRL1 to TRL2. The emulation software is accessible from the web in the following link: https://www.arashmousavi.com/skyrmionApp/

The results of this thesis have been also awarded the 3rd place of KUIMPACT 2022 patent competition and the patenting procedures are being conducted by Koç University's VPRD office (VPRD: Vice President of Research and Development).

Chapter 2

METHODS

2.1 Introduction

This chapter presents the theory and methods used in this thesis. A discussion of this work will not be possible without understanding magnetism, micromagnetics, computational micromagnetics, and Boolean algebra. Each of these topics is extensive, and several chapters can be devoted to any of them. This chapter tries to present the minimum necessary introduction for the reader to understand the rest of the chapters. It also aims to provide the main concepts for a deeper understanding, the tools for detailed analysis, and a list of software for reproducing the results or using the provided software library of the thesis.

The origins of magnetism, the pivotal role of angular momentum in magnetism, the quantum theory of angular momentum, and the similarities and differences between classical and quantum explanations are touched upon in this chapter.

The link between angular momentum and magnetism is the foundation of the Landau-Lifshitz-Gilbert (LLG) equation as the central equation for the dynamics of magnetic moments. This equation is derived from a simple and intuitive perspective. This derivation simplifies the understanding of the LLG equation.

Different energy terms contributing to magnetism lead to different types and equilibria conditions in magnetic materials. This chapter introduces these energy terms as the relationship between localized magnetic moments. The materials are curated to bridge the theory of discrete magnetic moments to the continuum limit, i.e., the theory of micromagnetics.

This chapter introduces Boolean algebra as the underpinning theory of the computations achieved by magnetic textures in this thesis.

2.2 Classical Description of Magnetism in Matter

Magnetism in matter arises from the combined effect of electric charge with spin and orbital angular momentum of electrons. This effect is macroscopically understood by thinking of a closed electric circuit in a magnetic field. From classical electromagnetism, we know that the energy of the circuit in this magnetic field is:

$$E = -(IA)\hat{\boldsymbol{n}} \cdot \boldsymbol{B} \tag{2.1}$$

Where I is the electric current, $\hat{n}$ is the normal vector to the circuit's plane, and A is the circuit's area. We can rewrite equation (2.1) as

$$E = -\boldsymbol{\mu} \cdot \boldsymbol{B} \tag{2.2}$$

with $\boldsymbol{\mu} = (IA)\hat{n}$. We call $\boldsymbol{\mu}$ the magnetic moment of the circuit. As per this definition, the SI unit of the magnetic moment is A m².

If we think of a single orbiting electron as an analog of an electric circuit, its associated electric current is:

$$I = \frac{e}{T} \tag{2.3}$$

Where e is the electron charge and T is the time of one revolution. The period of an orbiting object is:

$$T = \frac{2\pi r}{v}. \tag{2.4}$$

Where r is the radius of the path, and v is the speed of the object. Since by assuming a circular path for electron: $A = \pi r^2$, we can find the orbiting electron's magnetic moment as:

$$\mu = IA = \frac{e\pi r^2 v}{2\pi r} = \frac{evr}{2} \tag{2.5}$$

We must note that since the charge of the electron is negative, this equation has an inherent negative sign. Furthermore, since angular momentum is a central property of electrons in quantum mechanics, the standard way to represent equation (2.5) is to rewrite it in terms of angular momentum.

The angular momentum of an orbiting object with mass m, velocity v, and orbit radius r is:

$$\boldsymbol{L} = mvr\,\hat{\boldsymbol{n}} \tag{2.6}$$

Thus, we can rewrite equation (2.5) as

$$\boldsymbol{\mu} = \frac{e\boldsymbol{L}}{2m_e} = -\frac{|e|}{2m_e}\boldsymbol{L} = \gamma_L \boldsymbol{L} \tag{2.7}$$.

The gyromagnetic ratio γ_L is the ratio of the electron's magnetic moment to its angular momentum.

A confirmation of the validity of this analogy is shown experimentally in

Einstein–de Haas experiment. In this experiment, a hung ferromagnetic rod rotates when its magnetization changes. This effect, predicted by O. W. Richardson [96] in 1908, was shown experimentally by Albert Einstein and Wander Johannes de Haas in 1915 [97, 98]. The reverse effect was also observed by Samuel Barnett in 1915. In Barnett's experiment spontaneous magnetization was induced in a rotating Ferromagnetic rod [99].

2.3 Quantum Mechanical Angular Momentum

Quantum mechanics emerged in 20th century to explain the experiment results unexplainable by the classical physics of the time. In quantum mechanics, a wave function describes the system's state. The physical quantities are obtained by operators that act on this wave function. At first, there were two formulations for quantum theory: Schrodinger's formulations based on Schrodinger's wave equation that represented the state as a wave and the physical quantities as differential operators acting on the wave, and the Heisenberg formulation that represented the state by a vector and represented the quantities by matrices acting on the state vector. Later, Paul Dirac completed both representations by including special relativity and providing a unified picture and notation.

2.3.1 Quantum Mechanical Angular Momentum

In Schrodinger's formulation, the state of a system is a continuous complex-valued wavefunction $\psi(x)$ where x represents the system's physical dimensions. In Dirac's notation, the wavefunction is shown by $|\psi>$, and its complex conjugate is shown by $<\psi|$, which are called "ket" and "bra" of ψ respectively, and $<\psi|\psi> = 1$ that means that ψ is a normalized wave function.

$$<\psi|\psi>= \int \psi(x)\psi^*(x)dx = 1 \tag{2.8}$$

Since in quantum mechanics, we deal with the probabilities of obtaining a value for a physical quantity rather than its exact value, the "expected" value of physical quantities becomes an essential property of the system. We find the expected value of the quantity q under the continuous wavefunction ψ by

$$<Q>=<\psi|Q|\psi> = \int \psi(x)Q\psi^*(x)dx \tag{2.9}$$

Where Q is the operator related to the quantity q. If for an operator Q

$$Q|\psi> = \lambda|\psi> \tag{2.10}$$

We say that λ is an eigenvalue of the operator and since ψ is a normalized function,

$$< Q >=< \psi|Q|\psi >= \lambda < \psi|\psi >= \lambda. \tag{2.11}$$

The momentum operator is:

$$\boldsymbol{p} = -i\,\hbar\nabla, \tag{2.12}$$

and the position operator is:

$$\boldsymbol{r} = \boldsymbol{r}. \tag{2.13}$$

Thus, the angular momentum operator can be defined as

$$\boldsymbol{L} = -i\hbar\,\boldsymbol{r} \times \nabla. \tag{2.14}$$

If we write the components of this operator in cartesian coordinates, we have:

$$\begin{aligned} \boldsymbol{L} &= L_x\hat{\boldsymbol{e}}_{\boldsymbol{x}} + L_y\hat{\boldsymbol{e}}_{\boldsymbol{y}} + L_z\hat{\boldsymbol{e}}_{\boldsymbol{z}} \\ &= -i\hbar\left[\left(y\frac{\partial}{\partial z} - z\frac{\partial}{\partial y}\right)\hat{\boldsymbol{e}}_{\boldsymbol{x}}\right. \\ &\quad \left. + \left(z\frac{\partial}{\partial x} - x\frac{\partial}{\partial z}\right)\hat{\boldsymbol{e}}_{\boldsymbol{y}} + \left(x\frac{\partial}{\partial y} - y\frac{\partial}{\partial x}\right)\hat{\boldsymbol{e}}_{\boldsymbol{z}}\right]. \end{aligned} \tag{2.15}$$

Operators do not generally commute as numbers do. So naturally, $AB \neq BA$. To check the difference between these permutations of operators A and B, the commutation of the operators is defined as

$$[A, B] = AB - BA \tag{2.16}$$

One can prove that:

$$[x, p] = i\hbar, \tag{2.17}$$

which means that the eigenstates of x and p are different. This results in Heisenberg's uncertainty principle. For angular momentum, one also can obtain the following commutation relations:

$$[L_x, L_y] = i\hbar L_z, [L_y, L_z] = i\hbar L_x, [L_z, L_x] = i\hbar L_y \tag{2.18}$$

These relations lead to two significant consequences. First, since the different components of angular momentum do not commute, they don't have the same eigenstates. Thus, it is impossible to determine all the components of the angular momentum simultaneously. Secondly, the cross-product of angular momentum doesn't vanish as it does in classical mechanics.

$$\boldsymbol{L} \times \boldsymbol{L} = i\hbar\boldsymbol{L} \tag{2.19}$$

Although we have defined the angular momentum using the classical counterpart of $\boldsymbol{r} \times \boldsymbol{p}$, any operator that can satisfy the above equations can be an angular momentum operator. We will see this in the case of electron spin in the next section.

We can define the raising and lowering angular momentum operators as:

$$L_+ = L_x + iL_y$$
$$L_- = L_x - iL_y, \tag{2.20}$$

which satisfy:

$$[L_z, L_+] = \hbar L_+. \tag{2.21}$$

We also define the L^2 operator as:

$$L^2 = \boldsymbol{L} \cdot \boldsymbol{L} = L_x^2 + L_y^2 + L_z^2, \tag{2.22}$$

that commutes with all angular momentum operators defined so far.

$$[L^2, L_x] = [L^2, L_y] = [L^2, L_z] = [L^2, L_+] = [L^2, L_-] = 0 \tag{2.23}$$.

If $|\psi_m >$ is an eigenstate of L_z such that $L_z|\psi_m > = m\hbar|\psi_m >$,

$$L_z(L_+|\psi_m >) = (m+1)\hbar\,(L_+|\psi_m >). \tag{2.24}$$

Similarly,

$$L_z(L_-|\psi_m >) = (m-1)\hbar\,(L_-|\psi_m >).$$

The definition of these operators and the relationship between them shows that a wave function $|\psi >$ can be the eigenfunction of a single component of the angular momentum operator, i.e., x, y, z, and not all of them. This limitation is crucial in understanding the quantum angular momentum. We know angular momentum as a vector with well-defined components in classical physics. On the contrary, only one of these components can have a well-defined value in quantum physics. Thus, a vector understanding of angular momentum leads to a well-defined z component without a distinct phase, i.e., with a defined polar angle and undeterminable azimuthal angle.

If we suppose that $|\psi >$ is an eigenstate of L_z such that

$$L_z|\psi_m > = m\hbar|\psi_m > \tag{2.25}$$

Since $[L^2, L_z] = 0$, $|\psi_m >$ is also an eigenstate of L^2. Thus,

$$L^2|\psi_m > = \lambda\hbar^2|\psi_m > \tag{2.26}$$

Where λ must be determined in some way. To find the value of λ, we must solve the eigenvalue equation. Although we have the definition of L^2 as

$$L^2 = L_x^2 + L_y^2 + L_z^2 \tag{2.27}$$

since no wavefunction is the simultaneous eigenstate of these components, we cannot use this equation and must rewrite L^2 in terms of commutable operators.

One can verify the following expression:

$$L^2 = \frac{1}{2}(L_-L_+ + L_+L_-) + L_z^2 = L_-L_+ + L_z(L_z + \hbar). \tag{2.28}$$

Let's consider an angular momentum vector with an undetermined phase and determined z component. We can think of the state where the vector has reached its closest angle with the z-axis and further operation of L_+ doesn't increase the z component. In this state, we suppose $L_+|\psi> = 0$. If at this state $m = l$, i.e., $L_z|\psi>$ $= l\,|\psi>$, and name the state $|\psi_l>$ we have:

$$L^2|\psi_l> = \hbar^2 l(l+1)|\psi_l> \tag{2.29}$$

thus

$$\lambda = l(l+1). \tag{2.30}$$

Now, if we lower the z component by using L_- operator, we can verify that the eigenvalue of L^2operator does not change, i.e.,

$$L_z(L_-|\psi_l>) = \hbar(l-1)(L_-|\psi_l>), \tag{2.31}$$

and

$$L^2(L_-|\psi_l>) = \hbar^2 l(l+1)(L_-|\psi_l>). \tag{2.32}$$

this result is comparable to a classical vector with fixed magnitude $\hbar\sqrt{l(l+1)}$ around the z-axis.

A similar analysis follows with the smallest value for the z component, i.e., we find $-l$ for that value and $\hbar^2 l(l+1)$ for the L^2 operator. Thus

$$-l \leq m \leq l. \tag{2.33}$$

Since the raising and lowering operators can change m by integer values and m can change between $-l$ and l, l can have the values of $\frac{1}{2}, 1, \frac{3}{2}, 2, \ldots$

For an orbiting object around the z-axis

$$L_z = -i\hbar\frac{\partial}{\partial\phi} \tag{2.34}$$

Where ϕ is the azimuthal angle. One eigenstate for this operator with m as its eigenvalue is:

$$|\psi_m> = e^{im\phi} \tag{2.35}$$

Since the orbiting object must produce the same result when rotated 2π degrees due to circular/spherical symmetry, we must have:

$$|\psi_m> = e^{im\phi} = e^{im\phi(1+2\pi)} \tag{2.36}$$

This means that for orbital angular momentum, m (and therefore l) must be an integer number.

Figure 2.1 summarizes this discussion by showing the case for m=2. The z component of angular momentum can take discrete integer values between $-2\hbar$ and $2\hbar$, and the length of the angular momentum vector is $\sqrt{\hbar 2(2+1)}$.

2.3.2 Stern and Gerlach Experiment

When a classical particle with a magnetic moment and zero net charge moves inside a uniform magnetic field, it is expected to precess around the direction of the magnetic field while moving. Still, the course of the movement does not change. Thus, all particles that emerge in a single ray will not deflect and will reach the same point on the detector. If the magnetic field's intensity changes in the z-direction, the slight change of the magnetic field in the z-direction deflects the particle's trajectory towards +z or -z based on its magnetic moment's initial angle. In short, the deflection of the particles is parallel to the direction of the magnetic field and proportional to $\boldsymbol{\mu} \cdot \boldsymbol{B}$. So, if we send an unpolarized beam of classical particles through a magnetic field with +z variation, we expect to see a uniform spread of the particles on a detector. In 1922 Stern and Gerlach conducted this experiment on the atoms of silver, and the result was two separate areas in the z-direction instead of a spread. This surprising result means two things:

1- The angular momentum of the Ag atoms was quantized.
2- The quantization of angular momentum had only two values.

The first result might not surprise us based on our discussion of the quantum nature of angular momentum. The second result is still surprising as for an orbiting object, l is an integer, and if it is non-zero and at its least, m can take three values of $-1, 0, 1$. Thus, we must see three lines. The fact that we only see two lines means $l = \frac{1}{2}$. This perplexing result indicated that the angular momentum of the silver atoms could not have come from an orbiting object.

To understand the perplexity of the value of $l = \frac{1}{2}$, let's think of an orbiting object to have this value. According to equation (2.36), the object must be such that it revolves around itself twice (720 degrees) to reach the initial state, which contrasts with the reality as we understand it. Therefore, the source of the half-integer angular momentum is supposed to be an intrinsic property not an outcome of orbiting. Many particles, such as electrons, neutrons, protons, etc., are proven to have half-integer angular momentum. This property is called "spin" to differentiate this angular momentum from the orbital angular momentum. Particles with half-integer angular momentum follow Fermi-Dirac statistics and thus are called Fermions. Particles with integer angular momentum follow Bose-Einstein statistics and are called Bosons.

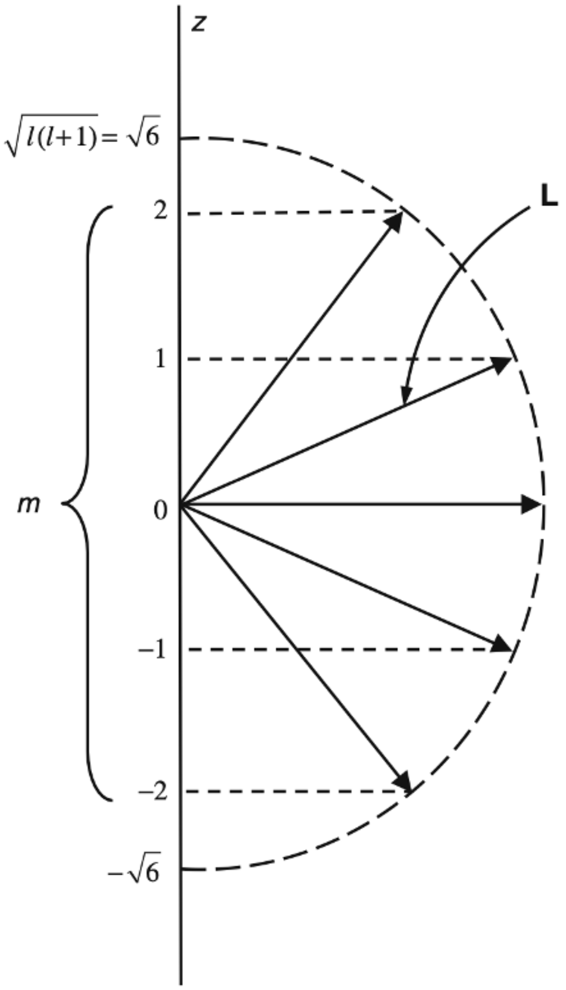

Figure 2.1.The vector interpretation of quantum angular momentum[100]**.**

2.3.3 Spin Angular Momentum

Spin can also be described by the operators that are proper angular momentum. These operators known as Pauli spin matrices constitute different components of the spin operator. Pauli matrices are:

$$\hat{\sigma}_x = \begin{pmatrix} 0 & 1 \\ 1 & 0 \end{pmatrix}, \; \hat{\sigma}_y = \begin{pmatrix} 0 & -i \\ i & 0 \end{pmatrix}, \hat{\sigma}_z = \begin{pmatrix} 1 & 0 \\ 0 & -1 \end{pmatrix} \tag{2.37}$$

That are put into the vector of matrices:

$$\boldsymbol{\sigma} = \hat{\sigma}_x \boldsymbol{e}_x + \hat{\sigma}_y \boldsymbol{e}_y + \hat{\sigma}_z \boldsymbol{e}_z \tag{2.38}$$

Now if we define:

$$\boldsymbol{S} = \frac{\hbar}{2}\boldsymbol{\sigma}, \tag{2.39}$$

we have

$$S_x = \frac{\hbar}{2}\,\hat{\sigma}_x, \qquad S_y = \frac{\hbar}{2}\,\hat{\sigma}_y, \qquad S_z = \frac{\hbar}{2}\,\hat{\sigma}_z\,. \tag{2.40}$$

We can write the eigenvalue equations:

$$S_z \begin{pmatrix}1\\0\end{pmatrix} = \frac{\hbar}{2}\begin{pmatrix}1\\0\end{pmatrix}, \qquad S_z \begin{pmatrix}0\\1\end{pmatrix} = -\frac{\hbar}{2}\begin{pmatrix}0\\1\end{pmatrix} \tag{2.41}$$

Based on the value of the spin, we name these two states the spin up and spin down states and denote them by

$$|\uparrow_z>= \begin{pmatrix}1\\0\end{pmatrix}, \qquad |\downarrow_z>= \begin{pmatrix}0\\1\end{pmatrix} \tag{2.42}$$

There are two eigenstates for the x, y components of the spin too. If we define S^2 as

$$S^2 = S_x^2 + S_y^2 + S_z^2 \tag{2.43}$$

And raising and lowering spin operators as

$$\begin{aligned} S_+ &= S_x + iS_y \\ S_- &= S_x - iS_y \end{aligned} \tag{2.44}$$

We can verify that spin operator possesses all conditions of a valid angular momentum operator.

2.3.4 Addition of Angular Momenta

Since the eigenstates of the spin and orbital angular momenta are different, for adding them we need to make a new state that is the eigenstate of both operators. We do this by multiplying the wavefunctions of these angular momenta. The simplest way to make this compound wavefunction is by multiplying the wavefunctions of the two angular momenta.

If we have two angular momenta described by wavefunction $\psi_{j_1m_1}$, $\psi_{j_2m_2}$ we can construct a wavefunction.

$$|\psi_{j_1m_1j_2m_2}>= \psi_{j_1m_1j_2m_2} = \psi_{j_1m_1} \times \psi_{j_2m_2} \tag{2.45}$$

This state represents the angular momentum of the system and is an eigenstate of the new system's angular momentum operator and thus has a set of values for the z-component that we represent by $\hbar m_{1,2}$ and has a magnitude $\hbar j_{1,2}(j_{1,2}+1)$.

If we construct the angular momentum operator of the new system as

$$\boldsymbol{J} = \boldsymbol{J_1} + \boldsymbol{J_2} \tag{2.46}$$

Since these angular momentum operators work on different parts of the state, they commute.

$$[\boldsymbol{J_1}, \boldsymbol{J_2}] = 0 \tag{2.47}$$

Using this result, we can prove that $\boldsymbol{J}$ is indeed an angular momentum operator and has all the properties of a proper angular momentum operator i.e.,

$$\boldsymbol{J} \times \boldsymbol{J} = i\hbar \boldsymbol{J} \tag{2.48}$$

Thus, we can find the highest angular momentum number for the z-component and call it j. We can visualize the relationship between these operators as vectors as Figure 2.2 shows.

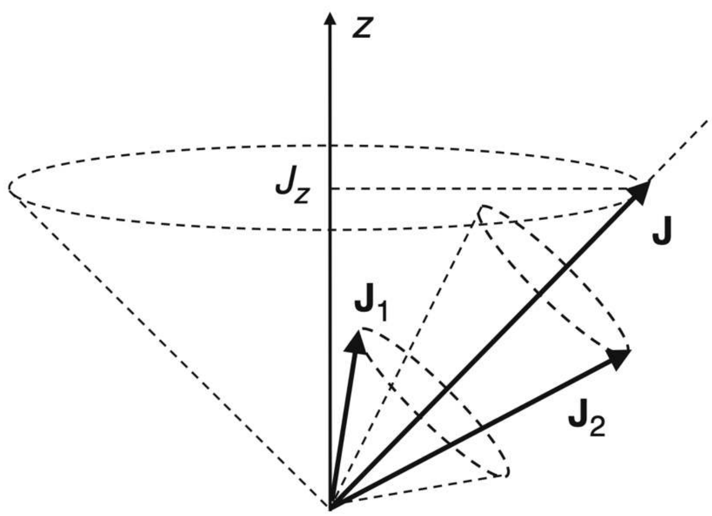

Figure 2.2.Two angular momentum vectors and their addition result [100]**.**

Since the spin of electron is an angular momentum itself, we can add it to the orbital angular momentum in this way. The addition is straightforward for single electron atoms and ions but for atoms with higher number of electrons the calculation becomes complex. Fortunately for the ground state of atoms and ions a simplification of adding spins and angular momenta separately and then joining them is possible. This simplification is known as Russell–Saunders coupling scheme [101]. In this scheme the total orbital angular momentum of electrons is calculated by

$$\boldsymbol{L} = \sum_i \boldsymbol{L}_i \tag{2.49}$$

And the total spin of electrons is calculated by:

$$\boldsymbol{S} = \sum_i \boldsymbol{S}_i \tag{2.50}$$

Then the total angular momentum of the atom or ion is calculated by

$$\boldsymbol{J} = \boldsymbol{L} + \boldsymbol{S} \tag{2.51}$$

2.4 Quantum Mechanical Angular Momentum and Magnetization

The quantized nature of angular momentum in atomic and sub-atomic scales produces quantized magnetic moments. The equation (2.7) holds for orbital angular momentum too. Since the angular momentum quantization step is $\hbar$, the quantization of magnetic moments is:

$$\boldsymbol{\mu_B} = \frac{e\hbar}{2m_e} \tag{2.52}$$

That is known as Bohr magneton. The electron spin is of a different nature from orbital angular momentum, and it has turned out that equation (2.7) needs a correcting factor for spin. This factor is called the Landé g-factor[102], and its value is 2. Thus, for an electron we have

$$\boldsymbol{\mu} = 2\gamma_L \boldsymbol{S}. \tag{2.53}$$

Where **S** is the spin of the electron. One needs to calculate the total orbital and spin angular momentums and apply these relations to get the magnetic moment of an atom or an ion. Thus, for calculating the magnetic moment arising from the combination of orbital angular momentum and spin is:

$$\boldsymbol{\mu} = \gamma_L(\boldsymbol{L} + 2\boldsymbol{S}) \tag{2.54}$$

We want a g factor to connect the magnetization to the total angular momentum:

$$\boldsymbol{\mu} = g\gamma_L \boldsymbol{J} = \boldsymbol{g}\gamma_L(\boldsymbol{L} + \boldsymbol{S}) \tag{2.55}$$

We get the inner product of both equations by $\boldsymbol{J}$ to have:

$$\begin{aligned} \gamma_L g J^2 &= \gamma_L(\boldsymbol{L} + 2\boldsymbol{S}) \cdot (\boldsymbol{L} + \boldsymbol{S}) \rightarrow g(L^2 + S^2) \\ &= (L^2 + 2S^2 + 3\boldsymbol{L} \cdot \boldsymbol{S}). \end{aligned} \tag{2.56}$$

Since by getting the dot product of equation (2.51)

$$\boldsymbol{L} \cdot \boldsymbol{S} = \frac{1}{2}(J^2 - L^2 - S^2), \tag{2.57}$$

we have

$$g = \frac{3}{2} + \frac{S^2 - L^2}{2J^2} \tag{2.58}$$

And since $S^2 = \frac{\hbar}{2} s(s+1)$, $L^2 = \hbar l(l+1)$

$$g = \frac{3}{2} + \frac{s(s+1) - l(l+1)}{2j(j+1)} \tag{2.59}$$

That reduces to 1 for pure orbital angular momentum and 2 for pure spin. Figure 2.3 shows the total orbital angular momentum, spin and magnetic moment. One crucial point for when there are both spin, and orbital momentum is that the magnetic moment's direction differs from the total angular momentum as Figure 2.3 shows.

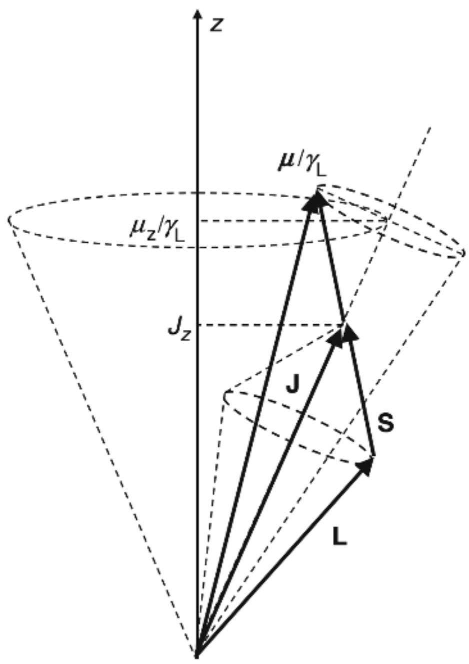

Figure 2.3. Total orbital, spin, and angular momentum relation with magnetic moment.

The discussion and figures provided for the quantum mechanical angular momentum and magnetization followed [100].

2.5 Magnetization Dynamics and Landau Lifshitz Gilbert (LLG) Equation

Since magnetic moment arises from angular momentum and electric charge, the dynamics of particles with magnetic moment follow the dynamics of massive particles with angular momentum.

To better understand magnetic moments' dynamics, let's consider an object with angular momentum. An example of a macroscopic object with angular momentum is a spinning top. The spinning top's rotation axis has a polar angle θ with the normal vector of a horizontal line. The gravitational energy of this spinning top is the gravitational field $\boldsymbol{G}$ is:

$$E = -\,\boldsymbol{G}\cdot md\boldsymbol{e}_l \tag{2.60}$$

Where m is the mass of the spinning top and d is the distance of the center of mass of the spinning top from its pivot point on the rotation axis. This gravitational field exerts a torque on the spinning top:

$$\mathbf{T} = md\boldsymbol{e}_l \times \boldsymbol{G} \tag{2.61}$$

This torque is normal to the angular momentum of the spinning top and thus causes the spinning top to rotate around the axis of the gravitational field. Since

$$\mathbf{T} = \dot{\boldsymbol{L}} \tag{2.62}$$

We can rewrite equation (2.61) as

$$\dot{\mathbf{L}} = md\boldsymbol{e}_l \times \boldsymbol{G} \tag{2.63}$$

Now, if we compare equations (2.61), and (2.63), we find the following equivalences:

$$\boldsymbol{B} \sim \boldsymbol{G} \ and\ \boldsymbol{\mu} \sim md\boldsymbol{e}_l \tag{2.64}$$

Now for a magnetic moment in the magnetic field, we can write as:

$$\dot{\boldsymbol{L}} = \frac{\dot{\boldsymbol{\mu}}}{\gamma_L} = \boldsymbol{\mu}\times\boldsymbol{B} \rightarrow \dot{\boldsymbol{\mu}} = \gamma_L\boldsymbol{\mu}\times\boldsymbol{B} \tag{2.65}$$

This equation is the precession term for the dynamics of a single magnetic moment in an external magnetic field. The standard form of this equation is in terms of magnetization **M** (magnetic moments per volume) and **H** (magnetic field intensity). Since

$$\boldsymbol{M} = \frac{\boldsymbol{\mu}}{v}, \qquad \boldsymbol{B} = \mu_0 \boldsymbol{H}$$

Where v is the unit of volume encapsulating $\boldsymbol{\mu}$, and μ_0 is the vacuum permeability. We can rewrite equation (2.65) as:

$$\dot{\boldsymbol{M}} = \gamma_L \mu_0 \boldsymbol{M} \times \boldsymbol{H} = \gamma_0 \boldsymbol{M} \times \boldsymbol{H} \tag{2.66}$$

which represents the precession term in the standard form in terms of magnetization and magnetic field.

Equation (2.66) means that a magnetic field causes a precession in the magnetization vector. The precessional term is normal to the magnetization vector. Therefore, it cannot not change the length of the magnetization vector i.e., applying a magnetic field cannot change the magnitude of the magnetization.

Although equation (2.66) accounts for the precession in the magnetization in presence of a magnetic field, it doesn't capture the complete picture. According to equation (2.66), the magnetization processes around the axis of the applied field without aligning with the magnetic field. In the real world, the magnetization eventually aligns with the magnetic field, i.e., the precession dampens out. Thus, this equation needs a "damping" term. The original damping term added by Landau and Lifshitz (LL) was:

$$\dot{\boldsymbol{M}}_{\boldsymbol{d}} = -\lambda\, \boldsymbol{M} \times (\boldsymbol{M} \times \boldsymbol{H}) \tag{2.67}$$

where λ is the phenomenological damping term. By adding the damping term to equation (2.66), we have the Landau-Lifshitz equation for the magnetic moment's dynamics in the magnetic field.

$$\dot{\boldsymbol{M}} = \gamma_0\, \boldsymbol{M} \times \boldsymbol{H} - \lambda \boldsymbol{M} \times (\boldsymbol{M} \times \boldsymbol{H}) \tag{2.68}$$

This equation captures the precession and damping in the precession of the magnetic moment. This damping results in the alignment of the magnetization with the applied field. One should also note that the damping term is normal to the magnetization vector.

There is a more accurate account for the damping term, which is an Ohmic type dissipation, as Gilbert (G) put forward in 1955 [103, 104]:

$$\dot{\boldsymbol{M}}_{\boldsymbol{dg}} = \eta \boldsymbol{M} \times \dot{\boldsymbol{M}} \tag{2.69}$$

The difference between the LL and G damping terms is that the LL damping term's magnitude depends only on the precession term's magnitude. This means that when the magnetization vector aligns more with the applied field, the damping term's magnitude becomes very small. On the other hand, Gilbert's damping term depends on the change of magnetization that includes both precession and damping and does not have this problem. The dynamics equation with G damping term is known as Landau-Lifshitz-Gilbert (LLG) equation:

$$\dot{\boldsymbol{M}} = \gamma_0 \boldsymbol{M} \times \boldsymbol{H} + \eta \boldsymbol{M} \times \dot{\boldsymbol{M}} \tag{2.70}$$

Since the change in the magnetization is normal to the magnetization itself, it doesn't change the length of the magnetization vector, similar to the precession term. Therefore, we can rewrite the equation in terms of the unit vector of magnetization. Moreover, since the magnetization in matter stems from the electrons, $\gamma_0 = -|\gamma_0|$ we can rewrite it as:

$$\dot{\boldsymbol{m}} = -\gamma \boldsymbol{m} \times \boldsymbol{H} + \alpha \boldsymbol{m} \times \dot{\boldsymbol{m}} \tag{2.71}$$

Where $\gamma = |\gamma_0|$ is the magnitude of the gyromagnetic ratio of the particle and $\alpha = \frac{\eta}{\boldsymbol{M}}$ is Gilbert's damping term.

A more computationally tractable version of equation (2.71) is used by substituting $\dot{\boldsymbol{m}}$ on the right-hand side and then simplifying:

$$\begin{gathered} \dot{\boldsymbol{m}} = -\gamma \boldsymbol{m} \times \boldsymbol{H} + \alpha \boldsymbol{m} \times (-\gamma \boldsymbol{m} \times \boldsymbol{H} + \alpha \boldsymbol{m} \times \dot{\boldsymbol{m}}) = \\ -\gamma\big[\boldsymbol{m} \times \boldsymbol{H} + \alpha\big(\boldsymbol{m} \times (\boldsymbol{m} \times \boldsymbol{H})\big)\big] + \alpha^2 \boldsymbol{m} \times (\boldsymbol{m} \times \dot{\boldsymbol{m}}) \end{gathered} \tag{2.72}$$

And since

$$A \times (B \times C) = B(C \cdot A) - C(A \cdot B) \tag{2.73}$$

We have

$$\boldsymbol{m} \times (\boldsymbol{m} \times \dot{\boldsymbol{m}}) = \boldsymbol{m}(\boldsymbol{m} \cdot \dot{\boldsymbol{m}}) - \dot{\boldsymbol{m}}(\boldsymbol{m} \cdot \boldsymbol{m}) \tag{2.74}$$

Since $\dot{\boldsymbol{m}}$ is normal to $\boldsymbol{m}$, and $\boldsymbol{m} \cdot \boldsymbol{m} = 1$ the equation (2.72) becomes:

$$\begin{gathered} \dot{\boldsymbol{m}} = -\gamma\big[\boldsymbol{m} \times \boldsymbol{H} + \alpha\big(\boldsymbol{m} \times (\boldsymbol{m} \times \boldsymbol{H})\big)\big] - \alpha^2 \dot{\boldsymbol{m}} \rightarrow \\ (1 + \alpha^2)\dot{\boldsymbol{m}} = -\gamma\big[\boldsymbol{m} \times \boldsymbol{H} + \alpha\big(\boldsymbol{m} \times (\boldsymbol{m} \times \boldsymbol{H})\big)\big] \end{gathered} \tag{2.75}$$

The use of $\boldsymbol{\mu}$ for a magnetic moment and the magnetic permeability in the literature are coincidental. They do not represent the same quantities and do not have the same dimensions.

Figure 2.4 shows the dynamics of a magnetic moment in an external magnetic field according to the LLG equation.

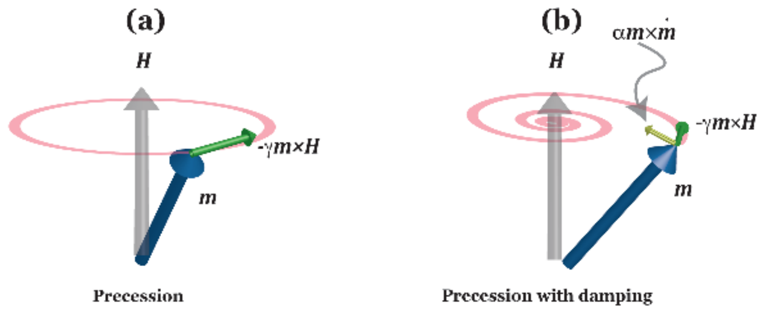

Figure 2.4. Dynamics of a magnetic moment with LLG. (a) The precession term in the LLG equation. (b) The precession and Gilbert damping term in the LLG equation [95].

2.6 Energy Terms

To this point we have established that the magnetic moments of atoms arise from the combinational effect of angular momentum and electric charge. Moreover, LLG explains the dynamics of a magnetic moment in an applied magnetic field. Further description of the forces is needed to explain the dynamics of magnetization. To fully understand magnetization in ensemble media like magnetic materials, we need to consider the energies acting on magnetic moments.

2.6.1 Zeeman Energy

Zeeman energy is the energy of a magnetic moment in an applied magnetic field. This energy resembles the energy of a closed circuit in an external magnetic field. The Zeeman energy of a set of magnetic moments in the constant external magnetic flux density ***B*** is:

$$E_z = -\sum_i \boldsymbol{\mu}_i \cdot \boldsymbol{B} \tag{2.76}$$

This equation means that the energy of a magnetic moment is maximum when the moment is facing opposite to the magnetic field and is minimum when the moment's direction is in line with the magnetic field. Therefore, Zeeman energy describes that magnetic moments prefer to align with the external applied magnetic field for a minimum equilibrium energy state when there are no other energy terms.

2.6.2 Dipolar Energy

Dipolar energy is the energy of the magnetic moments acting on each other.

The dipolar energy between a moment at site i and all other magnetic moments in the system is:

$$E_d = -\boldsymbol{\mu_i} \cdot \sum_{j \neq i} \boldsymbol{B_{ji}} \tag{2.77}$$

Where $\boldsymbol{B_{ji}}$ is the magnetic flux density arising from the moment $\boldsymbol{\mu_j}$ on the site of $\boldsymbol{\mu_i}$. The total dipolar energy of the system is:

$$E_d = -\frac{1}{2}\sum_{i} \cdot \sum_{j \neq i} \boldsymbol{\mu_i} \cdot \boldsymbol{B_{ji}} \tag{2.78}$$

The factor ½ here is because we must count the energy between two magnetic moments just once. We know from classical electromagnetism that the dipolar field B_{ji} of a magnetic moment $\boldsymbol{\mu_j}$ in the location $\boldsymbol{r_i}$ is:

$$B_{ji} = \frac{\mu_0}{4\pi}\left(\frac{3\left(\boldsymbol{\mu_j}.\left(\boldsymbol{r_i}-\boldsymbol{r_j}\right)\right)}{\left|\boldsymbol{r_i}-\boldsymbol{r_j}\right|^5}\left(\boldsymbol{r_i}-\boldsymbol{r_j}\right) - \frac{\boldsymbol{\mu_j}}{\left|\boldsymbol{r_i}-\boldsymbol{r_j}\right|^3}\right) \tag{2.79}$$

This equation shows that the magnetic field arising from a magnetic moment on locations on its sides (where $\boldsymbol{\mu_j}.\left(\boldsymbol{r_i}-\boldsymbol{r_j}\right) = 0$) is opposite to the direction of the magnetic moment itself. Thus, magnetic moments try to force each other in the opposite direction of themselves. This effect is evident macroscopically when rod magnets are brought beside each other—putting the magnets facing the same direction results in a repulsive force while putting them in the opposite direction results in the attractive force between the two magnets.

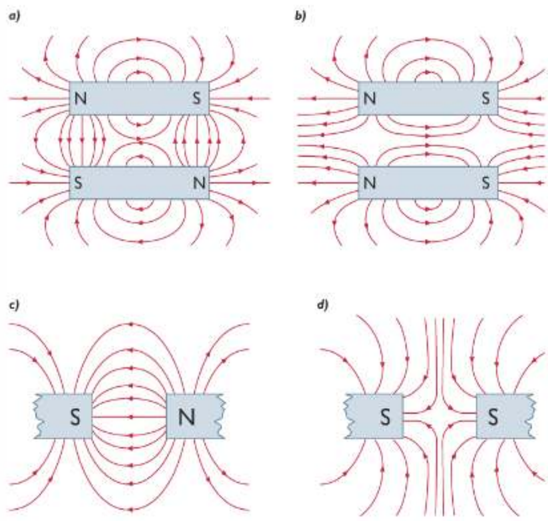

Figure 2.5.The dipolar fields between two magnets placed beside each other.

2.6.3 Heisenberg Exchange Energy

The earliest modern explanation of the ferromagnetism was the Weiss molecular field theory in 1907 [105]. This theory agreed with the results of experiments, but later turned out that the molecular magnetic field had to be very large of the order of $\sim 10^4$ of the local magnetization to produce ferromagnetic order. Later in 1911 Bohr proved that an ensemble of classical non-relativistic electrons couldn't produce ferromagnetism. This result was re-discovered by J. H. van Leeuwen [106] and was later known as Bohr- van Leeuwen theorem. The next step was the Lenz-Ising formulation that required the spins to interact with the neighboring spins on a certain range and they could have the values of ± 1 on a one-dimensional chain [107].

Since the Pauli spin operators of equation (2.37) had established the electron spins as vector quantities, Dirac proposed the spin Hamiltonian form as [108]:

$$E_{ex} = -\sum_{i,j} j_{i,j}\, \boldsymbol{S_i} \cdot \boldsymbol{S_j} \tag{2.80}$$

Werner Heisenberg also independently discovered this Hamiltonian in 1926 [109]. This is called the exchange interaction and becomes important when electron wave functions are overlapping. This term is a result of the indistinguishability of electrons and the fact that based on the Pauli exclusion principle, exchange of electrons must produce antisymmetric wavefunction despite the indistinguishability of electrons.

To see how exchange interaction changes the alignment of two electrons, we think of a Hamiltonian operator like equation (2.80). We can think of a total spin of the state of two electrons:

$$\boldsymbol{S} = \boldsymbol{S}_1 + \boldsymbol{S}_2 \tag{2.81}$$

Thus,

$$\boldsymbol{S}^2 = \boldsymbol{S}_1^2 + \boldsymbol{S}_2^2 + 2\boldsymbol{S_1} \cdot \boldsymbol{S_2} \tag{2.82}$$

We know from the discussion of the sections 2.3.3 and 2.3.4 that this is a proper angular momentum operator. Since by combining two spin ½ particles we can reach the total angular momentum numbers of s=0, s=1, the eigenvalues of the $\boldsymbol{S^2}$ operator are either $\hbar 0(0+1) = 0$ or $\hbar 1(1+1) = 2\hbar$. Thus, we have two different states where one has a single state with no angular momentum (analog to two opposite electrons) and the other has three states with $m = -1, 0, 1$ (analog to two electrons in the same direction). We can solve for the eigenvalue of the $\boldsymbol{S_1} \cdot \boldsymbol{S_2}$ operator for both cases:

$$\boldsymbol{S_1} \cdot \boldsymbol{S_2} = \begin{cases} \frac{1}{4}\hbar & s = 1 \\ -\frac{3}{4}\hbar & s = 0 \end{cases} \tag{2.83}$$

This means that for the Hamiltonian of the form $-J_{ex}\boldsymbol{S_1} \cdot \boldsymbol{S_2}$, the energy of the states is:

$$-J_{ex}\boldsymbol{S_1} \cdot \boldsymbol{S_2} = \begin{cases} \frac{-J_{ex}}{4}\hbar & s = 1 \\ \frac{3J_{ex}}{4}\hbar & s = 0 \end{cases} \tag{2.84}$$

That for $J_{ex} > 0$ results in the lower energy for the state with s=1.

We can write the exchange energy in terms of the magnetic moments to emphasize the magnetism as our property of interest.

$$E_{ex} = -J_{ex}\boldsymbol{\mu_i} \cdot \boldsymbol{\mu_j} \tag{2.85}$$

If $J_{ex} > 0$ the adjacent magnetic moments tend to be aligned in the same direction, and if $J_{ex} < 0$, the adjacent magnetic moments take alternate directions. Figure 2.6 shows these effects. Thus, if $J_{ex} > 0$, the effect of the exchange energy is opposite to the dipolar energy. The exchange energy only acts in small lengths where electron wavefunctions overlap, and the dipolar energy wins in longer length scales. The competition between exchange energy and dipolar energy results in regions of material with uniform magnetization (due to the exchange energy) that are different from the adjacent region (due to the dipolar energy). These regions are called magnetic domains.

Since the change in the magnetization from one region to the other must be continuous, a transition region between domains must arise. These transition regions are called domain walls.

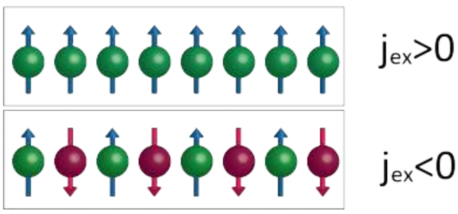

Figure 2.6. The effect of the Heisenberg exchange coefficient sign on neighboring spin arrangement[95]**.**

2.6.4 Dzyaloshinskii-Moria Interaction (DMI)

The relativistic effect of the coupling between spin and orbital angular momentum results in the Dzyaloshinskii-Moriya interaction (DMI). This energy arises in materials such as MnSi with non-centrosymmetric crystal structures or in the multilayer of ferromagnets (FM) and heavy metals (HM) such as Co/Pt. The DMI energy Hamiltonian operator is [110, 111]

$$H^{DM} = \sum_{i,j} \boldsymbol{D}_{ij} \cdot (\boldsymbol{S}_i \times \boldsymbol{S}_j) \tag{2.86}$$

where $\boldsymbol{D}_{ij}$ is the direction of the DMI vector. Spins on the plane normal to this vector are aligned normal to each other. As equation (2.86) implies, DMI tries to align the adjacent spins normal to each other and normal to the $\boldsymbol{D}$ vector. Figure 2.7 illustrates an FM/HM bilayer. The large spin orbit coupling (SOC) of the heavy metal causes the DMI vector to be in the plane of the interface of the bilayer. The arrangement of the adjacent spins for the lowest energy of equation (2.86) is shown in Figure 2.7.

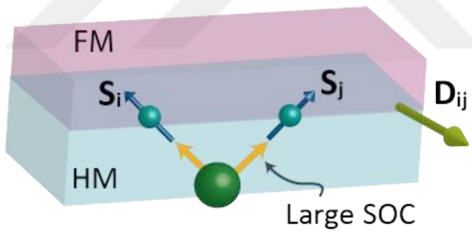

Figure 2.7. Dzyaloshinskii-Moriya interaction[95].

2.6.5 Magnetocrystalline Anisotropies

Spin-orbit coupling resulting from the arrangements of atoms in different crystal structures might result in different energies for the magnetization of a crystal cell for different axes. This phenomenon causes anisotropy in the preferred magnetization direction of the material. The magnetization aligns parallel to the lower energy axis. This axis is called the easy axis of the crystal. Two main types of anisotropies exist in magnetic materials: uniaxial anisotropy and cubic anisotropy.

Akulov derived the analytical form of the magnetocrystalline for cubic crystals [112].

2.7 Micromagnetics: The Continuum Theory of Magnetization

Although the magnetization in matter arises from quantum effects such as spin, orbital angular momentum, Heisenberg exchange, DMI, and anisotropy energies, an intermediate semi-classical computational theory is needed to explain different magnetic phenomena in larger nanometer and micrometer length scales. This theory, known as micromagnetics, puts these energies into a continuum framework. Many experimental studies have confirmed the validity of the micromagnetic models as was mentioned in chapter 1 of this thesis.

2.7.1 Magnetization

The central quantity in micromagnetics is magnetization. Magnetization is the volumetric density of magnetic moments. For a cell containing N tiny magnetic moments, the magnetization is:

$$\boldsymbol{M} = \frac{\sum_i^N \boldsymbol{\mu_i}}{V} \tag{2.87}$$

Where V is the volume containing the magnetic moments. Thus, the magnetization unit in SI is A m^{-1}, the unit of the magnetic field $\boldsymbol{H}$.

Since the maximum value of magnetization of a material type, i.e., saturation magnetization M_s is constant. In micromagnetics, the unit direction vector of magnetization $\boldsymbol{m} = \frac{\boldsymbol{M}}{M_s}$ is used instead of $\boldsymbol{M}$. Sometimes this vector is called the direction cosine of magnetization as its components are equal to the cosine of the deviations of magnetization from the cartesian axes.

2.7.2 Dipolar energy

The dipolar (magnetostatic) energy density is calculated by integrating the contributions of the magnetism of all points at the point of interest. To write the continuum equivalent of the equation (2.78), we first note that the absence of the magnetic monopole requires that the divergence of the magnetic flux density be zero everywhere, as one of Maxwell's four equations states:

$$\nabla \cdot \boldsymbol{B} = 0 \tag{2.88}$$

In materials with nonzero magnetization, the magnetic flux density $\boldsymbol{B}$ is the combination of magnetization and the magnetic field.

$$\boldsymbol{B} = \mu_0 \boldsymbol{H} + \mu_0 \boldsymbol{M} \tag{2.89}$$

If we get the divergence of both sides, we have:

$$\nabla \cdot \boldsymbol{H} = -\nabla \cdot \boldsymbol{M} \tag{2.90}$$

Since Maxwell's equation for the curl of magnetization is

$$\nabla \times \boldsymbol{H} = \boldsymbol{J} + \frac{\partial \boldsymbol{D}}{\partial t} \tag{2.91}$$

for the electrostatic case where there is no electric current density and time-dependent change in the electric displacement field $\boldsymbol{D}$, the right-hand side of the equation (2.91) is zero, i.e.,

$$\nabla \times \boldsymbol{H} = 0$$

Thus $\boldsymbol{H}$ can be written as the gradient of a potential. Now, if we define U such that:

$$\boldsymbol{H} = -\nabla U \tag{2.92}$$

and substitute in equation (2.90)

$$\nabla^2 U = \nabla \cdot \boldsymbol{M} \tag{2.93}$$

Now, if we define

$$\rho = -\nabla \cdot \boldsymbol{M} \tag{2.94}$$

The equation (2.93) becomes:

$$\nabla^2 U = -\rho$$

Which is the Poisson's equation and has the solution:

$$U = \frac{1}{4\pi} \iiint_V \frac{\rho(\boldsymbol{r}')}{|\boldsymbol{r} - \boldsymbol{r}'|} d^3\boldsymbol{r}' + \iint_S \frac{\sigma(\boldsymbol{r}')}{|\boldsymbol{r} - \boldsymbol{r}'|} d^2\boldsymbol{r}' \tag{2.95}$$

where:

$$\sigma = \boldsymbol{M} \cdot \hat{\boldsymbol{n}} \tag{2.96}$$

at the surface of the magnet. This results from applying the gauss theorem to the magnetization discontinuity for a small pillbox at the magnet's surface.

Figure 2.8 illustrates the coordinates, physical quantities, and integration variables of equation (2.95)[113].

One can then use this equation to calculate the magnetic field from the magnet's dipolar fields. Since this field contributes to the demagnetization of the magnet, it is called the demagnetization field. In a uniformly magnetized magnet, the contribution of the volume term, i.e., the bulk magnetization, is zero. Thus, the demagnetization field arises from the magnetization at the surfaces of the magnet. The discontinuity of magnetization at the surface of the magnet shows in the form of a delta function in $\nabla \cdot \boldsymbol{M}$ which is the surface term of equation (2.95).

With the demagnetization field, the demagnetization energy of the magnetic material can be calculated. Equation (2.78) calculates this energy in summation form. It can be rewritten in continuum integral form as

$$E_d = -\frac{1}{2}\mu_0 \iiint_V \boldsymbol{H_d}.\boldsymbol{M}(\boldsymbol{r})d^3\boldsymbol{r} \tag{2.97}$$

And the demagnetization energy density at each point is:

$$\phi_d = -\frac{1}{2}\mu_0 \boldsymbol{H_d} \cdot \boldsymbol{M} \tag{2.98}$$

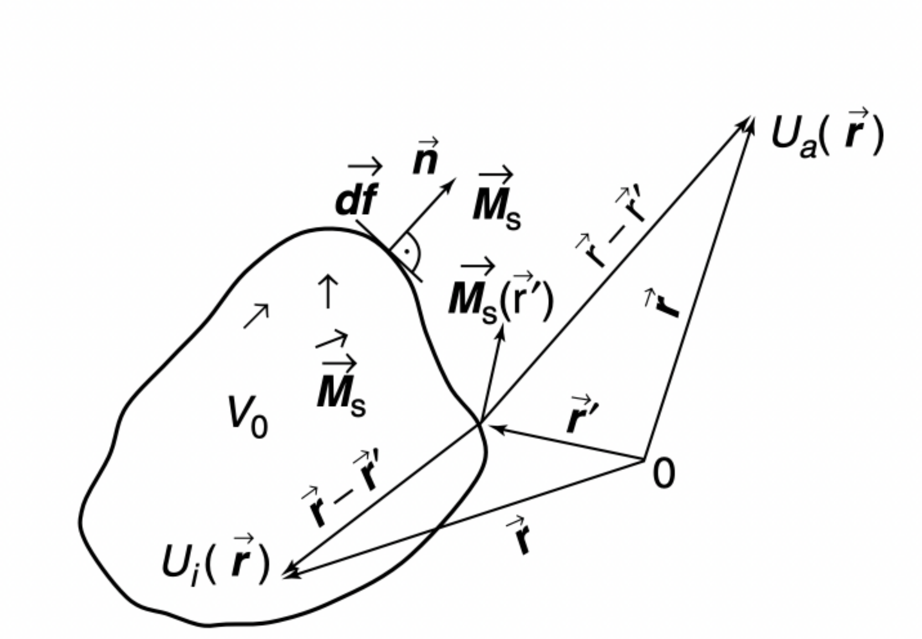

Figure 2.8. The magnetostatic potential inside and outside of a magnetic body of a material

2.7.3 Exchange Energy

The exchange energy of equation (2.85) that is between two individual dipoles has the continuum energy density equivalent [113]:

$$\Phi_{ex} = A_{ex}((\nabla m_x)^2 + \left(\nabla m_y\right)^2 + (\nabla m_z)^2) \tag{2.99}$$

Where A_{ex} (J/m) is the exchange energy coefficient and for cubic lattice is:

$$A_{ex} = \frac{2\,J_{ex}M_s^2}{N^2 g^2 \mu_B^2 a} \cdot c \tag{2.100}$$

2.7.4 Magneto-crystalline Anisotropy Energy Densities

The uniaxial anisotropy energy density expression in micromagnetics is:

$$\Phi_{Ku}(\boldsymbol{r}) = K_0(\boldsymbol{r}) + K_1(\boldsymbol{r})\, sin^2\, \phi(\boldsymbol{r}) \tag{2.101}$$

Where the $\phi(r)$ is the polar angle between a material's easy axis and the magnetization direction at point $\boldsymbol{r}$. K_0 and K_1 $(J \cdot m^{-3})$ are the uniaxial anisotropy constants. Since K_0 is only an offset to the energy and can contain material-specific uniaxial anisotropy effects. Figure 2.9 shows the uniaxial energy dependence on the deviation of the direction of magnetization from the easy axis.

Some materials also have cubic anisotropy. The following relation is for the lattice with cubic anisotropy energy.

$$\Phi_{Kc}(\boldsymbol{r}) = K_0(\boldsymbol{r}) + K_1(\boldsymbol{r}) \sum_{i \neq j} m_i m_j + K_2(\boldsymbol{r}) m_x^2(\boldsymbol{r}) m_y^2(\boldsymbol{r}) m_z^2(\boldsymbol{r}) \tag{2.102}$$

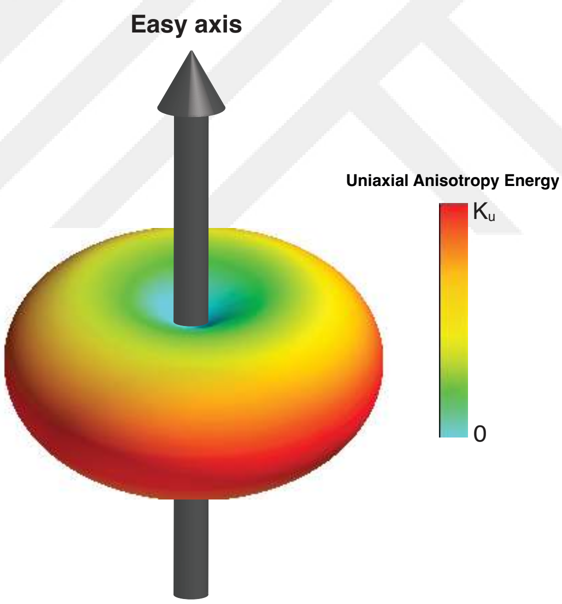

Figure 2.9. The magnetization direction dependence of the uniaxial anisotropy energy. The radius (from origin to radial distance vector) and color scale (blue to red) shows the angular dependence of uniaxial energy density. The lowest energy density direction (here; 0°) is the spontaneously preferred magnetization direction.

2.7.5 Effective Field

Magnetization dynamics depend on the effective magnetic field acting on each site. This effective field dynamically changes the magnetization through the LLG equation. According to Brown's theory of magnetization, the effective field is the derivative of the energy with respect to the components of magnetization [113]:

$$\boldsymbol{H_{eff}} = -\frac{1}{\mu_0 M_s}\frac{\delta\Phi}{\delta\boldsymbol{m}} \tag{2.103}$$

Where in cartesian coordinates:

$$\frac{\delta}{\delta\boldsymbol{m}} = (\frac{\partial}{\partial m_x}, \frac{\partial}{\partial m_y}, \frac{\partial}{\partial m_z}) \tag{2.104}$$

Here we drive the exchange energy of the equation (2.99). The derivation is done for the x component here. The derivations for the y and z components are similar. For the x component of the exchange effective field, we first calculate the derivative of the exchange energy with respect to m_x. Since the derivative is only with respect to m_x we need only to keep the m_x term in the exchange energy relation.

$$\begin{gathered}\frac{\partial}{\partial m_x}(A_{ex}(\nabla m_x)^2) = \\ A_{ex}\frac{\partial}{\partial m_x}\left(\left(\frac{\partial}{\partial x}m_x\right)^2 + \left(\frac{\partial}{\partial y}m_x\right)^2 + \left(\frac{\partial}{\partial z}m_x\right)^2\right) = \\ 2A_{ex}\left(\frac{\partial^2}{\partial x^2}m_x + \frac{\partial^2}{\partial y^2}m_x + \frac{\partial^2}{\partial z^2}m_x\right) = 2A_{ex}\nabla^2 m_x\end{gathered} \tag{2.105}$$

Since the Laplacian operator in cartesian coordinates for vector $\boldsymbol{m}$ is

$$\nabla^2\boldsymbol{m} = (\nabla^2 m_x + \nabla^2 m_y + \nabla^2 m_z) \tag{2.106}$$

The effective exchange field can be written as:

$$\boldsymbol{H_{ex}} = -\frac{2A_{ex}}{\mu_0 M_s}\nabla^2\boldsymbol{m} \tag{2.107}$$

Thus, the effective field is:

$$\boldsymbol{H}_{eff} = -\frac{2A_{ex}}{\mu_0 M_s}\nabla^2\boldsymbol{m} + \frac{\delta\Phi_{anis}}{\delta\boldsymbol{m}} + \boldsymbol{H}_d + \boldsymbol{H}_{ext} \tag{2.108}$$

2.7.6 Zhang-Li spin Transfer Torque

Zhang-Li spin transfer torque (STT) is the induced torque of the incoming spin polarized electrons in the spin-polarized current injection scheme [114, 115]:

$$\begin{gathered}(1+\alpha^2)\dot{\boldsymbol{m}}_{ZL} = [(1+\xi\alpha)\boldsymbol{m}\times(\boldsymbol{m}\times(\boldsymbol{u}\cdot\nabla)\boldsymbol{m}) \\ + (\xi-\alpha)\boldsymbol{m}\times(\boldsymbol{u}\cdot\nabla)\boldsymbol{m}]\end{gathered} \tag{2.109}$$

$$\boldsymbol{u} = \frac{\mu_B}{2e\gamma_0 M_s(1+\xi^2)}\boldsymbol{j} \tag{2.110}$$

Figure 2.10 shows the precession caused by the spin-polarized currents according to equation (2.109) [115].

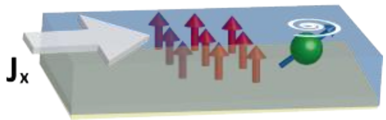

Figure 2.10. Precession of spins due to in-plane current. The in-plane current of spin polarized electrons (red arrows) causes a precession in the magnetic moments of the host material according to the Zhang-Li term[95].

2.7.7 Slonczewski Spin-Transfer Torque

The Slonczewski STT is the induced change in magnetization by the spins of electrons that have moved from a polarizer layer and a spacer layer and are injected normal to the plane of the material. The Slonczewski STT [115]:

$$\begin{aligned}(1+\alpha^2)\dot{\boldsymbol{m}}_{SL} &= \beta(\epsilon+\alpha\epsilon')\left(\boldsymbol{m}\times\left(\boldsymbol{m_p}\times\boldsymbol{m}\right)\right)\\ &\quad-\beta(\epsilon'-\alpha\epsilon)\boldsymbol{m}\times\boldsymbol{m_p}\end{aligned} \tag{2.111}$$

where:

$$\beta = \frac{j_z\hbar}{M_s e d} \tag{2.112}$$

and

$$\epsilon = \frac{P(\boldsymbol{r},t)\Lambda^2}{(\Lambda^2+1)+(\Lambda^2-1)(\boldsymbol{m}\cdot\boldsymbol{m_P})} \tag{2.113}$$

2.8 Unit systems

The SI system of units and measurement has been used throughout this study. The SI uses meter-kilogram-second (MKS) as the units for length, mass, and time dimensions. Another system of units based on centimeter-gram-second (CGS) is also extensively used, especially in experimental studies. For the mechanical units of physics, such as force, velocity, momentum, acceleration, etc., straightforward conversions exist between units. These conversions preserve equation forms. To convert between the mechanical cgs and SI units, we only need to write the unit in terms of the fundamental units and then use the conversion coefficients (1m = 100 cm, 1kg = 1000 g, 1s = 1s), and derive the coefficient between the quantities. Table 2.1 lists the standard mechanical quantities and their conversion formula between cgs and SI units.

2.8.1 The SI View of Electromagnetic Units

Electricity and magnetism were understood as different phenomena and later unified as a single theory by special relativity. Thus, different equations existed for the forces arising from these phenomena. The electrostatic force between two charges is calculated by the inverse square distance relation:

$$F = k_C \frac{q_1 q_2}{r^2} \tag{2.114}$$

Where q_1 and q_2 are electric charges, r is the distance between the charges, and k_C is a constant with units depending on the units of electric charge and the length.

The magnetic force per unit of length between two long wires also follows a formula depending on the electric currents in the wires and the distance between them.

$$\frac{F}{L} = 2k_A \frac{I_1 I_2}{r} \tag{2.115}$$

Here $I_1$and I_2 are the electric currents in the wires, r is the distance between the wires, and k_A is a constant with the units depending on the units of the electric current and length. After the unification of electric and magnetic phenomena and understanding them as different parts of the electromagnetism theory, k_A and k_C were related with the following relation.

$$k_C = c^2 k_A \tag{2.116}$$

Where c is the speed of light.

The SI system treats the electric current as a fundamental quantity, such as length and mass. If we ascribe the units of Ampere (A) to electric current such that the force per length between each of the wires carrying 1 A and separated by 1 m distance is $2 \times 10^{-7} N\ m^{-1}$, we can define the electric charge unit such that 1 Coulomb = 1 A/s. With this choice of the electric charge unit, the electric charge of an electron is $e = 1.60 \times 10^{-19}\ C$. The value of k_A becomes $10^{-7}\ N\ A^{-2}$. Now we can define the permeability of the vacuum as

$$\mu_0 = 4\pi\ k_A = 4\pi\ \times 10^{-7}\ N\ A^{-2} \tag{2.117}$$

Thus

$$k_C = c^2 k_A = \frac{c^2}{4\pi}\mu_0 = 8.99 \times 10^9\ N\ m^2 A^{-2} s^{-2} \tag{2.118}$$

And the coefficient $1/(c^2\mu_0)$ is defined as the permittivity of the vacuum and denoted by ϵ_0.

2.8.2 The EMU-CGS view of Electromagnetic Units

The electric current and charge are not primitive quantities in the cgs units but are derived from the other three. Several approaches exist to define the units of electromagnetic quantities. In the EMU-CGS view, $k_A = 1$ is a unitless number. Thus, the unit of electric current in this system named Biot (Bi) or absolute ampere (abA) is defined such that two infinite thin wires carrying 1 Bi and placed 1 cm far apart exert 2 dyne/cm on each other.

$$1\ Bi = 1\ dyne^{\frac{1}{2}} = \ 1\ g^{\frac{1}{2}}\ cm^{\frac{1}{2}}\ s^{-1} \tag{2.119}$$

And the unit of electric charge is defined by $1\ Bi\ s = 1\ g^{\frac{1}{2}} cm^{\frac{1}{2}}$. The units of electromagnetic quantities in the EMU-CGS are shown in Table 2.2.

To calculate the conversion factor between Bi (CGS current unit) and A (SI current unit), we use equation (2.115) and note the definition of 1 A as the electric current value that produces $2\ \times 10^{-7} N\ m^{-1}$ for wires that are 1 m apart and 1Bi that produces 2 dynes for the wires that are 1cm apart, we get the scaling factor of $1\ A = 0.1\ Bi$

Table 2.1.Mechanical units of SI and cgs

Quantity (symbol)	Name: unit in cgs	Equivalent in SI
Velocity (v)	cm s^{-1}	10^{-2} m s^{-1}
Acceleration (a)	gal (cm s^{-2})	10^{-2} m s^{-2}
Force (F)	dyne (g cm s^{-2})	10^{-5} N(kg m s^{-2})
Energy (E)	erg (g cm^2 s^{-2})	10^{-7} J (kg m^2 s^{-2})
Pressure (P)	barye (g cm^{-1} s^{-2})	10^{-1} Pa (kg m^{-1} s^{-2})

The conversion between the cgs and SI units for electromagnetism is not as straightforward and needs derivations and explanations that we go through here.

Table 2.2. Conversion of common electromagnetic quantities from cgs to SI

Quantity (symbol)	unit in cgs	Equivalent in SI
Electric current (I)	1 Bi	10 A
Magnetic dipole moment ($\boldsymbol{\mu}$)	1 Bi cm^2 = 1 erg G^{-1}	10^{-3} A m
Magnetic Flux density (**B**)	1G : 1g Bi^{-1} s^{-2}	10^{-4} T: kg A^{-1} s^{-2}
Magnetic Field (**H**)	1Oe	$1/4\pi$ 10^3 A m^{-1}
Volume Magnetization (**M**)	emu cm^{-3}	1000 A m^{-1}

2.9 Computational Micromagnetics

The energy and effective field terms of section 2.7 cannot be calculated analytically except for simple geometries. Computational micromagnetics has arisen as a numerical tool for simulating the magnetization in nanometric to micrometric length scales.

Digital modeling of the continuum systems needs discretization to some extent. Two main methods have arisen for solving differential equations and modeling physical systems. The *finite difference* method divides geometry into evenly spaced cells, and each cell's physical properties are calculated. Each of these cells is a cuboid. On the other hand, the *finite element* method divides the geometry into subdomains and then recombines these subdomains to model the whole system. In this study, we have chosen the finite difference method since the cell structure of the finite difference models better simulates the lattice structure of real materials, the flat planar layers, and flat edges. Moreover, in the finite difference method, the control over the length scales of the cells is possible. This control is essential because of the short-range effects such as Heisenberg exchange and the DMI interaction.

2.9.1 Exchange Lengths

By discretization, geometry is divided into fixed-sized cells. The smaller cells allow higher accuracy while increasing the computational cost of the modeling. From the computational perspective, coarser cell size is desired since choosing bigger cells significantly decreases the simulation's computational complexity.

Since the exchange interaction is a strictly short-range interaction and does not go beyond several nanometers, the magnetostatic and magneto crystalline exchange lengths have been introduced as the hard caps on the size of cells.

Magnetostatic exchange length is:

$$l_{ex} = \sqrt{\frac{A_{ex}}{\mu_0 M_s^2}} \tag{2.120}$$

As seen in equation (2.120), this length arises from the square root of the exchange energy term to the magnetostatic energy of a single cell. For the crystals with uniaxial anisotropy, we can replace the magnetostatic energy density of the single cell with the anisotropy energy density; thus, another definition arises for the exchange length:

$$l_{exu} = \sqrt{\frac{A_{ex}}{K_u}} \tag{2.121}$$

This term is called the magnetocrystalline exchange length. When choosing a cell size for the system, one must calculate both lengths and select a cell size smaller than both.

2.9.2 Brown Thermal Fluctuations

The thermal noise realizes as normally distributed random effective field terms. These field terms can be calculated by this relation:

$$\boldsymbol{B_t} = \boldsymbol{\eta}\sqrt{\frac{2\alpha k_B T}{M_s \gamma \Delta V \Delta t}} \tag{2.122}$$

Where $\boldsymbol{\eta}$ is a vector with a random direction and a magnitude that follows the normal distribution. k_B is the Boltzmann constant, T is the temperature, ΔV is the cell volume, and Δt is the time step duration.

To have an estimation of the magnitude of $\boldsymbol{B}$ some calculations for a cobalt on platinum layer wit $\alpha = 0.3$ are put in Table 2.3

Table 2.3.Deterministic part of the thermal field based on example parameters.

Parameters	$\sqrt{\frac{2\alpha k_B T}{M_s \gamma \Delta V \Delta t}}$
T=300K, cell size = $1nm \times 1nm \times 1nm$ $\Delta t = 10^{-15}s$	220.7 T

T=300K, cell size = $4nm \times 4nm \times 4nm$ $\Delta t = 10^{-15}s$	27.5 T
T=600K, cell size = $4nm \times 4nm \times 4nm$ $\Delta t = 10^{-15}s$	39 T

2.9.3 Limitations of Micromagnetics

Micromagnetics is a continuum theory that has rendered accurate for the problems with length scales of several nanometers to micrometer scale. It is a semi-classical framework as it uses the continuum model while including quantum mechanical energies such as exchange and DMI. Micromagnetic limitations must be kept in mind before applying it to a specific problem. For the problems where the quantum effects become more important and the length scales are comparable to molecular sizes, atomistic models are the better choice. On the other end of the scale, where the length scales become bigger than several microns, the huge increase in the number of cells renders the modelling computationally prohibitive even for the modern computer systems.

The implicit assumption of the micromagnetic is that energy terms and the magnetization pattern are continuous and differentiable. This assumption challenges the results of the micromagnetic models for antiferromagnetic materials. Although there are studies that use micromagnetics for modelling these materials, the interpretation of results needs great care and scrutiny.

Micromagnetics also assumes the constant saturation magnetization for each cell. This assumption might also bring challenges when modelling ferrimagnets and antiferromagnetic materials. Even if the exchange length allows for a bigger cell size, if the cell cannot be estimated with a magnetization vector of a constant size, we must decrease the cell size to satisfy this condition.

2.10 Micromagnetic Software

The systematic approach to modeling the micromagnetic systems needs full-fledged software for scripting, model definition, model observation, and data extraction. Here we briefly introduce two main finite difference micromagnetic software and explain our choice for use in this thesis.

2.10.1 OOMMF

Object Oriented Micromagnetic Framework (OOMMF) is a micromagnetic framework designed at the Information Technology Laboratory at the National Institute of Standards and Technology (ITL/NIST) of the United States [116]. The computational engine is developed in C++ and the scripting and graphical user interface capabilities use the Tcl/Tk library. OOMMF uses CPU processing for the simulation of the micromagnetic systems. OOMMF is extensible, and new modules can be integrated into it by third-party developers.

The OOMMF Vector File (OVF) format has become the standard for saving the output of micromagnetic data.

2.10.2 MuMax3

MuMax3 is a new micromagnetic simulation software developed by the DyNaMat group at Ghent University. Mumax3 utilizes the GPU acceleration to reach several folds reduction in the computation time [115]. This is mainly possible because of the high efficiency of the Fast Fourier Transform (FFT) calculations on Graphical Processing Units (GPU). Calculating the demagnetization field is the most computationally intensive part of micromagnetic modeling. Since the calculation follows an integral with the form of convolution, efficient calculation of the FFT speeds up the computations. This increase in speed is achieved in MuMax3 by utilizing the parallel computing capabilities of NVDIA's CUDA framework.

MuMax3 is developed with Golang and uses Golang syntax for scripting. A complete and updated introduction to MuMax3 and the description of its API is on its website.

2.11 Micromagnetic Simulation Pipeline

2.11.1 Concepts

There are common entities in micromagnetic software. A **cell** is the smallest subdivision of space and is in the form of a cuboid. A **region** is an ensemble of connected or disconnected cells. There are multiple ways to define a region. In this thesis we have used image method to define regions because of the freedom and accuracy. The **mesh** is the repetitive pattern defining the subdivision of space. The **geometry** is the total space where the mesh resides. The points outside the geometry are considered as **vacuum**. A **field** has the similar meaning to its physical counterpart and means a quantity that has value at each point of space. Based on the type of a quantity, we can have either a **vector field** or a **scalar field.** Each vector field is a set of three scalar fields for its x, y, z components. The examples of vector fields are magnetization, effective field, demagnetization field, etc., and the examples of scalar fields are energy densities, parameters such as exchange energy constant, and any components of the vector fields, for example, the x component of the magnetization field.

2.11.2 Input

The input of a simulation describes the geometry, regions, parameters, timing, and the data to be recorded. The input can be in the form of a script text file, or an interactive command entered via the input box or the Graphical User Interface (GUI). Here we mainly use the file format input as it is more suited for more complex simulations and executing larger number of simulations. MuMax3 uses Golang syntax for scripting.

2.11.3 Output

The quantities of a simulation can be saved with a predetermined time step or at an arbitrary moment. The results are saved in formats based on the type of the quantity. A scalar or vector field can be saved in an OVF file in text or binary encoding. This file can be further processed with other tools for calculations or getting an image output. MuMax3 can directly save snapshot images of a field. A snapshot image has considerably lower size than the OVF file, but only contains the mapping between the field value and pixel intensities. This means that the image snapshot is only desirable for viewing the result and not applicable when we want to do calculations on the results. There are aggregate quantities such as the average of magnetization, the total topologic charge, the total energy, etc., These quantities have a single value at a moment, and they are saved in tables where the column specifies the quantity, and each row is the value of the quantity at the specified time for that row.

2.12 Introduction to Boolean Algebra

Boolean algebra, also known as Boolean Logic, is a branch of algebra dealing with values of "1"/true and "0"/false with the functions and operations concerning these values. Three primary operations of Boolean algebra are **multiplication**, **addition**, and **complement**. The multiplication and addition in Boolean algebra have the commutative, associative, and distributive properties of their numerical counterparts. The complement operator takes a single operand and changes it to "0"/"1" from "1"/"0". Table 2.4 shows the results of basic Boolean algebra operations with their possible operands.

2.12.1 Boolean Logic Gates

The two values of "1" and "0" in Boolean algebra can represent an electric wire's on/off state where the voltage over/below a specified threshold is considered "1"/"0". Thus, Boolean algebra can explain the operations in a complex electric system where the existence of voltage or current represents a signal, i.e., a Digital system.

The correspondence of the Boolean operations with logic statements has led to the names of AND, OR, and NOT for multiplication, addition, and complement operations, respectively. The relevant circuit schematic for each operation is devised to represent these operations in the digital logic circuits. Figure 2.11 part (a) shows the schematics of the three primary logic operations. Part (b) shows three other common logic gates. The gates in part (b) can be expressed in terms of the gates in part (a)

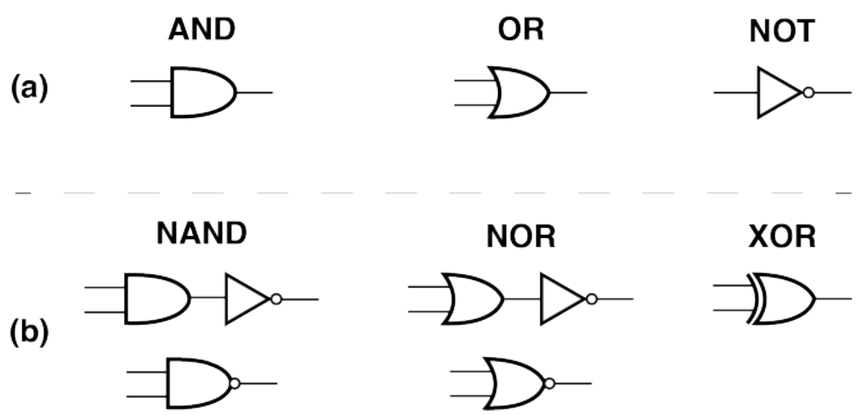

Figure 2.11. Boolean logic gates. (a) the schematics for primary Boolean operations. (b) NAND, NOR, and XOR gates.

Table 2.4.The basic Boolean algebra operations and their results

Operation	Operand 1	Operand 2	Symbol
Addition (OR)	0	0	$0+0=0$
	0	1	$0+1=1$
	1	0	$1+0=1$
	1	1	$1+1=1$
Multiplication (AND)	0	0	$0\times 0=0$
	0	1	$0\times 1=0$
	1	0	$1\times 0=0$
	1	1	$1\times 1=1$
Complement (NOT)	1		$\overline{1}=0$
	0		$\overline{0}=1$

2.12.2 Boolean Functions

Boolean functions are mathematical functions with the set of 0,1 as their domain and range. Three primary Boolean operations can express every Boolean function. The gates introduced here can also be expressed in the function notation. Table 2.5 summarizes the functional notation of the gates in Figure 2.11.

Table 2.5.The function form of the Boolean gates and their equations

Gate	Function equation
OR	$OR(a,b)=a+b$
AND	$AND(a,b)=ab$
NOT	$NOT(a)=\bar{a}$
NOR	$NOR(a,b)=\overline{a+b}=\bar{a}\,\bar{b}$
NAND	$NAND(a,b)=\overline{ab}=\bar{a}+\bar{b}$
XOR	$XOR(a,b)=a\oplus b=a\bar{b}+\bar{a}b$
XNOR	$XNOR(a,b)=a\overline{\oplus}b=ab+\bar{a}\bar{b}$

2.12.3 Truth Table of a Boolean Function

Since the domain of the Boolean functions is a discrete set with 2^n number of elements where n is the number of inputs, the function can be completely represented by a table with two columns where the first column is the input, and the second column is the output. Table 2.6 shows the truth tables for the gates of Table 2.5.

Table 2.6.The truth table of conventional gates

ab	OR(a,b)	AND(a,b)	NAND(a,b)	NOR(a,b)	XOR(a,b)	XNOR(a,b)
00	0	0	1	1	0	1
01	1	0	1	0	1	0
10	1	0	1	0	1	0
11	1	1	0	0	0	1

2.12.4 Universal Set of Gates

A universal set of gates is a gate or a set of gates that can be used to construct an arbitrary Boolean function. From our discussion, we know that the set of AND, OR, and NOT gates is a universal set of gates. One can ask whether the universal set of gates is unique to these three gates. It is not; there are other universal sets of gates. One can also wonder if there is a single gate that constitutes a universal set. Yes, there are such sets. NAND and NOR each are universal.

It is trivial that if we can make each member of a universal set by the members of one set, the set is universal too. Here we prove that the NOR gate is universal. By the output of the following three equations, one can verify the correctness of these statements.

$$OR(a,b) = NOR(NOR(a,b), NOR(a,b)) \tag{2.123}$$

$$AND(a,b) = NOR(NOR(a,a), NOR(b,b)) \tag{2.124}$$.

$$NOT(a) = NOR(a,a) \tag{2.125}$$

Figure 2.12 shows the circuit for universal gates of AND, OR, NOT made up of NOR gates. Other gates such as NAND, XOR, and XNOR can also be made from NOR gates. NAND gate by itself is a universal gate and can be used to make other gates.

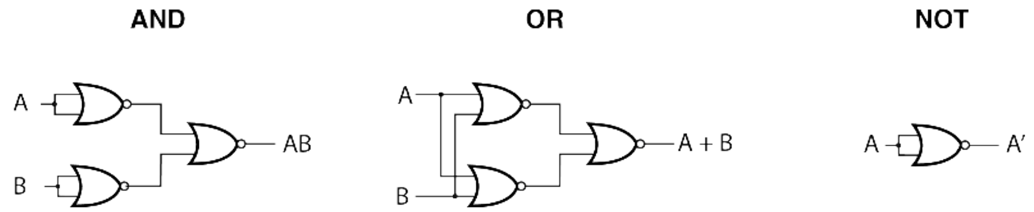

Figure 2.12. AND, OR, NOT gates by NOR gate. The combination of NOR gates can make up the universal set of AND, OR, NOT gates.

2.13 Application Dependencies

This section is devoted to the application dependencies of this thesis. The applications are developed in Python 3.

2.13.1 Python

Python is a general-purpose, interpreted, strongly and dynamically typed programming language famous for its simplicity, rich ecosystem, and active community. The packages for managing the micromagnetic simulation and simulating the behavior of the logic gates are developed using Python. In this work, we use Python 3.6+ and recommend that the provided packages be installed in this version of Python. The main power of Python comes with its packages. The following packages have been extensively used in our application development:

- Numpy: a tool for numerical operations in Python. Numpy is unofficially known as MATLAB® in Python.
- Pandas: a tool for data wrangling and modification in Python. Datafarmes are the central object in Pandas. Pandas is also unofficially known as R (or excel) in Python.
- OpenCV: a high-performance image modification written primarily in C++ with different application programming interfaces (API) for languages such as Python.
- Matplotlib: the main visualization library for Python
- Pickle: an object serialization and compression for Python
- Graphviz: a graphing tool using the DOT language.
- Jupyter Notebook: a notebook development environment to share python codes. The tutorials related to this thesis are provided in the form of Notebooks.

2.14 Summary

This chapter went through the foundations, theories, and tools used in this thesis. The main constituents of this chapter were magnetism, micromagnetism, computational micromagnetism, Boolean algebra, software frameworks, and software used in developing the programs needed for this study.

The first topic to present was the classical description of magnetism because magnetism is a phenomenon with macroscopic manifestation. The close relation between magnetism and angular momentum was presented, and the relevant formulae were deduced.

A brief introduction to the quantum mechanics representation of angular momentum followed. Then, the theory of electron spin and its implications were presented. Two primary differences in the quantum mechanical description of magnetism from the classical description, i.e., the g-factor correction and the deviation of the magnetization vector from the angular momentum vector based on the value of the g-factor, were also discussed. The value of the resulting g-factor for the systems with both orbital and spin angular momentums was then presented.

The LLG equation was derived as the natural consequence of the relation between angular momentum and magnetization. The LLG equation and the fundamental description of magnetism set the stage for the theory of micromagnetism.

The interactions between magnetic moments and between magnetic moments and external forces produce energy terms. These energies produce different phenomena in magnetic materials and render these materials a rich host for these phenomena. This chapter first reviewed the analytical forms of these energies for separate moments. Then, the micromagnetics framework as the continuum theory of magnetization was introduced. The finite difference method for modeling the magnetic systems was then reviewed.

Although the SI system has been used throughout this thesis, a brief introduction of the cgs system was also provided as the cgs system is used more extensively in experimental studies.

The computational micromagnetics and the modeling software frameworks were introduced, and our reasons for choosing MuMax3 as our primary software framework was briefly discussed.

Because of the central role of Boolean algebra throughout the thesis, a brief introduction to this theory was provided. This introduction included the conventional functions and gates, their truth table, and the concept of a universal set of gates. This concept becomes important in later chapters when we introduce our single-element universal set of gates.

The multitude of software tools used in this study was then listed with a brief explanation. The relevance of these tools becomes more critical in the later chapters when the systematic study of devices and the framework and tools developed in this thesis are presented.

This chapter served two purposes: setting the theoretical foundation of this thesis and listing the tools needed for the study. Many of this thesis's programming or physics aspects are chapter-related and wouldn't fit in this chapter. Putting them in this chapter would increase the bulk of this chapter beyond its purpose. It would also increase the divergence of materials and impair this chapter's focus and generality. Thus, the detailed relevant material was decided to be put to their specific chapters.

Chapter 3

THE SKYRMION GENERATOR

3.1 Introduction

The skyrmion generator is the first device that we explain. This chapter is devoted to the analysis of the skyrmion generator. This design serves as a current-driven (periodic or aperiodic) skyrmion source. It can also be used for digital skyrmion clock generation.

Magnetic skyrmions are chiral spin patterns with non-zero topological charge [5]. Topological charge is defined as:

$$\mathrm{N} = \frac{1}{4\pi}\int \mathrm{d}^2\mathrm{r}\mathbf{m}.\left(\frac{\partial\mathbf{m}}{\partial \mathrm{x}} \times \frac{\partial\mathbf{m}}{\partial \mathrm{y}}\right) \quad (3.1)$$

Where r is the distance from the origin, **m** is the normalized magnetization and x, y are the coordinate components of the plane of the magnetic film. The competition between chiral and collinear forces gives rise to skyrmions. The collinear energy term can be the Heisenberg exchange interaction [9, 11, 42] or dipolar interaction [117, 118] and the chiral interaction is the bulk or interfacial Dzyaloshinskii-Moriya Interaction (DMI). For materials with non-zero perpendicular magnetic anisotropy, and interfacial DMI, Néel skyrmions arise while Bloch skyrmions emerge with bulk DMI [110, 111]. Materials with in-plane anisotropy can also host skyrmions [119]. Skyrmions were first observed in a lattice in MnSi that possesses bulk type DMI which arises from non-centrosymmetric crystal structures [12, 13, 120, 121]. Single skyrmions were then observed in multilayers of heave metals (HM) and Ferromagnets (FM) [43, 122]. The topological protection of skyrmions has allowed them the room temperature stability that bolsters their attraction as the next-generation information carriers or data signals.

Skyrmions are the subject of intensive research due to their many appealing features, such as their nanometer diameters, which enable high-density storage, as well as their stability at room temperature [14, 60, 123, 124], low-power current-controlled motion [46, 125, 126], and their robustness against geometric or material defects [16, 127]. Skyrmions are also detectable through different means such magnetic force microscopy (MFM) [128], soft x-ray scattering [129, 130], and Lorentz transmission electron microscopy [13, 131].

The elimination of the skyrmion Hall effect lays the groundwork for the development of racetrack devices that rely on skyrmions, which could push the skyrmionics to reach to speeds and efficiencies that transcend the Moore's law [65, 132-136].

Various methods for initiating skyrmion formation have been suggested and exhibited by researchers. These methods involve using spin transfer torques to generate skyrmions from the edge of a notch [57], injecting vertical spin currents [16, 137, 138], applying electric field pulses [139], creating skyrmions through a constriction using the flow of electric spin-polarized current at a geometric narrow channel [69, 70], domain wall (DW) bending at the junction between narrow and wider channels, using electric current for nucleation in multilayers [140], and secondary skyrmion resulting from a DW with a magnetic field [68].

In this chapter, we introduce a new method for producing skyrmions in computational micromagnetic models. The approach involves using a combination of DW pinning and DW-to-skyrmion conversion. The drive of the system is spin-polarized current that with combination of the specific geometry leads to skyrmion generation with desired frequency. The process begins by initializing a skyrmion that moves to a channel. The narrow channel turns the skyrmion into a magnetic domain. This magnetic domain has two opposite-chirality walls. A pinning notch fixes one DW and the other DW moves further. This expands the magnetic domain. Further applying the spin-polarized charge current to the domain profile, will eventually causes skyrmion generation because of the special geometry of the device. The skyrmion generation rate can be adjusted by the adjusting the current density in a reversible manner. This process happens without the presence of an external magnetic field.

3.2 Domain Wall Expansion

Prior investigations into the motion of nanoscale domain walls (DWs) have unveiled various fascinating characteristics, such as the ability of DWs to be pinned by indentations, notches, and kinks. It has been demonstrated that notches and other structural irregularities can hinder DW movement, and the depinning energy is influenced by the DW's chirality [141]. These findings have opened avenues for utilizing magnetic domain expansion to induce magnetization switching by electrical stimulus. The magnetic domain expansion is the foundation of skyrmion generation in this chapter.

The square notch of the device creates an energy step that hinders the movement of a DW. For each notch shape and DW there exists a current density that can depin the domain wall from the notch. In this section, these depinning current densities are found for both DWs. The findings show that the depinning current density for the right DW, j_R, is lower than that of the left DW, j_L. If the current is less than j_R, the right DW stops at the notch. Since both domain walls are pushed towards the right, the left DW approaches the right DW. Thus, the magnetic domain decreases in size and disappears. This is shown in the supplementary movie S3.2 (Supplementary movie 2 in [90]).

On the other hand, the currents that exceed the j_L are of sufficient magnitude to propel both walls from the notch i.e., the magnetic domain moves past the notch. This is shown in the supplementary movie S3.3 (Supplementary movie 3 in [90]). Based on these facts, a current density that leads into the domain expansion must be between j_R and j_L, with this current, the right DW can cross the notch, but the left DW is pinned. This leads to the expansion of the magnetic domain which is desirable for the operation of the generator. This is shown in the supplementary movie S3.1 (Supplementary movie 1 in [90]). For the magnetic parameters and the nominal dimensions of Figure 3.1, $j_R = 1.10 \times 10^{12}\ \mathrm{A \cdot m^{-2}}$ and $j_L = 1.72 \times 10^{12}\ \mathrm{A \cdot m^{-2}}$.

Charge carriers (electrons) move both skyrmions and domain walls in their direction of movement. Here we start with a skyrmion and push it into the channel with spin-polarize current. Prior studies have revealed that forcing a skyrmion into a channel with a diameter smaller than its own causes the skyrmion's topological protection to break down [68]. The narrow channel that skyrmion is pushed into, breaks down the topological protection of the skyrmion and turns it into a magnetic domain. The current density that pushes the walls is between j_R and j_L that results in the pinning of left DW and moving of the right DW which results into the domain expansion. The DMI of the system determines the type of skyrmion and the resulting domain walls. For interfacial (bulk) DMI

Néel (Bloch) skyrmions emerge, and the resulting DWs will be Néel (Bloch) as well. Here we use interfacial DMI. Thus, the skyrmions and DWs are of Néel type.

3.3 Periodic Skyrmion Generation

The device's design and the skyrmion generation process are illustrated in Figure 3.1. Figure 3.1(a) shows the geometry of the device. It is composed of several parts, including the input track, the notch channel, reservoir, output channel, and the output track from left to right.

Figure 3.1(b) depicts the skyrmion generation process. To generate skyrmions, we first stabilize one at the input track. Then a spin-polarized DC current is applied with a density of $\mathrm{j} = 1.4 \times 10^{12} \mathrm{A} \cdot \mathrm{m}^{-2}$. This value which falls between j_R and j_L that results into the magnetic domain expansion. Since the magnetic textures move with the electrons, the current must move from right to left. The current pushes the skyrmion into the narrow channel. The channel transforms it into a magnetic domain. The current is greater than j_R. Thus, the right domain wall passes the notch. The current is smaller than j_L and the left DW pins to the notch. This leads into the domain expansion.

The extending magnetic domain moves into the reservoir. This extension continues until it reaches the right side of the reservoir. When the right side of the reservoir hinders the horizontal expansion of the magnetic domain, it expands in vertical direction that leads to the creation of a magnetic domain at the input of the output channel. When the vertically extended domain covers the entrance of the output track, the current pinches it out of the main domain into the output channel. The current further pushes this domain to the right of the output channel. When it reaches the output track a skyrmion forms. The process of vertical expansion of the main domain, pinching a domain and moving it to the output track continues while the DC current is applied. This results in the repeated formation of skyrmions. This operation with nominal values is shown in the supplementary movie S3.4 (Supplementary movie 4 in [90]).

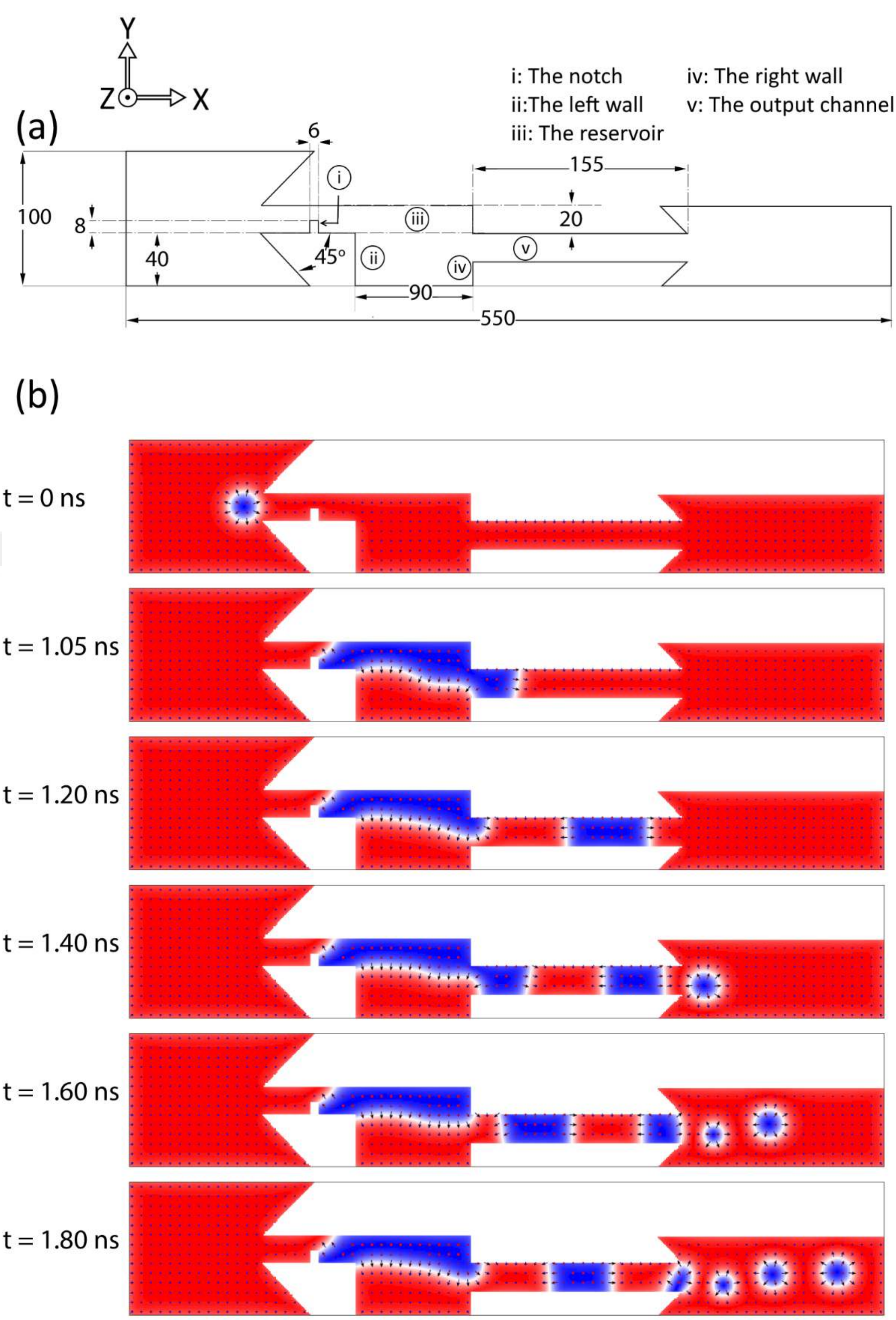

Figure 3.1. The skyrmion generator process. (a) Device blueprint. All the dimensions are in nanometers (b) The periodic skyrmion generation with the current density that lies between $j_R = 1.32 \times 10^{12}\ A \cdot m^{-2}$ and $j_W = 1.73 \times 10^{12}\ A \cdot m^{-2}$ with this current density, the left DW pins to the notch in the input channel[90].

3.4 Operational regimes

Different energy barriers arise from the complex geometry of the device, which result in multiple operational regimes. An important threshold is the current threshold that can overcome the repulsion arising from the right side of the reservoir. This current threshold is $j_{Rw} = 1.32 \times 10^{12} \mathrm{A \cdot m^{-2}}$. The magnetic domain stops before the right side of the reservoir for smaller current density values. Figure 3.2 (a) shows this situation for $j = 1.30 \times 10^{12} \mathrm{A \cdot m^{-2}}$. This situation is shown in the supplementary movie S3.5 (Supplementary movie 5 in [90]).

Another situation with out-of-range currents is when the current is greater than j_L. In this situation, both DWs pass the notch and since the protrusion at the junction between the input track and reservoir acts as an anti-notch with its own pinning potential, the left domain wall pins to it. Figure 3.2 (b) shows this situation. This situation is shown in the supplementary movie S3.6 (Supplementary movie 6 in [90]). This condition remains stable until the current density reaches $j_W = 2.73 \times 10^{12}\ \mathrm{A \cdot m^{-2}}$. At this point, the domain is depinned, and it moves towards the right until it reaches the right wall of the reservoir, where it disappears. This situation is shown in the supplementary movie S3.7 (Supplementary movie 7 in [90]).

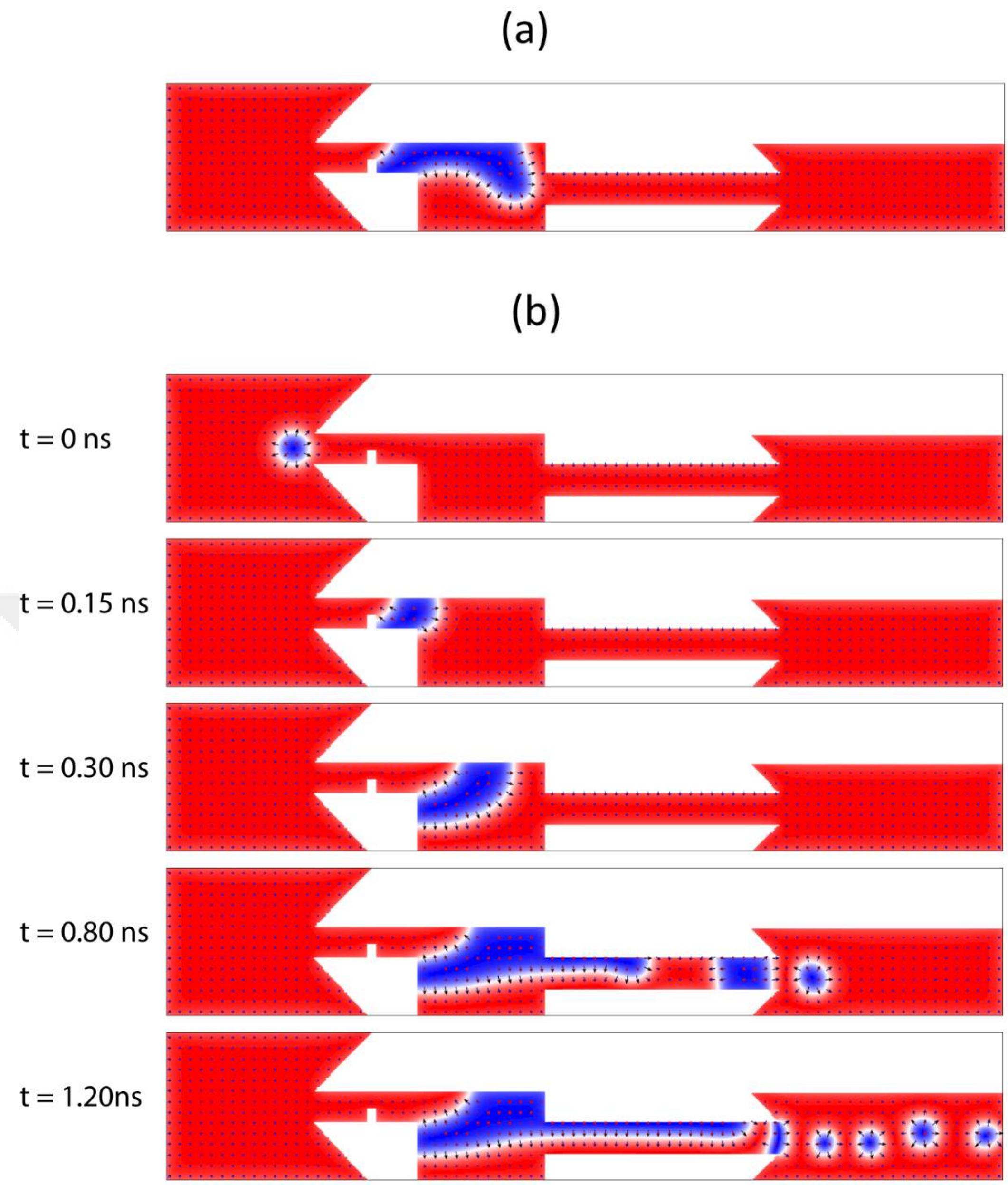

Figure 3.2.Operation regimes driven by lower and higher currents. (a) The magnetic domain does not fill the reservoir if the current density is smaller than $j_R = 1.32 \times 10^{12}\ \mathrm{A \cdot m^{-2}}$ (b) The left DW unpins from the notch and pins at the left side of the reservoir for current densities over $j_W = 1.80 \times 10^{12}\ \mathrm{A \cdot m^{-2}}$[90].

The device operates according to the following principles:

1. The notch pins the left DW.
2. The direct spin-polarized current, causes the magnetic domain to expand.
3. The magnetic domain stops at the right wall of the reservoir.
4. The domain also expands in +x direction.
5. The domain ultimately reaches the output channel.

6. The DC current pinches a part of the domain into the output channel.
7. The DC current moves the detached domain to form a skyrmion in the output track.

The process of steps from 4 to 7 is a repetitive cycle that results in the creation of periodic skyrmions. The frequency at which skyrmions are generated is influenced by the timing of these steps, which in turn is determined by several factors such as the applied current, material properties, and geometric properties. Later in the chapter, we explore how the application of current density and the damping coefficient affect this frequency. We study the effect of the Cobalt layer thickness (ranging from 1 to 4 nm) on the operation of the skyrmion generator.

3.5 Alternative Operation Regimes and DMI Type

The geometry, initial conditions, and the current density values presented here are nominal values, but the device can work with some variation to these values. The figures and movies of this section can be found in the supplementary materials of our skyrmion generator paper [90]. Different operation regimes are:

1- The device can be initialized with a magnetic domain rather than a skyrmion. Movie S3.9 (Supplementary movie 9 in [90]) shows this situation. Movie S3.10 (Supplementary movie 10 in [90]) also shows this situation without the notch in the channel.

2- Although the nominal values of the operation result in the notch pinning of the left DW, the DW can also be pinned to the reservoir wall as shown in Figure 3.2. This is shown in supplementary movie S3.6 (Supplementary movie 6 in [90]). The pinning to the right side of the reservoir also can happen if the notch is not present in the input channel. This can happen because of some defect in the fabrication process. The working of the device without a notch is shown in movie S3.11 (Supplementary movie 11 in [90]).

3- The junctions can assume right angles instead of 45° vertices. This can simplify the fabrication of the device. The successful operation of the generator in this situation is shown in Movie S3.12 (Supplementary movie 12 in [90]).

4- The DMI type determines the skyrmion and DW type. The interfacial and bulk DMIs result in Néel and Bloch type skyrmions and walls. Since this work focuses on multilayers, the main presentation is for the interfacial DMI but the results for the bulk DMI are identical with the interfacial. Supplementary movie S3.14 shows the results with bulk DMI. The main results of this work are obtained with interfacial DMI, but the results are the same with the bulk DMI too. A sample of the operation of the device with bulk DMI and bloch skyrmions and DWs is shown in movie S3.13 (Supplementary movie 13 in [90])

3.6 The Frequency of Skyrmion Generation

The frequency of skyrmion generation is influenced by the speed in which device's operation moves through step 4 to step 7 of the section 3.3. If the parameters of the material, geometry, and current density are arranged in a way that promotes quicker insertion of domains into the output channel, then the frequency of skyrmion generation will be higher. Altering the applied current allows for the adjustment of this timing. Increasing the applied current leads to an increase in the speed of domain expansion. As a result, the frequency of generating skyrmions is expected to increase by increasing the current density.

3.6.1 Skyrmion Generation Frequency for Nominal Values

The nominal parameters for the device are interfacial DMI and 1nm thick nanotrack. Figure 3.3 (a) displays the relationship between the frequency of skyrmion generation and the applied current for these parameters. The frequency of skyrmion generation grows proportionally with the applied current in the normal operational mode. For the low-current operational mode it has a higher square root shape and is illustrated in Figure 3.3 (b).

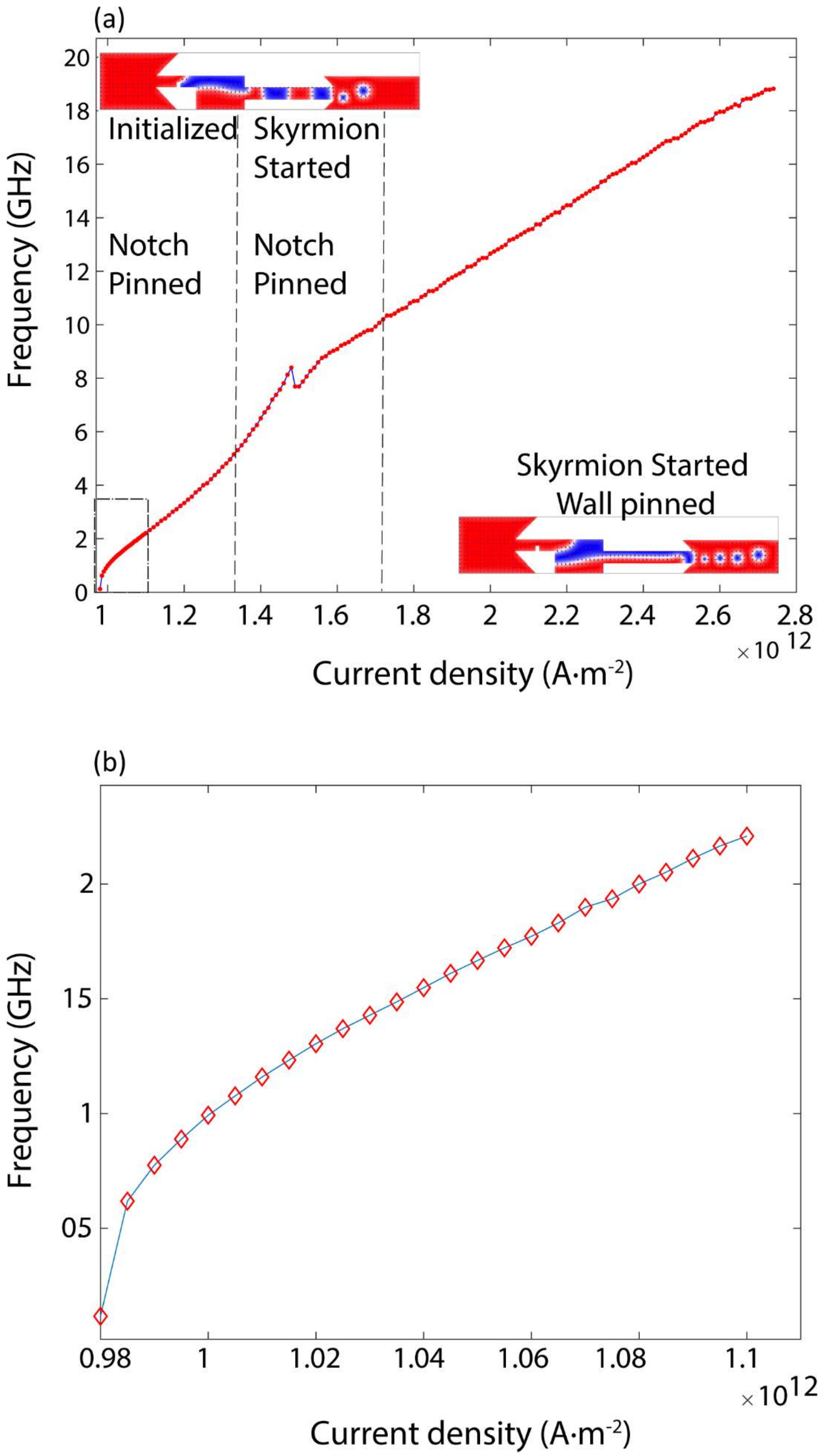

Figure 3.3. Input current density dependence of skyrmion generation frequency. (a) The rate of skyrmion generation dependence on the applied current density. The value of damping α is 0.3. The current

densities that produce skyrmions are between $j = 9.80254 \times 10^{11}\ A \cdot m^{-2}$ that corresponds to $f = 114$ MHz and $j = 2.74 \times 10^{12}\ A \cdot m^{-2}$ that corresponds to $f = 18.881$ GHz. (b) the magnified plot for the dashed rectangle in the part a. For this lower current density region, the skyrmion generation frequency has a square root dependence on the applied current density [90].

3.6.2 Skyrmion Generation Frequency for Bulk DMI

The skyrmion generation frequency for the material with bulk DMI which results in Bloch skyrmions is very similar to the skyrmion generation frequency for the interfacial DMI and Néel type skyrmions. The skyrmion generation frequency for Bloch and Néel type skyrmions are shown in Figure 3.4. As this figure shows, the generation frequencies are very similar for the two types of skyrmions.

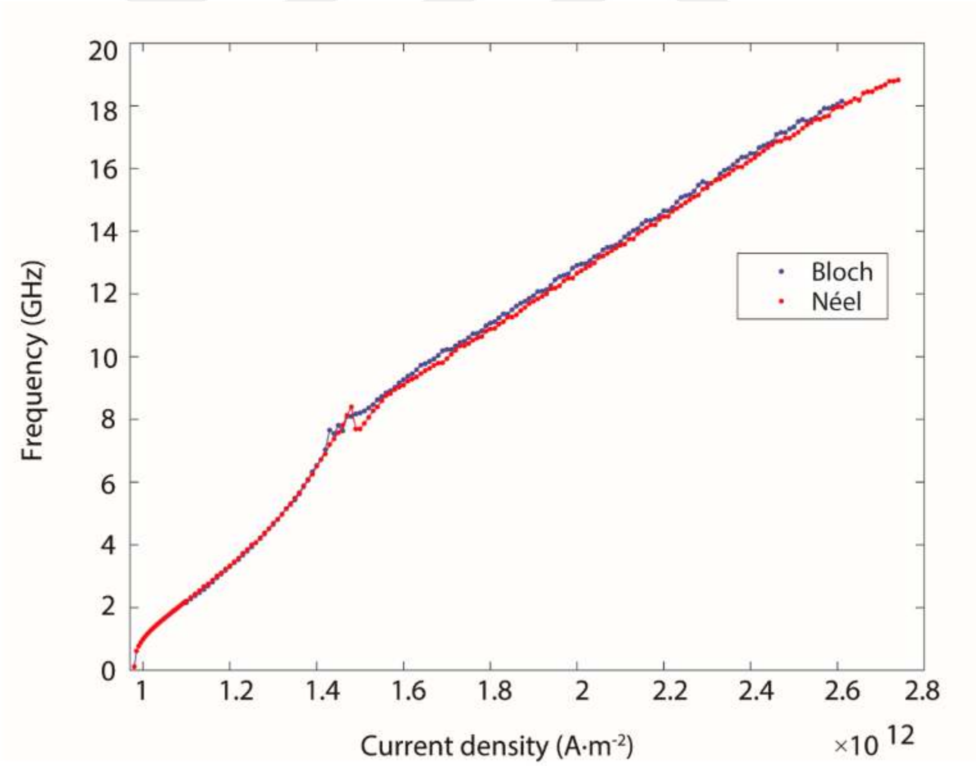

Figure 3.4. Skyrmion generation frequency for Bloch and Néel type skyrmions. The skyrmion generation frequencies for both types of skyrmions are very similar for all the current density values[90]

3.6.3 Skyrmion Generation Frequency for 4 nm Nanotracks

Since increasing the nanotrack thickness to 4 nm is essential for the finite temperature stability, The skyrmion generation frequency for this thickness also needs to be investigated. Figure 3.5 shows the skyrmion generation frequency for the devices with 1nm and 4 nm thickness. As this figure shows, the device with 4 nm thickness has lower frequency of skyrmion generation. The minimum current for skyrmion generation is also slightly higher for the 4 nm thick device. The lower frequency for thicker device can be ascribed to the lower demagnetization field. If we write the LLG equation including the spin transfer torques we have

$$\dot{\boldsymbol{m}} = \gamma_{LL} \frac{1}{1+\alpha^2}\left(\boldsymbol{m} \times \boldsymbol{B}_{eff} + \alpha\left(\boldsymbol{m} \times \left(\boldsymbol{m} \times \boldsymbol{B}_{eff}\right)\right)\right) + \tau_{STT} \qquad (3.2)$$

Where τ_{STT} stands for the spin transfer torques and $\boldsymbol{B}_{eff}$ is the effective magnetic flux density. With higher thickness, the demagnetizing field will be lower in the layer. When the demagnetization field is lower, the $\boldsymbol{B}_{eff}$ is more inclined towards the bulk magnetization of the film. This results in an increased resistance against the spin transfer torques that tend to deflect the magnetization to move the magnetic textures such as skyrmions and domain walls. Thus, moving these magnetic textures with the same speed needs higher current density. This results in the lower speed with the same current and thus lower skyrmion generation frequency.

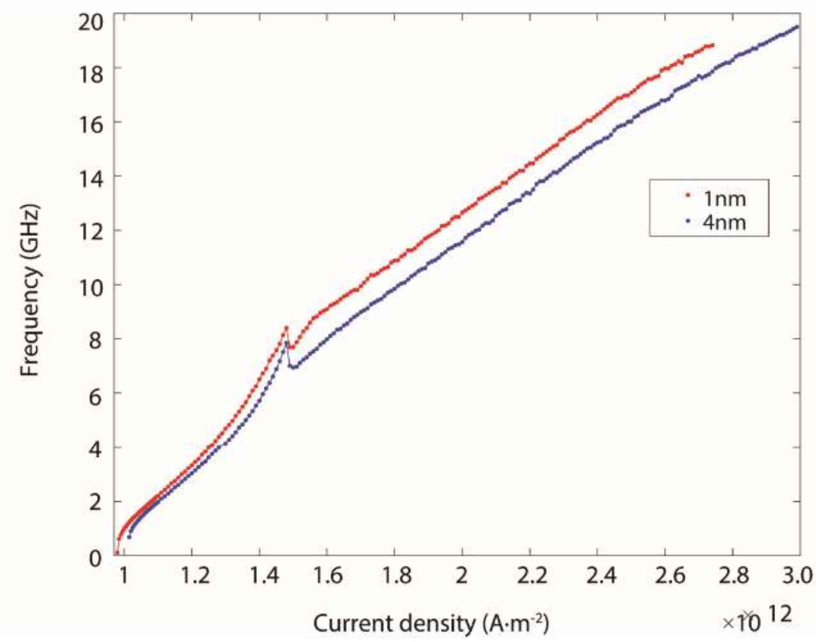

Figure 3.5. Skyrmion generation frequency for devices with 1 nm and 4 nm thickness. The generation frequency for the 4 nm nanotrack is

smaller than of the devices with 1 nm thickness and it starts from a slightly higher current threshold[90].

Skyrmion Generation for Lower Currents

If the starting applied current is less than $1.32 \times 10^{12} \mathrm{A \cdot m^{-2}}$ that is the threshold of bringing the right DW to the right side of the reservoir, skyrmions cannot be generated. However, if a greater current pulse is applied at first to expand the magnetic domain to the right side of the reservoir, lower currents can be used to generate skyrmions. The current pulses for the skyrmion generation with this scheme are shown in Figure 3.6. Initially, a current with the density of j=$1.40 \times 10^{12} \mathrm{A \cdot m^{-2}}$ is used to fill the reservoir width with the magnetic domain. After 1.89 ns, the current is reduced to $0.97 \times 10^{12} \mathrm{A \cdot m^{-2}}$, which is sufficient to clear the remaining skyrmions in the output channel and track while not big enough to produce skyrmions. After this initialization, higher currents can be used to generate skyrmions with lower frequencies. For example, a 114 MHz frequency can be reached with the current density of j=$9.80254 \times 10^{11} \mathrm{A \cdot m^{-2}}$.

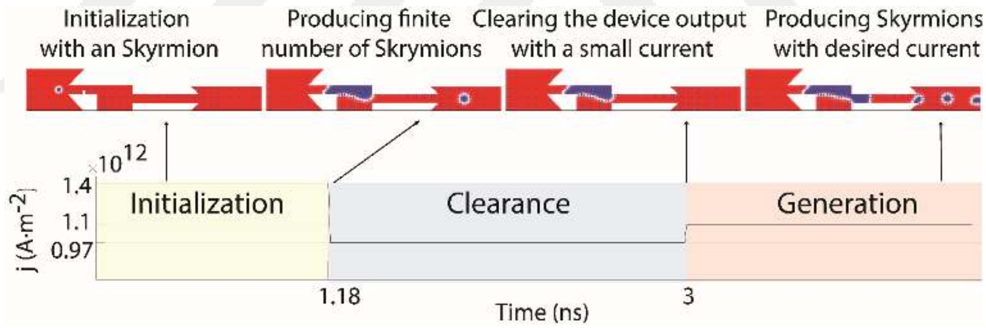

Figure 3.6.Skyrmion generation for lower currents. The skyrmion generation frequency can be tuned for currents lower $1.32 \times 10^{12} \mathrm{A\, m^{-2}}$ by initializing the device with a higher current to fill the reservoir. The initialization current density here is $1.40 \times 10^{12} \mathrm{A \cdot m^{-2}}$, then a current with density of $9.7 \times 10^{11} \mathrm{A \cdot m^{-2}}$ is applied to clear remaining skyrmions. The skyrmion generation frequency can be tuned by applying the desired current pulses. For example, here a current with the density of $1.1 \times 10^{12} \mathrm{A \cdot m^{-2}}$ has been applied [90].

As previously mentioned, the frequency at which skyrmions are generated is determined by the density of the current being applied. Moreover, the frequency of skyrmion generation may also be influenced by essential material properties such as the damping parameter. If all parameters are held constant, increasing the current density will result in a higher frequency of skyrmion generation according to Figure 3.3 (a).

The skyrmion generation conditions are also affected by the damping coefficient α, which can change in different material compositions and deposition conditions. Figure 3.7 displays the impact of both the damping parameter and applied current on the frequency of skyrmion generation. In the shaded areas of the graph, either no skyrmions are produced or only a limited number are formed. Various scenarios where this behavior occurs are identified in in Figure 3.7 (a) and their corresponding cases are depicted in Figure 3.7(b).

Within the region 1, the magnetic domain shifts towards the right of the reservoir until it disappears as shown in supplementary movie S3.8. It is observed that increasing the damping coefficient leads to a decrease in the threshold current density values, causing the domain to depin with a smaller current. When the damping coefficient is higher, the frequency of skyrmion generation decreases for a constant applied current.

Region 2 displays the scenarios for smaller and larger values of α. In this case, the minimum current required to generate skyrmions is dependent on the α value. Although the magnetic domain expands into the output channel, there is no occurrence of pinching, and thus no skyrmions are produced.

Regions 3 and 4 demonstrate an intriguing correlation between the alpha value and current density thresholds. In Region 3, the left domain wall is pinned to the notch, but the applied current is insufficient to move the domain wall to the right reservoir wall. The situation in region 4 is similar, with the domain wall being pinned to the left wall. Additionally, there are different thresholds for the domain to reach the right reservoir wall, in addition to the pinning thresholds for the notch and right wall. In region 5, the threshold for the expansion of the magnetic domain is so low that it extends into the output section.

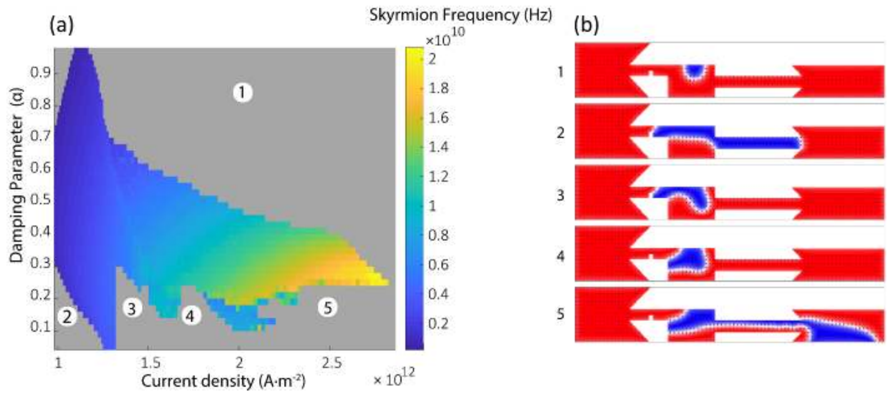

Figure 3.7. Skyrmion generation frequency based on input current and damping coefficient. (a) Skyrmion generation frequency dependence on current density and Gilbert damping α. Colorbar shows the generated skyrmion frequency. Gray regions show failed cases with no skyrmion of finite number of skyrmions. (b) The device's magnetic state examples for different cases of part (a) [90].

3.7 Skyrmion Energy Analysis

To generate a skyrmion for the geometry shown in Figure 3.1, several energy barriers must be overcome, including the energy for the DWs to pass the notch, the energy to expand the magnetic domain, the energy to fill the reservoir, pinching energy, and skyrmion nucleation energy. To advance information processing beyond the limitations of Moore's Law, it is essential for each bit to consume the least amount of energy, ideally approaching Landauer's limit of $k_BT\ln(2)$. However, most current information processing devices' energy consumption surpasses several orders of magnitude more than this limit. The skyrmion nucleation energy is close to Landauer's limit and thus has a potential to lower the energy consumption significantly. This section focuses on the energy required for skyrmion generation, the initialization energy of the device which is the energy to fill the reservoir before the generation of the first skyrmion is 1.12×10^{-19} Joules. After this initialization step, the marginal energy cost of generating each skyrmion is 1.94×10^{-19} Joules. This energy is approximately $67.5 \times k_BT\ln(2)$, where T = 300 K. This means that skyrmions can be used as ultralow-energy information bits in the room temperature. This calculation excludes Joule heating, which is considered separately in this chapter. Since other types of materials such as magnetic insulators can potentially replace the ferromagnetic

Cobalt and these materials can be used in conjunction with pure spin currents, this potential for low energy information processing can be reached by using these materials instead of Co/Pt bilayer.

A recent model has been developed to determine the energy of a skyrmion, where the equilibrium energy is determined by the exchange interaction coefficient, A, the layer thickness, d, and a constant, k, which is specific to the type of skyrmion produced [142]. In that study the energy of skyrmion is E=kAd. For our device with a material thickness of 1 nm, the exchange interaction coefficient of 15 pJ/m, $k=1.94 \times 10^{-19}/(15 \times 10^{-12} \times 1 \times 10^{-9}) = 12.9$. When the material thickness is increased to 4 nm, the skyrmion energy becomes 7.76×10^{-19} Joules while keeping k constant at 12.9.

3.8 Room Temperature Thermal Effects

The skyrmion generator of this chapter is a nano-scale device. The model contains Cobalt layers of 1 nm thickness. The models were conducted without the effect of the room temperature noises. However, when modeling real devices, the room temperature noise and Joule heating effects both need to be taken into consideration. Once we modeled the operation of the device with room temperature effects, we discovered that increasing the thickness of the cobalt layer to 4 nm for the same geometry improves the device's ability to withstand stochastic temperature effects. Supplementary Movie S3.8 (Supplementary movie 8 in [90]) demonstrates the device's operation at room temperature with a 4 nm cobalt layer. Increasing the cobalt layer’s thickness does not hinder the device operation but results in the increase in power consumption due to higher Joule heating.

3.8.1 Equilibrium Temperature

The flow of current in the device results in the Joule heating. The dissipated power from the Joule heating in a rectangular nanotrack can be deduced using:

$$P_{in} = I^2R = \frac{(Jwd)^2\rho l}{wd} \tag{3.3}$$

Where I is the electric current flowing in the track, R is the ohmic resistance, w is the track width, d is the layer thickness, ρ is the resistivity of the material, and J is the in-plane current flowing in the layer. The ohmic resistance can be deduced by breaking the device into different rectangular regions. Using the resistivity of the Platinum and Cobalt layers presented in Table 3.1 The ohmic resistance is 1677 Ω for a device with 4nm Cobalt and 4nm Platinum layers. The Joule heating power for these values is 9 mW.

This Joule heating can result in an indefinite increase in the temperature if there is not a thermal energy drain. Radiation, convection, and thermal conduction are the ways that the device can lose thermal energy. The amount of energy loss for the radiation and convection are negligible in comparison with conduction. If the nanotrack is in contact with a constant temperature heat sink, the energy output of the system by conduction is:

$$P_{out} = \frac{k\Delta T A}{d} = \frac{kwl\Delta T}{d} \tag{3.4}$$

If we want the temperature of the layer not to change, we need the output power to be equal to the input power; thus, for a rectangular track, we have:

$$\frac{(Jwd)^2 \rho l}{wd} = \frac{kwl\Delta T}{d} \rightarrow \Delta T = \frac{J^2 d^2 \rho}{k} \tag{3.5}$$

Where k is the thermal conductivity of Platinum. This means that the temperature difference between the device is not dependent either on the length or width of the track and only depends on the thickness of the conducting layer.

For the parameters of Table 3.1, $\Delta T = 35.6°C$. Thus, if the substrate is kept at room temperature, 300 K, the device temperature will be ~336 K. The finite temperature simulations show the robust operation of the device with this temperature.

Table 3.1.The parameters used for the calculation of equilibrium temperature.

Parameter	Value
Electrical resistivity of Cobalt	$5.6 \times 10^{-8}\ \Omega \cdot \mathrm{m}$
Electrical resistivity of Platinum	$9.8 \times 10^{-8}\ \Omega \cdot \mathrm{m}$
Thermal conductance of platinum	$71.6\ \mathrm{W \cdot m^{-1} \cdot K^{-1}}$
Thickness of the Cobalt layer	4nm
Thickness of platinum	4nm
Current density if the current passes a 100nm wide channel	$2.9 \times 10^{12}\ \mathrm{A \cdot m^{-2}}$

3.9 Summary

The skyrmion generator is the subject of this chapter. First, the selective domain wall pinning, and the domain expansion based on it have been described. Then the geometry of the device and the process of skyrmion generation based on this geometry were explained. The sequential steps leading to skyrmion generation were explained and the steps for the periodic generation of skyrmions were delineated from the other steps. The fact that this geometry is subjected to changes without hindering the device operation was emphasized. Since the device has periodic skyrmion generation, the frequency of the skyrmion generation and the effect of the deciding factor i.e., current density value was quantized. It was determined that the skyrmion generation frequency increases by increasing the current density. Since the damping parameter has an important effect on the generation of skyrmions, the effect of the damping and current density together was quantified and presented in a phase diagram. The energy required for skyrmion generation also was discussed.

The skyrmion frequencies produced by the device can be controlled reversibly within a wide range of frequencies from 114 MHz to 21 GHz, depending on the geometry, applied current, and material properties such as damping, DMI parameter, and anisotropy constants. The presented initialization and frequency tuning procedures allow for precise and dynamic adjustment of the skyrmion frequencies. As the device does not require an external magnetic field and is robust against variations in cobalt layer thickness. Additionally, since the nucleation energy for each skyrmion is around 50 k_BT, the marginal energy consumption per bit is much lower than that of the existing technology and very close to the Landauer limit.

The device proposed can serve as an efficient and nonvolatile clock or signal source for integrated skyrmionic chips. Due to the linear frequency response of the device over a large range, it can also be used as a skyrmionic frequency modulator in telecommunication.

Chapter 4

THE INVERTER GATE

4.1 Introduction

With the introduction of the DC current skyrmion generator in the last chapter, we can now turn our focus on the INVERTER gate as the central element of the skyrmionic logic scheme.

The importance of an inverter gate is evident since inversion is one of the essential elements in the universal set of operations in Boolean Logic.

A useable and robust skyrmionic logic gate system must use a single type of signal, have cascadable geometry, use the non-volatility of skyrmions for nonvolatile functionality and not depend on the synchronized motion of skyrmion.

The signal in this gate is the skyrmion. If a skyrmion exists on a region of interest at the specified time window, the signal value is '1'; if it doesn't exist, the signal value is '0'.

There have been many efforts to make a skyrmionic logic gate system. Many of these systems are universal but use different stimuli for the data-carrying signals. Some proposals use the voltage-induced change in the perpendicular magnetic anisotropy energy density. Other studies use the current induced domain wall injection. Other efforts lack the inversion functionality and thus don't lead to a universal set of logic gates. For more information on these studies, you can refer to the section 1.2.7 of this thesis.

4.2 Gate Geometry

The inverter gate introduced in this chapter is 300 nm wide and has a length of 240 nm. The skyrmion track widths are 50 nm. Figure 4.1 shows the geometry of the inverter gate with the skyrmion's injection sites and their direction of motion. The proposed gate is from cobalt as the ferromagnetic layer on top of the platinum as the heavy metal layer with the large spin-orbit coupling that induces the interfacial DMI needed for the skyrmion stabilization.

As Figure 4.1 suggests, there are two entrance locations for the skyrmions. The left side of the horizontal channel and the bottom of the vertical channel are the entrance points of skyrmions. We call the skyrmion that enters the vertical channel the "signal skyrmion" and the skyrmion that enters the horizontal channel the "probing skyrmion".

The vertical channel starts with a 50 nm wide track connected to a 20 nm track via acute 45° angle edges. The dipolar fields of these sharp angle edges reduce the entrance threshold current of skyrmion into the 20nm track. There is also an 8 nm notch in the vertical track. As we saw in the last chapter, the role of this notch is to introduce a difference in the passing currents of the domain walls (DWs) to make the domain extension possible. The notch helps break the inversion symmetry of the device geometry and this asymmetry allows for breaking the topological protection of skyrmions. There are also two protruding notches on the sides of the vertical channel that create potential barriers to increasing the stability of the vertical channel domain.

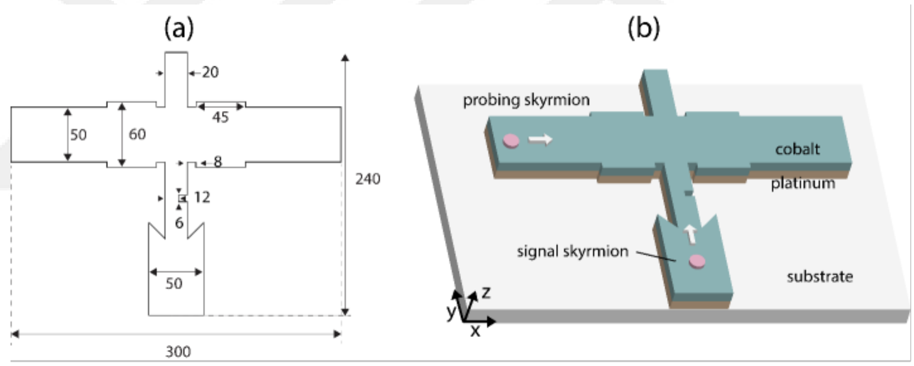

Figure 4.1. The inverter gate material and geometry. (a) the detailed top-view geometry of the inverter gate (b) the layers of the inverter gate with the injected skyrmions[91].

4.3 Work Cycle

The work cycle of the inverter gate consists of three main stages: **Initialization**, **Transmission**, and **Clearance**. These stages are sequential, i.e., the application of spin-polarized current to the horizontal and vertical channels of the device is asynchronous. At the initialization stage, the current pushes up the skyrmion in the vertical track. Then, at the transmission stage, the horizontal skyrmion is pushed. In the end, the device is cleared up of any remaining domain walls and skyrmions. Since the vertical channel skyrmion is the signal skyrmion, the existence of a skyrmion at the beginning of the operation at the vertical channels means the 'input = 1', and the lack of skyrmion means the 'input 0'. The probing skyrmion is refreshed at each T ns at the beginning of each work cycle, where T is the operation period of the inverter gate. The output port of the vertical channel could also be used for probing the previous state (or presence of domain wall: 1, else: 0) of the non-volatile logic inverter gate.

Figure 4.2 shows the operation cycle of the inverter gate. Both cases of 'input = 1' and 'input = 0' are shown in the upper and lower parts of the figure, respectively. Supplementary movie S4.1 (Supplementary_Video_SV_1._0_1 in [91]) shows the case for the 0→1 and supplementary movie s4.2 (Supplementary_Video_SV_2._1_0 in [91]) shows the case for 1→0 case.

4.3.1 Initialization

The first column of Figure 4.2 part (a), depicts the initialization stage of the inverter gate operation. Since the magnetic configurations moved by current move in the direction of the movement of electrons, a DC current is applied to the -y direction to move the skyrmion in the +y direction. The value of this current is between 0.9 $\times 10^{12}$ and 1.9 $\times 10^{12}$ A m^{-2}. This current value is such that it is strong enough to break the topological protection of the skyrmion but not as strong as clearing the vertical channel from the magnetic domain. This current is applied for 0.46 ns. The figure shows the evolution of the magnetic configuration of the vertical channel at this stage. Different phenomena are happening at this stage, such as the selective domain wall pinning and changing the single bent DW into three DWs at the junction. We will go through these phenomena later in this chapter.

If there is no skyrmion in the vertical channel at the beginning of the stage, the vertical channel will stay empty throughout the operation. The first column in Figure 4.2 part (b), shows this situation.

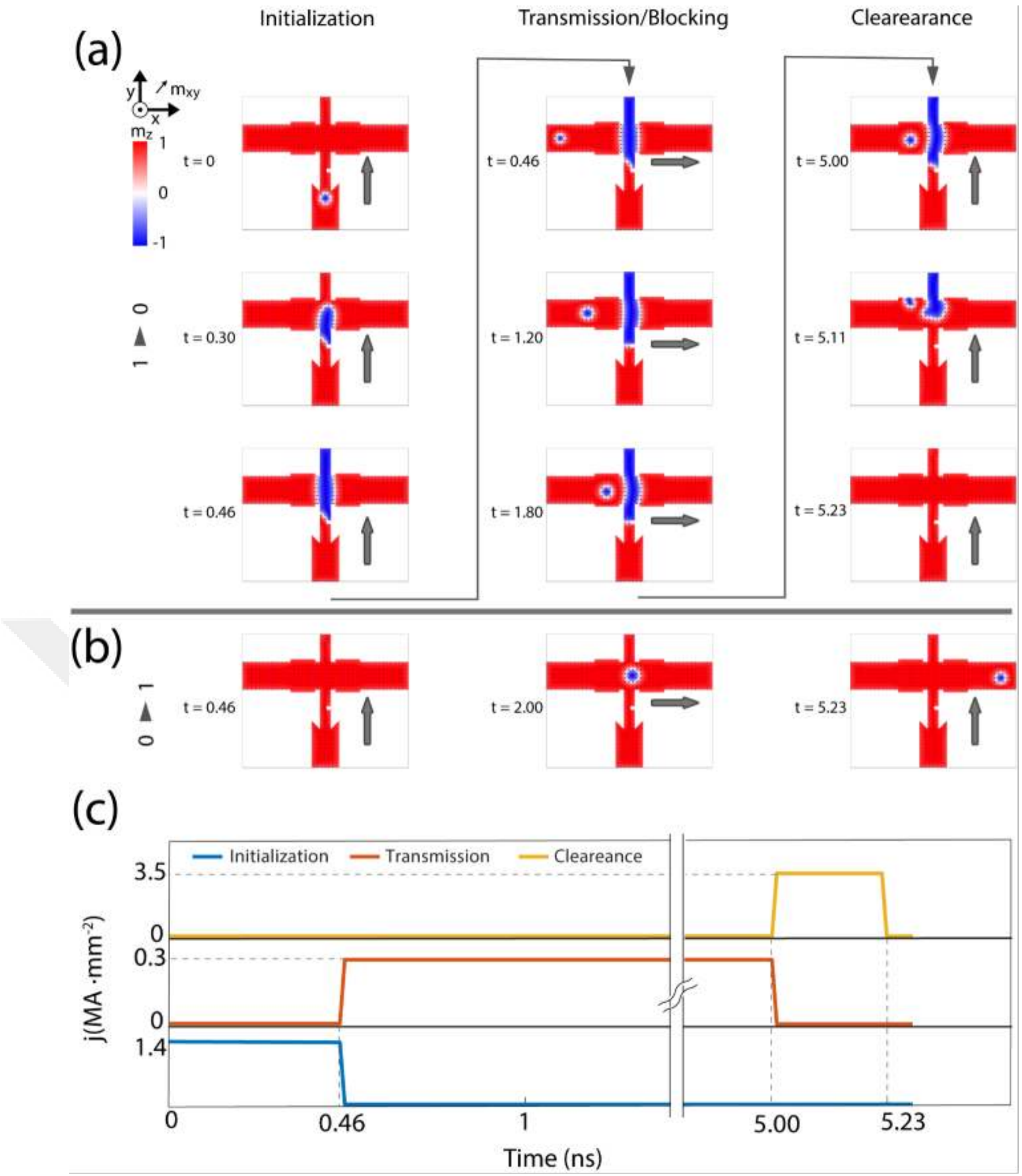

Figure 4.2. The work cycle of the gate. (a) The 'input = 1' (b) the 'input =0' case. (c) The applied spin-polarized current densities [91].

4.3.2 Transmission and Blocking

The second column of Figure 4.2 shows this stage. This stage starts from t=0.46 ns. Depending on the input of the initialization stage, the vertical channel might be filled or empty. The spin polarized current is applied to the horizontal direction to push the skyrmion to the right side of the horizontal track. If the vertical channel is empty at this stage, the skyrmion moves to the right side of the horizontal track, but if the vertical channel is filled, this domain stops the skyrmion from moving to the right side of the device. In short, based on the existence of the magnetic domain in the vertical channel, the skyrmion is either transmitted to the right side or blocked by the magnetic domain. The duration of this stage is 5.23 ns. This time equals the time it takes the skyrmion to move from left to right side of the device.

This stage is the device's main logic stage, as the magnetic domain in the vertical channel depends on the initial skyrmion in the vertical channel input. Since the domain blocks the motion of the horizontal skyrmion from left to right, depending on the existence/lack of the signal skyrmion, there will be/not be a skyrmion at the right-hand side of the horizontal track at the end of the operation; hence the name of the device: the INVERTER.

One question that might arise at this stage is, "why do we need to apply the current to the skyrmion for the whole duration of the transmission case even if the magnetic domain is blocking the skyrmion from moving?" The answer is that the work cycle of the device must be independent of its inputs for the operation to be meaningful. In other words, if there were sensors or other devices that let us know if the vertical channel is filled, we wouldn't need the probing skyrmion to check the existence of the vertical domain. One can say that the probing skyrmion is a "sensor" to check the presence of the vertical domain. Thus, we must apply the current for the complete duration of the skyrmion movement from left to right.

4.3.3 Clearance

At this stage, the magnetic configuration of the device must be reset for the next work cycle to begin. A high enough current (3.5×10^{12} A m^{-2}) is applied to the vertical track of the device and the side protruding notches of the horizontal track. This current clears up the device of the remaining magnetic domains. By the same justification of the last subsection, we apply the current whether any magnetic domains exist in the geometry as the work cycle is oblivious to the existence of signal skyrmion.

4.4 Operational Characteristics

In this section, we have a detailed look at the operational characteristics of the inverter gate. The external driving stimuli to this device are the applied currents in the vertical track, the horizontal track, the side notches, and the applied magnetic field. We also discuss the critical current density values, timings, and the robustness of the device.

Figure 4.3 summarizes the main points of this section's discussion. The first row of this figure is devoted to the timing of initialization and transmission stages on the applied current. The second row explains the timing dependence of the clearance stage on the applied current and external magnetic flux density.

4.4.1 Initialization Stage

Figure 4.3(a) depicts the dependence of the minimum time for the initialization stage versus the applied current. At this stage, the current pushes the skyrmion at the bottom of the vertical channel to the narrower channel. This breaks the topological protection of the skyrmion, turning it into a pair of domain walls with a magnetic domain whose magnetization points towards the -z direction. We call the upper domain wall the "leading domain wall" and the lower domain wall the "back domain wall." The passing currents for these two domain walls from the intruding notch in the vertical channel are different. The current density needs to be higher than the threshold to push the skyrmion into the narrower channel and higher than the threshold for pushing the leading domain wall past the intruding notch. The higher value of these two is the current density value needed to move the leading domain wall past the notch. This current density is 1.3×10^{12} A m^{-2}.

On the other hand, the current density must not be higher than the current density for passing the back domain wall from the central notch, i.e., 1.96×10^{12} A m^{-2}. Since Figure 4.3(a) shows the minimum filling time of the vertical channel, for example, for $J=1.4 \times 10^{12}$ A m^{-2}, the minimum time is 0.44 ns. We have picked 0.46 ns which is marginally higher than the minimum, to ensure that the channel is filled with a safe margin.

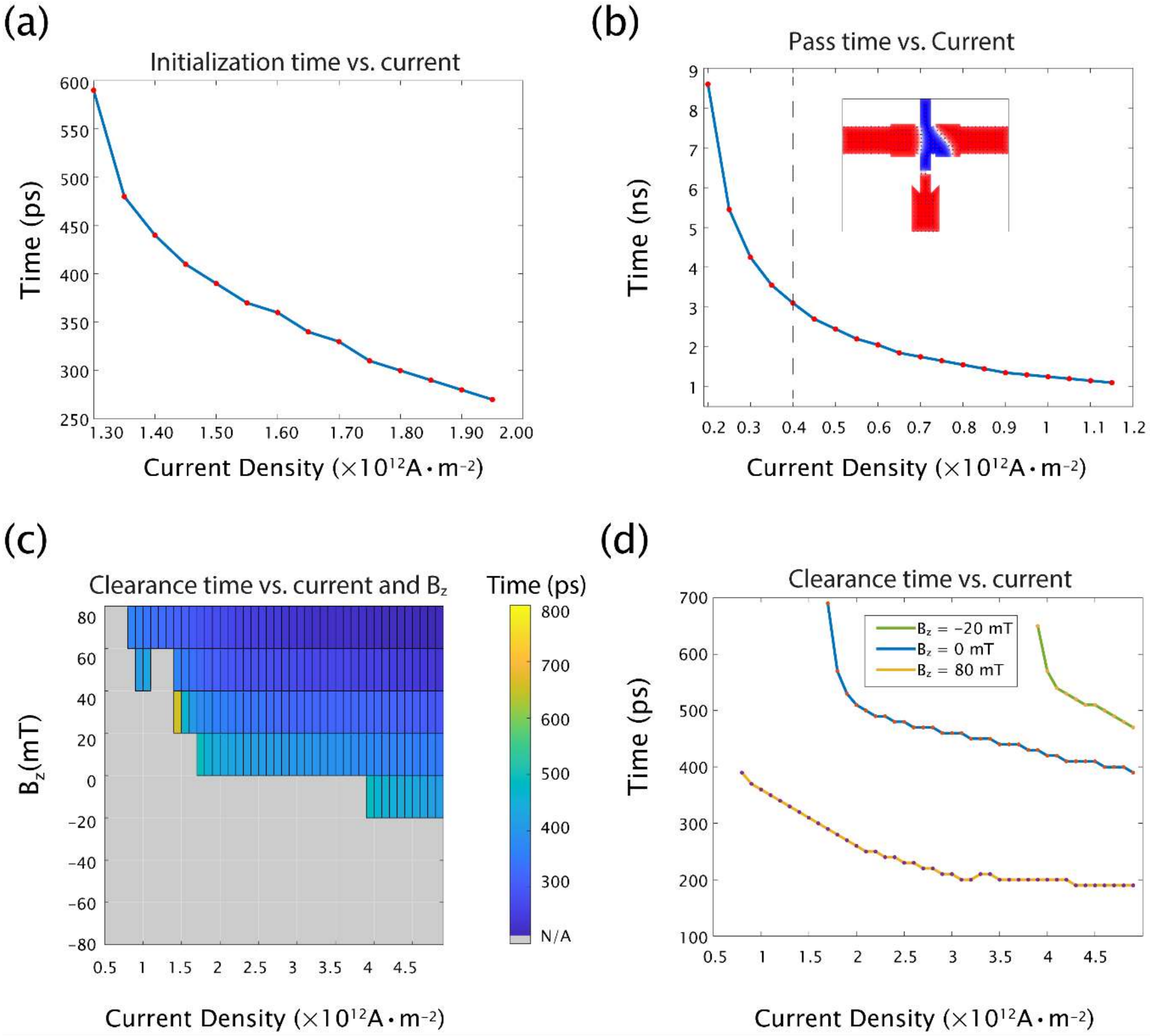

Figure 4.3. Operational characteristics dependence on the current and magnetic field. (a) The duration of the Initialization stage vs. current density (b) The duration of Transfer stage vs. current density (c) the effect of the current density and external field on the duration of the Clearance stage. Larger current values and higher external fields decrease the timing of the Clearance stage. (d) Cross sections of the part (c) for different external field values. For a constant external field, increasing the current density decreases the Clearance time. Higher external fields lower the current density threshold for the clearance stage [91].

4.4.2 Transmission/Block Stage

Figure 4.3 part (b) shows the skyrmion transmission time versus the current density. This is the time that takes the skyrmion from the left side of to reach the right side. Most of the operation time cycle of the gate passes in this stage, and it seems desirable to increase the current density of this stage to the highest possible value for a higher operating frequency of the device. This highest current has two critical thresholds. First, a high enough current can disrupt the vertical domain. As the inset of Figure 4.3 part (b) shows, increasing the current density beyond 0.4×10^{12} A m^{-2} disrupts the vertical domain. Although this disruption does not hurt the transmission operation, it hinders the clearance operation and must be avoided. Therefore, we must keep the current density value below this threshold. As we will see in the more detailed geometry analysis, this threshold can be increased by increasing the heights of the side notches. Still, we are using the values for the geometry we introduced at the beginning of this chapter.

Another threshold for the current is the skyrmion edge edge-annihilation threshold. If the skyrmion reaches the right end of the horizontal track, the currents higher than 0.6×10^{12} A m^{-2} destroy the skyrmion. For the scalable operation of the device, we need to preserve the skyrmion and keep the current value below this value. For the existing geometry of the device, the domain disruption current density value is lower than the skyrmion annihilation current value. Thus, by keeping the current density below the domain disruption threshold current, we automatically keep the skyrmion intact when it reaches the right end of the horizontal track. We have chosen 0.3×10^{12} A m^{-2} and push the skyrmion for 5.23 ns which is slightly higher than the time needed to move the skyrmion to the right-hand side.

4.4.3 Clearance Stage

Figure 4.3 parts c and d show the time dependence of the clearance stage on the applied external field and current density. According to part (c), there is a window of parameters for the correct operation of the clearance stage. A magnetic field towards -z direction hinders the clearance, and a magnetic field towards +z helps a faster clearance. This is intuitively understandable since applying the magnetic field in the +z direction helps reduce the area of the regions with -z magnetization (blue regions). We also see that using the higher current leads to a faster device clearance. The dependence of the clearance time on the current density and magnetic field helps us choose the best values for the current density. Part (d) shows the current dependence of the clearance stage time for different magnetic field flux density values. We have chosen the B=60 mT and J= 1.4×10^{12} A m^{-2}. With these values, the clearance time is 0.23 ns.

4.5 Energy Analysis

The energy consumption of the inverter gate is an essential criterion for efficiency evaluation. The external sources for the energy of the inverter gate are the spin polarized current and the applied magnetic field. Here the applied magnetic field is a DC field. Thus, this chapter concerns itself with the consumption and injection from the spin polarized current. The energy of this current has two separate parts.

1- The spin injection energy leads to dynamic changes in magnetization configuration, e.g., the motion of skyrmions, the elongation of the domains, the bending of the domain walls, etc.

2- Ohmic dissipation energy turns into heat. This heat increases the temperature, which introduces noise to the device.

Therefore, we are dealing with two different energies that contribute to opposing phenomena. Here we calculate the energy consumption of both parts and understand the energy scale and requirements for robust operation. Figure 4.4 shows the energy analysis results of the device for the "input =1" case as this has the higher energy consumption.

4.5.1 Magnetic Energy

Figure 4.4 parts (a) and (b) show the snapshots of the magnetic configuration evolution of the inverter gate and its magnetic energy (blue curve in part b). The magnetic energy evolution comes from the spin transfer torque of the conduction electrons. The snapshot number on the energy curve is put to better understand the correspondence between the blue curve of part (b) and the snapshots.

To calculate this energy, we must note that the energy is transferred from the electrons to the magnetic configuration in a non-adiabatic way, i.e., the reduction in the energy of the magnetic structure is not transferred back to the spin polarized current. Therefore, we only integrate the magnetic energy of the device where the energy is increasing. For this, we can calculate the injected power to the device and integrate the energy where the power value is positive ($P(t) > 0$).

By "magnetic energy," we mean all energy terms that are related to the magnetization configuration:

$$\Phi(\mathrm{t}) = \Phi_{\mathrm{ex}}(t) + \Phi_{\mathrm{DMI}}(t) + \Phi_{\mathrm{demag}}(t) + \Phi_{\mathrm{anis}}(t) + \Phi_{\mathrm{zeeman}}(t) \quad (4.1)$$

The total magnetic energy for the system for a 1nm thick layer is 9×10^{-19} J, and for a 6nm thick layer is 5.2×10^{-19} J $\approx 6\times E_{1nm}$. To have a better scale, we can compare these energies to the k_BT at room temperature (300 K). The energy for 1nm and 6nm thick layers are 230 k_BT and 1347 k_BT at T=300 K for 1 nm and 6 nm, respectively.

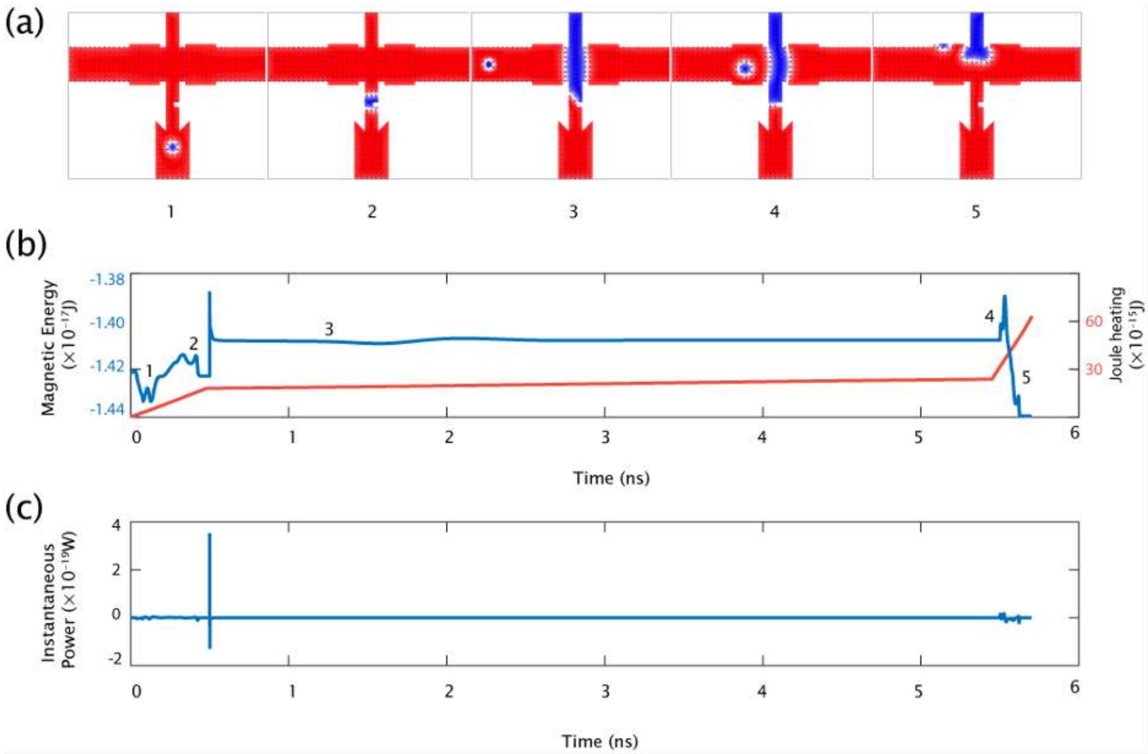

Figure 4.4. The energy and power analysis of the inverter gate. (a) The magnetic configuration of the device at key moments specified in part b (b) blue: The total magnetic energy evolution of the device. steps 1 and 3 denote the moments that a skyrmion is introduced to the system. Step 2 shows the DW passing the vertical channel notch, and step 4 shows the increase in the energy due to the repelling force between a skyrmion and a DW. Step 5 is the clearance stage of the device. Red: The Joule heating energy of the device. (c) The instantaneous power of the magnetic energy of the device. Integration of the parts with positive power ($P_{input} > 0$) shows the marginal energy consumption of the device [91].

Figure 4.4 shows the energy development of the system for the case of 1 → 0 i.e., when a skyrmion is present in the vertical channel. The energy of the system can also be investigated for the case where there is not a skyrmion in the vertical channel i.e., the case of 0 → 1. Figure 4.5 shows this case. Since the Joule heating energy is the same for both cases, it is not repeated in this figure.

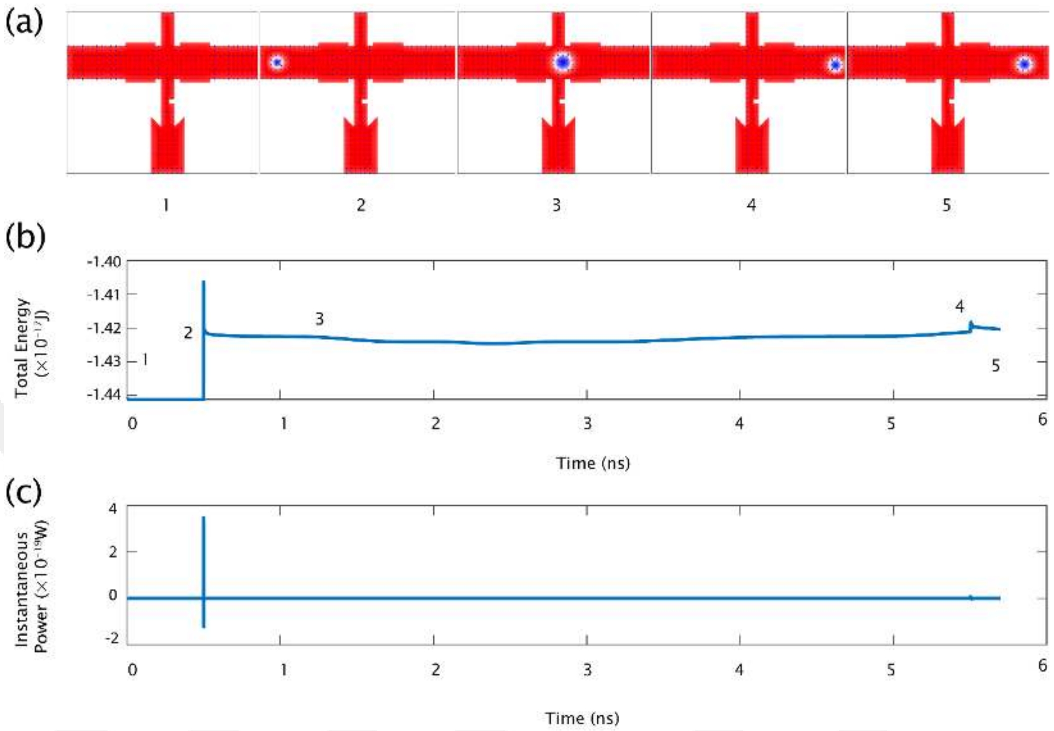

Figure 4.5.The energy and power analysis of the inverter gate for 0→1 case. (a) The magnetic configuration of the device at key moments specified in part b (b) The total magnetic energy evolution of the device. The constant period of the initialization stage shows the lack of skyrmion in the vertical channel (step 1). Introducing a skyrmion to the horizontal track increases the energy (step 2). The energy remains relatively constant with small changes of the different energy landscape the skyrmion experiences in the horizontal track (step3). The repulsion between the skyrmion and the right wall of the horizontal track slightly increases the energy (step 4). Turning off the current leads to the further decrease in the energy because of the relaxation of skyrmion (step 5). The numbers correspond to the snapshots in the part (a). (c) The instantaneous power of the magnetic energy of the device. Integration of the parts with positive power ($P_{input} > 0$) shows the marginal energy consumption of the device [91].

4.5.2 Joule Heating Energy

Since the flow of electric current is the physical drive of the device, the energy consumption due to the Joule heating is an integral part of the energy calculation.

We first calculate the energy consumption due to the electric current flow in the device and then calculate its thermal effects. The input power in each track is calculated by using:

$$P_{in} = I^2 \times R_{eq} \tag{4.2}$$

Where I is the current flowing in the track, and $R_{eq}$is the equivalent resistance given by:

$$R_{eq} = \sum_r \rho.\frac{l_r}{W_r d} \tag{4.3}$$

Where ρ is the resistivity of the material, l_r is the length of the track, W_r is the width of the track, and d is the thickness of the gate. The total energy of each stage is calculated by using:

$$E = P_{in} \times \Delta t \tag{4.4}$$

Where Δt is the total time of the stage. Table 4.1 shows this energy for different stages of a 1 nm thick inverter gate.

Table 4.1. Ohmic dissipation energies for the inverter gate

Stage	Energy per 1nm thickness
(1) Initialization	1.89×10^{-14} J
(2) Transmission	5.61×10^{-15} J
(3) Clearance	3.89×10^{-14} J

4.6 Cascadability

This section goes through the cascadable operation of the device. Here we show that a cascaded two-gate structure is feasible. Then the stage for the complete Boolean logic picture of the next chapter is set.

Figure 4.6 shows the cascadable inverter gates. Part (a) shows the geometry of these gates, and part b shows the energy analysis of the cascaded gates, like the inverter gate energy analysis.

In the configuration of Figure 4.5, the output of the bottom inverter gate is connected to the signal input of the top inverter gate. We define the order of

operation, such as the bottom inverter gate being the first and the top inverter gate being the second to run. This order of operation is essential and defines the system's functionality of connected gates. Here we have the case where the input of the first gate is ‘0’. Thus, its output is ‘1’. The operational cycle of the inverter gate in the cascaded fashion is not different from its operation in the singular form. At the end of the operational cycle of the first gate, a skyrmion exists at the lower end of the vertical channel of the second gate. Now, the operation cycle of the second gate begins. Since the input of the second inverter gate is ‘1’ at this point, the output of it will be ‘0’. This shows that connecting two inverter operations equals the trivial case of just transferring the input.
Here, we have just considered the operation of the INVERTER gates with a signal skyrmion and a probing skyrmion such that the probing skyrmion always exists and the domain from the signal skyrmion blocks the movement of the probing skyrmions.

Supplementary movie S4.3 (Supplementary_Video_SV_3._0_1_0 in [91]) shows the case for the 0→1→0 and supplementary movie S4.4 (Supplementary_Video_SV_4.1_0_1 in [91]) shows the case for 1→0→1 case.

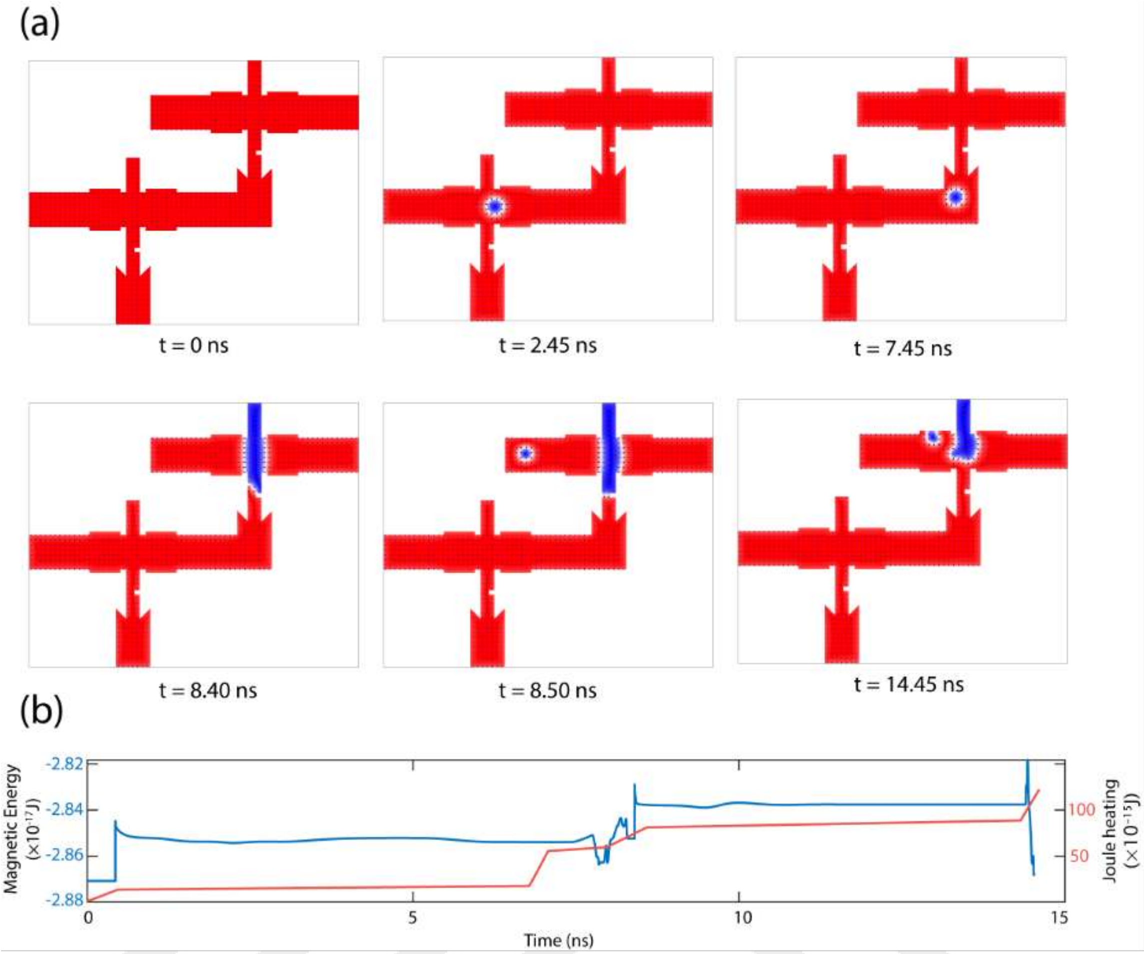

Figure 4.6. Cascadable inverter gates. (a) The magnetic configuration of the cascaded Inverters for 0→1→0 (b) the magnetic and Joule heating energy of the cascaded gates [91].

Figure 4.6 Shows the energy development of the system for the case of 0 → 1 →0 i.e., when a skyrmion is not present in the vertical channel of the bottom inverter gate. The energy of the system can also be investigated for the case where there exists a skyrmion in the vertical channel of the bottom gate i.e., the case of 1 → 0 →1. Figure 4.7 shows this case. Since the Joule heating energy is the same for both cases, it is not repeated in this figure.

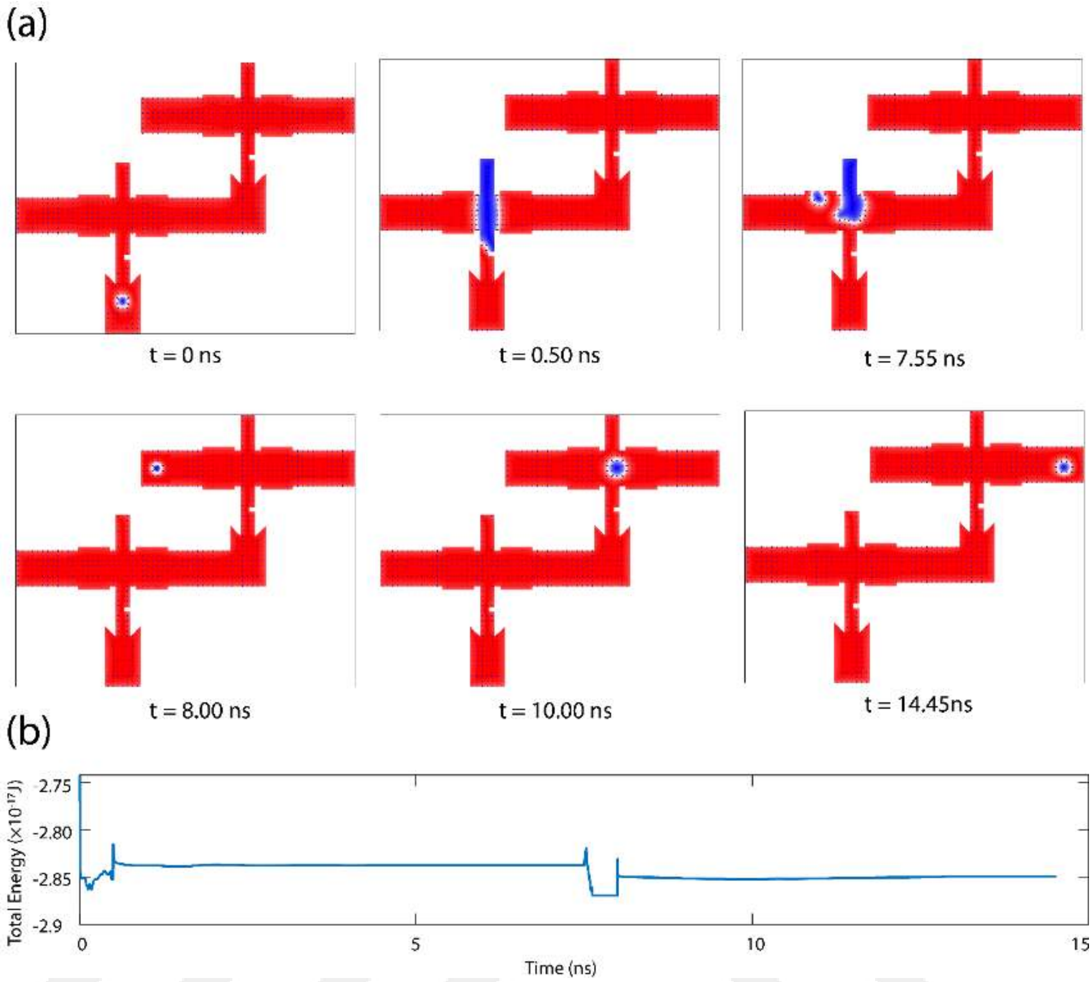

Figure 4.7. Cascadable inverter gates. (a) The magnetic configuration of the cascaded Inverters for 1→0→1 (b) the magnetic energy of the cascaded gates [91].

4.6.2 A Change in the Perspective: AND Gate

If we change our notion of the probing skyrmion of the second (top) gate of Figure 4.5 to another signal input, we reach an exciting result for the cascaded system of the gates. In this case, our gate system has two inputs. Input1 is the skyrmion in the vertical channel of the bottom gate, and input2 is the skyrmion in the horizontal track of the top gate. Now let's consider the four different possible cases:

- Input1=0, input2=0/1: In this case, the skyrmion in the horizontal channel of the first inverter reaches the second inverter. It also fills up the vertical channel of the second inverter. In this case, at the end of the operation cycle of the second inverter, there will be no skyrmions at the output of the cascaded gate system.

- Input1=1, input2=0/1: In this case, since input1 blocks the probing skyrmion of the first inverter gate, there will be no skyrmion blocking the horizontal channel of the second inverter gate. Thus, if there is a skyrmion at the left of the horizontal track of the second inverter gate, it will move to the output location, and the output will be 1.

Table 4.2 summarize these cases.

Table 4.2.The cascaded gates with two inputs

Input1	**Input2**	**output**
0	0	0
0	1	0
1	0	0
1	1	1

This table shows the truth table of an AND gate. Since the intention of designing the inverter gate was to have the NOT gate functionality, and we achieved this result by changing the probing skyrmion of the top inverter gate to a signal skyrmion, we will not go into more detail for now. The discussion of the complete logic system will follow in the next chapter.

4.7 Physical Interactions of Magnetic Textures and External Forces

As we have seen, there is a rich set of interactions for the magnetic configurations, such as skyrmions and DWs. Two main interactions are the movement of objects by the spin-polarized current and interactions between two magnetic textures or between a magnetic texture and geometry.

These two types of interactions lead to different phenomena, such as selective domain wall pinning and magnetic domain elongation, domain wall curvature induction, domain wall break and transformation, domain wall repulsion, and skyrmion repulsion.

4.7.1 Domain Wall Motion by Spin-polarized Current

Here we understand the domain wall motion by reducing the domain walls to a 1D structure. If we cut the domain walls of Figure 4.8 part (b.i) along the vertical line and depict both domain walls in the yz plane, we reach the parts (a.i) and (a.ii), respectively, for the leading and back domain walls. We want to see how the spin transfer torque moves both domain walls in the $+y$ direction.

To understand this torque, we need to use the Zhang-Li torque term of equation (2.109):

$$(1+\alpha^2)\dot{\boldsymbol{m}}_{ZL} = [(1+\xi\alpha)\boldsymbol{m}\times(\boldsymbol{m}\times(\boldsymbol{u}.\nabla)\boldsymbol{m}) + (\xi-\alpha)\boldsymbol{m}\times(\boldsymbol{u}.\nabla)\boldsymbol{m}] \tag{4.5}$$

For a current that's only flowing in the y direction, and if $\xi = \alpha$, this equation reduces to:

$$\dot{\boldsymbol{m}}_{ZL} = \frac{\mu_B j}{2e\gamma_0 M_{sat}} \mathbf{m}\times\left(\mathbf{m}\times\frac{\partial}{\partial \mathrm{y}}\mathbf{m}\right) \tag{4.6}$$

This means that the change of magnetization is normal to the magnetization itself. Since we are talking about the one-dimensional domain wall here, i.e., we are regarding the changes in the yz plane to represent all changes in the magnetization:

$$\boldsymbol{m}\cdot\frac{\partial}{\partial \mathrm{y}}\boldsymbol{m} = 0 \tag{4.7}$$

Using the vector identity:

$$A\times(B\times C) = B(C\cdot A) - C(A\cdot B)$$

we have

$$\dot{\boldsymbol{m}}_{ZL} = -\frac{\mu_B j}{2e\gamma_0 M_{sat}}\frac{\partial}{\partial \mathrm{y}}\boldsymbol{m} \tag{4.8}$$

This equation has a simple solution:

$$\boldsymbol{m}(y,t) = \boldsymbol{m}(y-vt) \tag{4.9}$$

where:

$$v = \frac{\mu_B j}{2e\gamma_0 M_{sat}} \tag{4.10}$$

We deduce the following from equation (4.8):

- The current injected movement keeps the body rigid and doesn't change the magnetization profile of the domain wall.
- The speed of the movement is directly proportional to the current density and inversely proportional to the saturation magnetization.

Green arrows show numerical results of STT on the domain walls magnetization profile on each magnetization site. These arrows indicate that both the domain walls move in the $+y$ direction.

Since the STT results in the motion of the magnetic objects, we can talk about a generalized force on the magnetic texture. Figure 4.8 part b shows this STT-induced force by green arrows.

4.7.2 The Energy Induced Forces

The STT term in equation (4.6) is a dissipative term. i.e., it matches the dissipative (damping) part of the LLG equation. If we rewrite the LLG equation (2.75) with (4.6), we have:

$$(1+\alpha^2)\dot{\boldsymbol{m}} = -\gamma \boldsymbol{m} \times \boldsymbol{H_{eff}} + \boldsymbol{m} \times \left(\boldsymbol{m} \times \left[-\alpha\gamma \boldsymbol{H_{eff}} + v(1+\xi\alpha)\frac{\partial}{\partial e_j}\boldsymbol{m}\right]\right) \tag{4.11}$$

Where e_j is the direction of electron movement. Thus, the motion of textures in the system depends on the balance of the effective field and the STT.

We know from equation (2.103) that the H arises from the magnetic energy of the system, i.e.,

$$\boldsymbol{H_{eff}} = -\frac{1}{\mu_0 M_s}\frac{\delta\Phi}{\delta\boldsymbol{m}}$$

This effective field shows itself as a counteracting force to the STT force. Part (b) shows these forces by black arrows.

Therefore, the STT force can induce energy changes in the system. Because of the adiabaticity of the magnetic energy, magnetic texture changes that increase energy are elastic. This elasticity means that the magnetic textures have spring-like interactions. An STT force or an external magnetic field can push domain walls together, contract a skyrmion, push a skyrmion closer to a domain wall, bend a domain wall, etc. Now, if we remove external stimuli, the effective field from the increase in the geometry transfers the system to the lower energy level.

Moreover, the effective field arising from the system's energy can change the magnetic configuration of the magnetic texture. This change can, in turn, change the derivative of the magnetization in the direction of the spin-polarized current, which can change the contribution of the STT to the system.

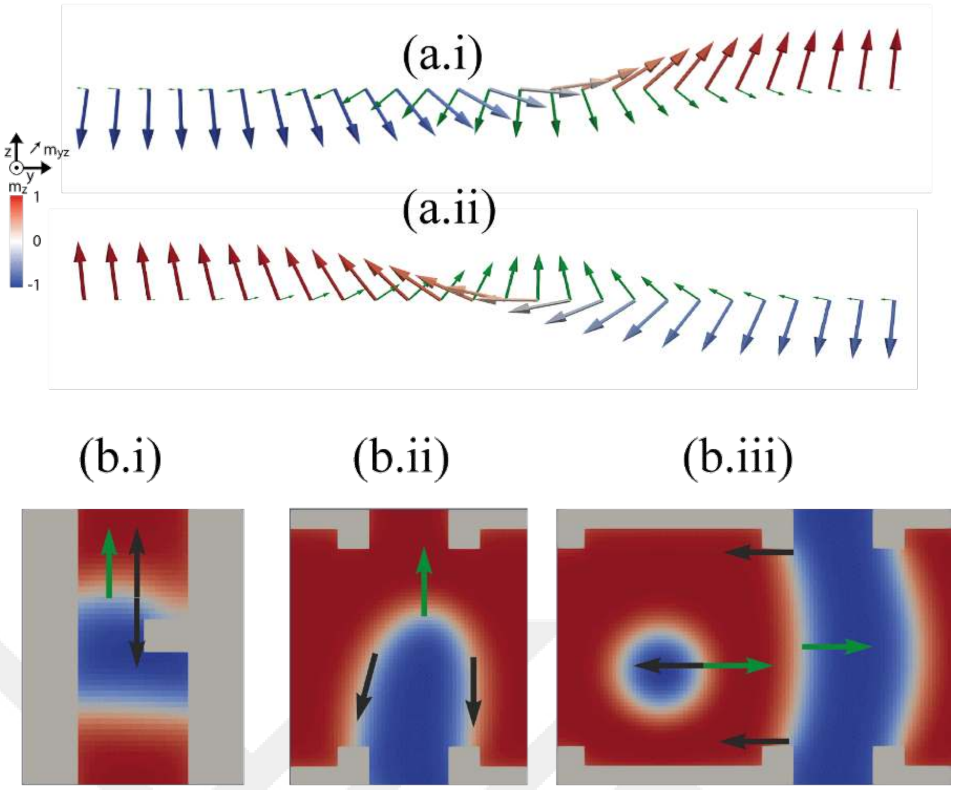

Figure 4.8. Domain wall with generalized forces. (a.i) The cross-section of the leading domain wall and the current induced torques exerted on each site. The green arrows show the current induced torques (a.ii) The cross-section and torques of the back DW (b.i-iii) Magnetic configuration and the generalized forces acting on magnetic structures at key times. The black arrows show the forces exerted on magnetic textures by either geometry or magnetic textures and the green arrows show the current induces torques [91].

4.8 Energy-dependent Properties of Magnetic Textures

Now that the existence of forces on magnetic objects are justified, we can discuss the implications of these forces in greater detail.

4.8.1 Domain Wall and Skyrmion Repulsion

This work deals with 180° domain walls connecting the regions with opposite magnetic directions. The thickness of the domain wall depends on the balance between the exchange energy and dipolar energy. When two domain walls get very close, two areas with the same magnetization direction become closer. This increases the dipolar energy of the system. Moreover, if these two domain walls get much closer to each other such that the distance between them is closer than the exchange length of the system, the exchange energy increases. Both increases in energy result in an effective field that pushes the domain walls away from each other. Since dipolar and exchange energies are reciprocal, both domain walls get repelled. This interaction is also valid between two skyrmions and between a skyrmion and a domain wall.

4.8.2 Skyrmion-edge Repulsion

Both domain walls and skyrmion contribute to an increase and a reduction in the system's energy. The increase comes from the exchange interaction between the adjacent spins, and the reduction results from the lower dipolar energy since they form regions with opposite magnetizations. For stable textures, the energy reduction is greater and results in negative net energy. When a skyrmion moves closer to an edge, the dipolar energy increases because of the opposite direction of its stray fields to the stray field of other magnetization sites. This increase in energy results in a repulsion force. If it reaches the exchange length, the exchange energy increases too.

4.8.3 Domain Wall Self-energy

The DWs depicted in Figure 4.8 parts (a.i) and (a.ii), are the 1D cross sections of the DWs of the part (b.i). For these DWs, we call the extent of the DW in the y direction the "thickness" of the DW and the extent of the DW in the x direction the "length" of the DW. For the straight DWs without a change in the cross-sectional profile, the energy of the DW increases for longer domain walls. This means that a shorter DW is preferred over a longer one.

The exchange energy wants to keep the adjacent magnetizations in the same direction. Any added angle for the adjacent magnetizations increases the exchange energy. This means that a straight domain wall has lower energy than a domain wall with curvature.

4.8.4 Skyrmion self-energy

A skyrmion has a natural diameter and wall thickness. These values depend on the material parameters [143]. Its characteristic sizes might change when we put a skyrmion under external stimuli such as a magnetic field, edge, or domain wall repulsion. These changes result in a difference in the energy of the skyrmion and the emergence of a new effective field. For example, if a skyrmion is put inside a smaller channel, the edge forces constrict the skyrmion. This results in an increase in the energy of the skyrmion, and new effective fields emerge as a result. Then if the edges are removed, this effective field increases the skyrmion size to reduce its energy.

4.9 Device-specific Interactions

To have a detailed understanding of the magnetic texture development of the device an analysis and break down of different phenomena happening is necessary. Figure 4.9 shows the total magnetic energy versus the texture development of the various parts of the device. The figure legend on the bottom right shows the region of interest for other parts.

4.9.1 Selective Domain Wall Pinning

When the skyrmion is pushed into the narrower part of the vertical channel, its topological protection is broken, and the skyrmion turns into two domain walls. The spin polarized current pushes both walls with the same force in the +y direction. When the leading wall reaches the notch, it is broken easily and occupies the left-hand side of the notch. On the other hand, passing the notch is harder because it increases the wall length and, thus, the energy. This increase in energy shows itself as a force keeping the wall from passing the notch. Now since the STT force is pushing the back domain wall too, the back wall gets closer to the leading wall. This leads to an increase in energy. This increase in energy shows itself as the effective field repulsive force on the leading domain wall. The addition of the STT and effective field forces is enough to push the domain wall past the notch. When the back domain wall reaches the notch, it cannot pass the notch because there is only STT acting on it which is not enough to push this wall past the notch.

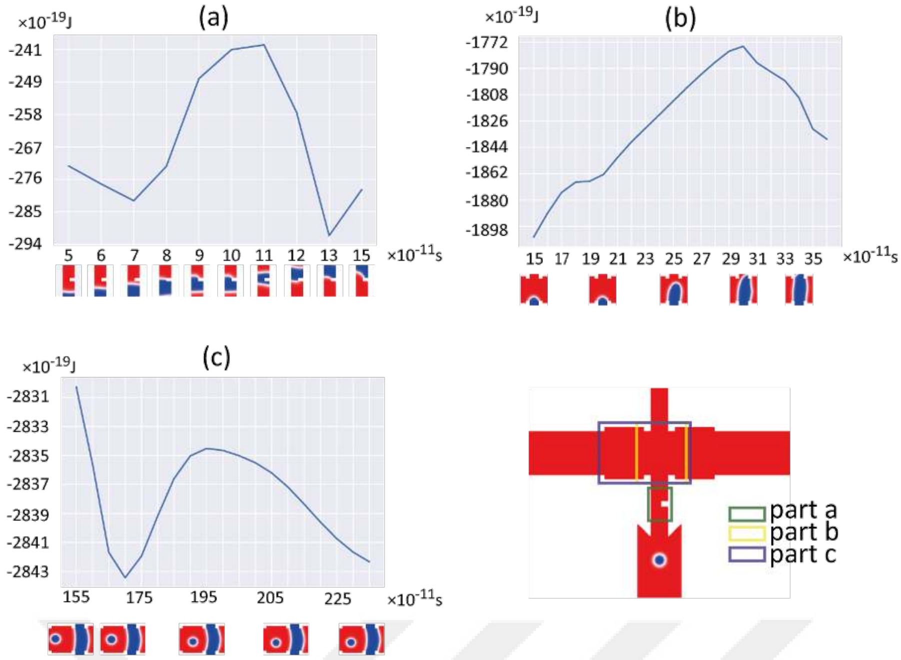

Figure 4.9. Development in the magnetic texture of the system and the corresponding magnetic energy. (a) The energy evolution of the passage of the leading DW and pinning of the back DW at the notch in the vertical channel. (b) The energy evolution of the bending and division of the DW at the junction of vertical and horizontal channels (c) the energy evolution of the skyrmion blocking by the vertical domain [91].

4.9.2 Domain Wall Bending and Division

As Figure 4.9 part (b) shows, when the leading DW reaches the junction, the spin-polarized current acts on the middle part while the big potential step of the edges keeps the ends of the DW in place. These two forces result in the bending and elongation of the DW. This bending and elongation increase the energy of the device. This process continues until the bent DW reaches the top side of the junction. On this side, there are sharp edges. These edges support a structure of three domain walls with lower energy than the bent domain wall. This makes a potential well for the system. Thus, the bent domain wall structure leads to three straight domain walls whose energy is lower than the bent domain wall.

4.9.3 Skyrmion-Domain Wall Repulsion

Figure 4.9 part (c) shows the energy development of the device when the vertical channel domain wall blocks the horizontal channel skyrmion. There is a decrease in the system's energy because of the reduction in the self-energy of skyrmion. This reduction happens because the skyrmion comes from a narrower channel that was exerting forces on it and keeping it smaller to the wider area where its size is closer to its natural size. Then the energy increases as the skyrmion is pushed closer to the domain wall. This energy increase leads to forces on the skyrmion and the domain wall. The energy reaches its peak when the skyrmion stops moving forward, and the effective field force in the direction of the STT force becomes equal to the STT force. Because of the complex effects of the domain bent domain wall, the geometry, and dipolar fields of the vertical channel, the effective field force has different components that lead to the rotation and dislocation of the skyrmion, which the system in the lower energy state.

4.10 Finite Temperature Stability

Robustness against thermal noise is a crucial aspect of the gate for the experimental setting. As the thermally induced random field of the Brown equation depends on the time step, the time step must be chosen small enough for reliable thermal modeling. This small timestep increases the computational cost of finite-temperature models. Thus, many studies of micromagnetic models ignore finite-temperature modeling. To better understand the difference between the computational costs of the micromagnetic models for zero or finite temperatures, we compare two identical models. The simulation time for the cascaded gates of section 4.6 on an NVIDIA Tesla k20m take 15 hours for the zero temperature and 111 hours for the finite temperature simulations. Nonetheless, our approach is to test all the designs with finite temperature modeling to ensure that it works correctly in finite temperature.

In the testing for finite temperature, the inverter gate was re-designed several times. Two main factors for thermal stability are the self-energy of magnetic textures and the increased complexity of the energy landscape.

As the thermal energy induces a random effective field on the magnetic textures, the shape and stability of the magnetic texture are affected by these effective fields. For a stable magnetic texture under finite temperature effect, its self-energy must be bigger enough than the thermal energy $k_B T$ at room temperature. The most convenient way to increase the self-energy of the textures without changing the material parameters and the XY plane energy landscape of the device is to increase the layer thickness. The complete thermal stability for all the stages of the device is achieved by a 6nm thick ferromagnetic layer.

The geometric complexities of the device make up a complicated energy landscape for the skyrmion motion. This complex energy landscape, in conjunction with the random temperature effects, might result in unfavorable consequences or even the disruption of the operation of the device. For example, when a skyrmion moves into the junction, the momentum from the change in the size of the skyrmion in conjunction with effective fields of thermal noise results in the destruction of the skyrmion. One possible solution to this problem is increasing the width of the horizontal channel. Although this increase in the width solves the problem of skyrmion annihilation at the junction, it decreases the stability of the blocking domain wall. Another possible solution is to introduce a magnetic field to shift the energy landscape so that the thermally induced randomness does not result in the annihilation of the skyrmion. We have found that an external magnetic field of 0.02 T is enough to keep the skyrmion from destruction. A change in material parameters such as the perpendicular magnetic anisotropy (PMA) also might increase the stability of the operations.

Supplementary movie S4.5 (Supplementary Video SV 5 Single inverter at 300 K without external field bias in [91]) shows the case without external magnetic field and Supplementary movie S4.6 (Supplementary Video SV 6 Single inverter at 300 K with external field B 0.02T in [91]) shows the case with external magnetic field of B=0.02 T. The successful operation of the cascaded case in the more complex case of 0→1→0 with finite temperature is also shown in supplementary movie S4.7 (Supplementary Video SV 7 Cascaded inverters at 300 K with 6 nm thick cobalt layer in [91])

4.10.1 Thermal Equilibrium

It is shown in section 3.8 that a nanotrack in contact with a substrate with constant temperature reaches an equilibrium temperature with constant temperature difference with the substrate. The clearance stage of the device is the stage with the highest dissipation power P_{in}, thus the equilibrium temperature of this stage is highest equilibrium temperature. For the parameters in Table 4.3 the equilibrium temperature difference of the device is 11.5 K. This means that if the substrate is kept at 300 K, the device temperature will be 311.5 K.

Table 4.3.The parameters for thermal equilibrium calculations

Parameter	Value
Electrical resistivity of Cobalt	$5.6 \times 10^{-8}\ \Omega \cdot \mathrm{m}$
Electrical resistivity of Platinum	$9.8 \times 10^{-8}\ \Omega \cdot \mathrm{m}$
Thermal conductance of Platinum	$71.6\ \mathrm{W} \cdot \mathrm{m}^{-1} \cdot \mathrm{K}^{-1}$
The thickness of the Cobalt layer	4nm
Thickness of platinum	4nm
Current density if the current passes a 100nm wide channel	$3.5 \times 10^{12}\ \mathrm{A} \cdot \mathrm{m}^{-2}$

4.11 Geometry Characterization

We design the desired interaction in the device by making a balance between the effective field and external forces of STT and the applied magnetic field. There are different handles to achieve these interactions, such as material parameters and geometry. Material parameters are global and cannot produce the complex energy landscape needed for the desired interactions in the device. The device's geometry is our only handle for designing the desired energy landscape. Although variations in the thickness of the layer (z-direction) can be a handle for the design of the energy landscape, we don't use it as such because of fabrication difficulties and unexpected effects such a change might bring about. Therefore, geometric features in XY dimensions are the principal factors in constructing the desired energy landscape. This section does a detailed analysis of the impacts of each geometric element on operation stages. We find the working window for each of the dimensions. This gives us a better understanding of the tolerances that can be handled to enhance the operation parameters.

4.11.1 The Effect of the Vertical Channel Width on the Initialization Stage

The vertical channel width of the inverter (VW) gate is 20 nm. The deviation on this width affects the initialization and blocking stages. The effect of width (VW) on the initialization stage is shown in Figure 4.10. According to this figure, a higher current density is needed to fill up the vertical channel as the channel gets wider. Regardless of the vertical channel size, the hard cutoff for moving the domain wall past the notch is 0.8×10^{12} A m^{-2}. The nominal current value for the initialization current is 1.4 × 10^{12} A m^{-2} which works for VWs of 20 ± 2 nm width.

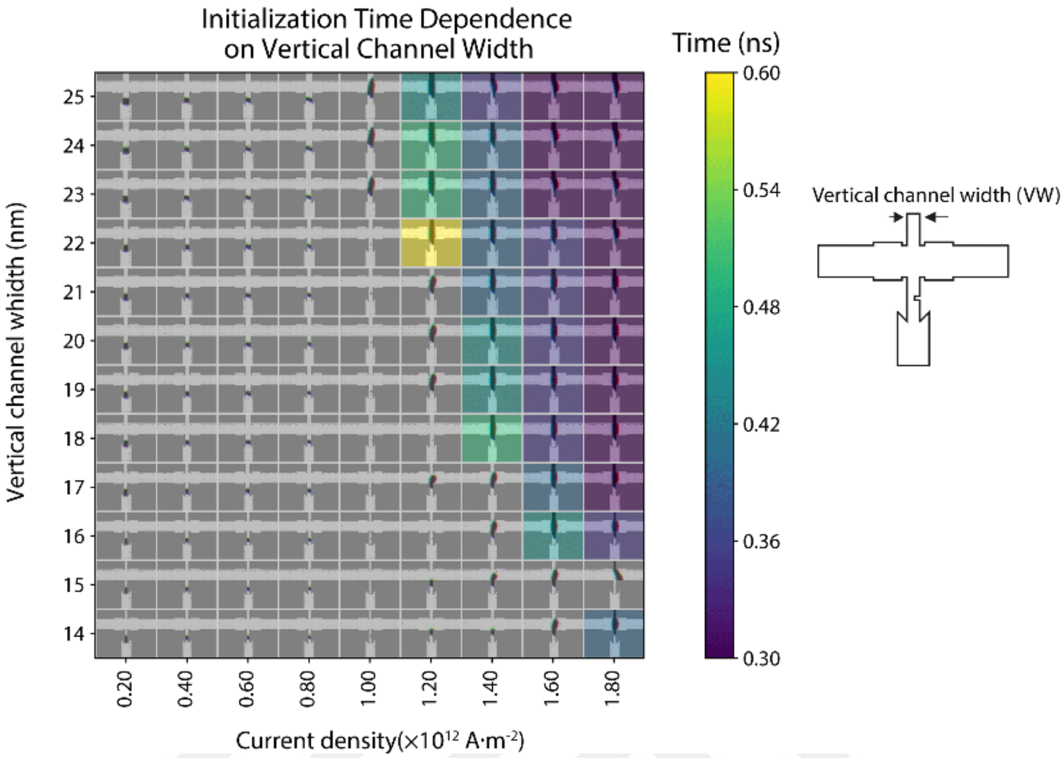

Figure 4.10. The effect of the vertical channel width and current density on initialization time

4.11.2 The effect of the Vertical Channel Width on the Stability of the Vertical Domain

To study the effect of vertical track width (VW) on the transmission stage, we first run the initialization stage with the current density values needed for the successful initialization stage and then run the transmission stage with different current values. Figure 4.11 shows the effect of VW on the stability of the vertical domain against the electric current in the horizontal track. Since all cases fail after a threshold value of 0.73 × 10^{12} A m^{-2}, the width of the vertical channel does not play a significant role in stabilizing the vertical domain. The top three rows of Figure 4.11 show that the vertical domains with 23-25 nm width show slightly less stability than the rest as their threshold current is 0.52 × 10^{12} A m^{-2}.

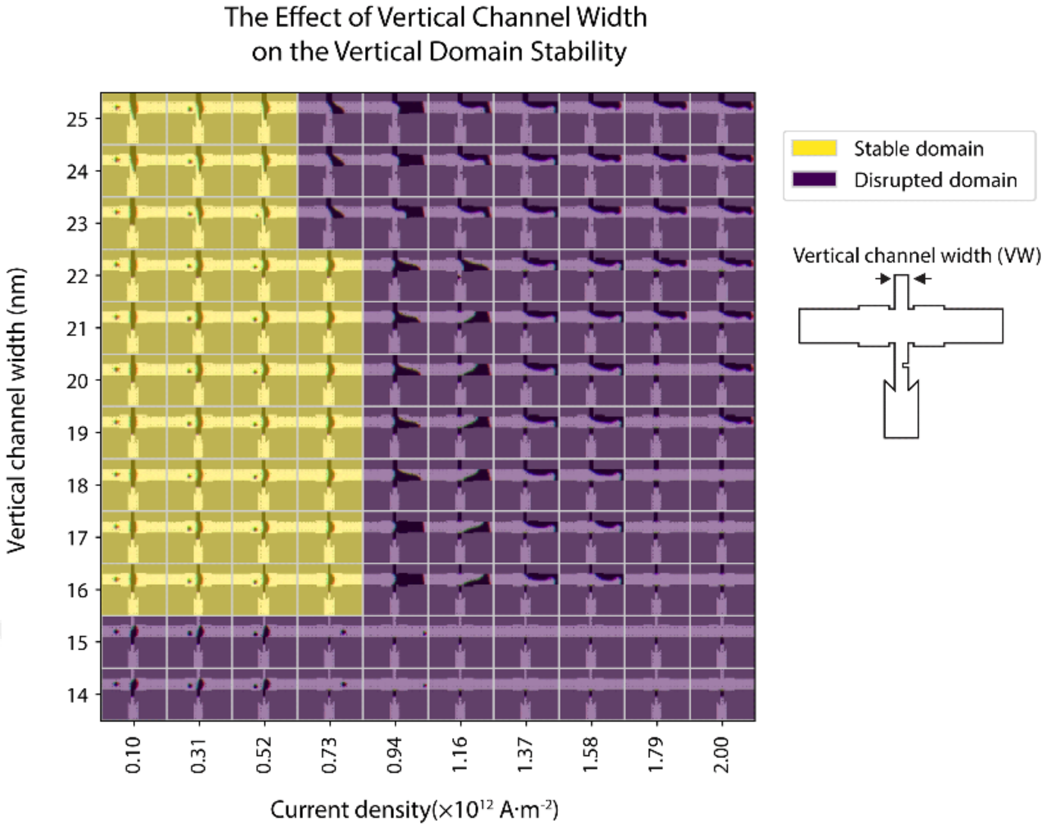

Figure 4.11.The effect of the vertical channel width on the stability of the vertical domain

4.11.3 The Effect of the Horizontal Channel Width on the Initialization Stage

The horizontal channel width (HW) is expected to have a direct effect on the initialization and transmission stages. Figure 4.12 shows the effect of HW on the initialization time. As one expects, the width of the horizontal channel affects the initialization time and viability. The nominal value for the horizontal channel width is 50 nm, HWs up to 62 nm, and down to 30 nm allow for successful initialization. For successful instances, wider horizontal channel results in a longer initialization time which is due to the longer path for the slower part of the initialization, i.e., the extension of the magnetic domain in the horizontal channel.

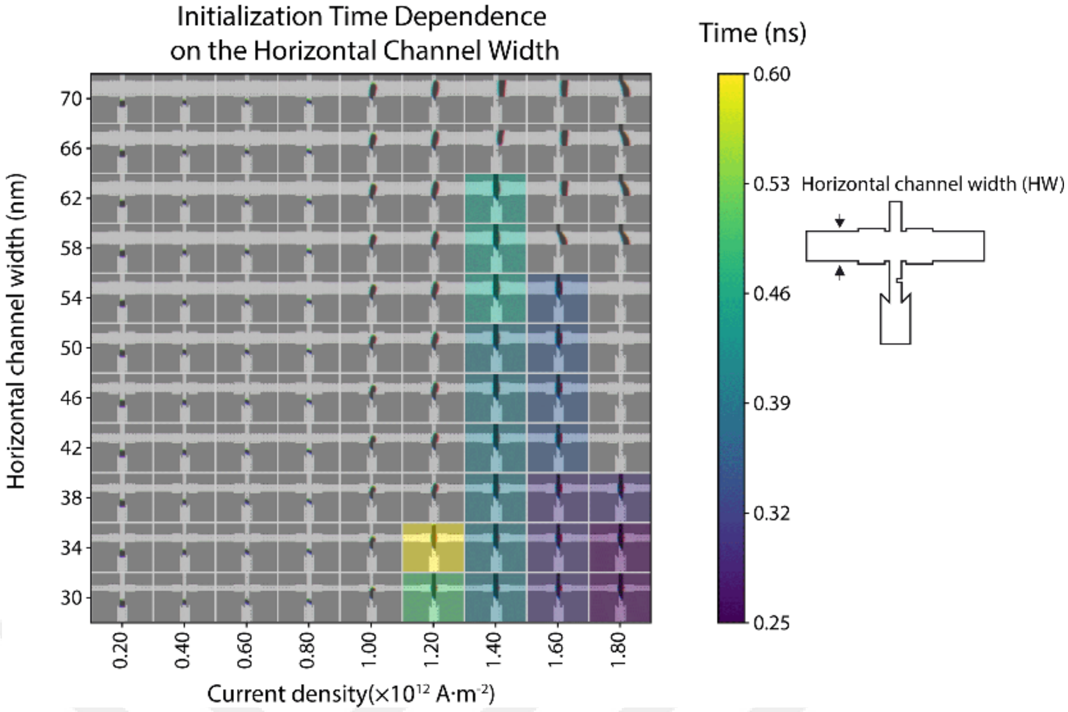

Figure 4.12. The effect of the horizontal channel width on the initialization time

4.11.4 The Effect of the Horizontal Channel Width on the Stability of the Vertical Domain

Figure 4.13 shows the effect of the horizontal channel width (HW) on the stability of the vertical domain against the force of the spin polarized electric current in the horizontal channel. This figure shows that the vertical domains in narrower horizontal channels have higher stability.

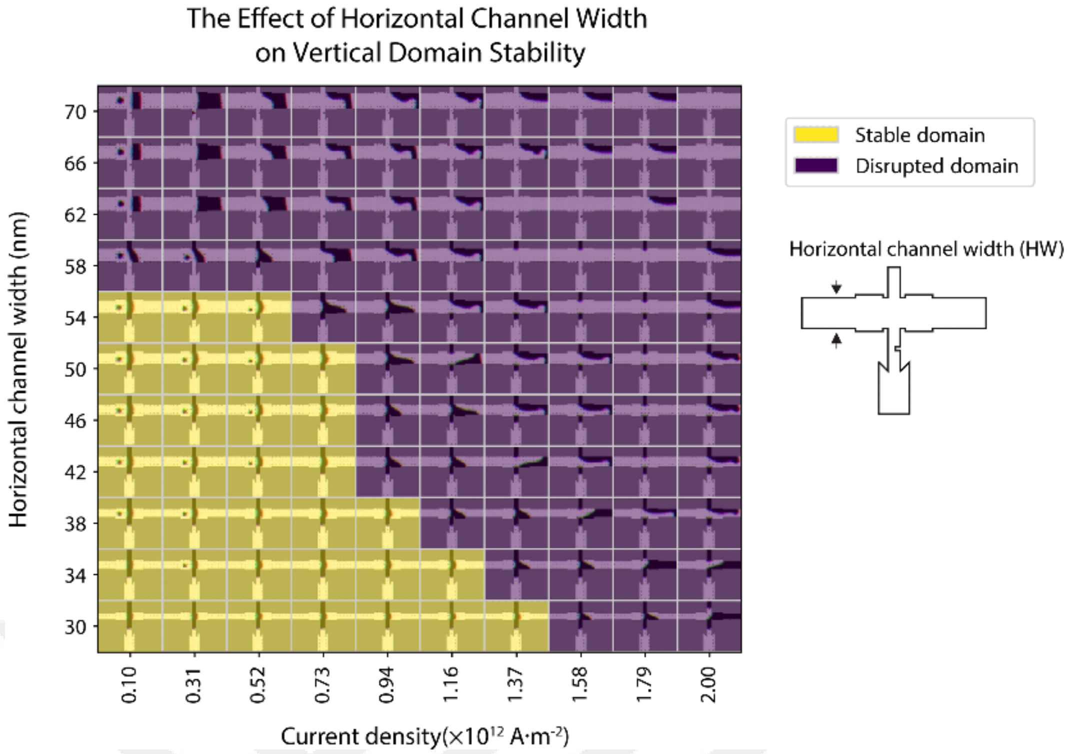

Figure 4.13. The effect of the horizontal channel width on the stability of the vertical domain

Since the disruption of the vertical domain causes the extension of the domain into the horizontal channel, we expect the clearance stage to fail for these cases. The clearance stage on the cases of Figure 4.13 is applied to check this. The results are shown in Figure 4.14. As expected, the clearance stage is unsuccessful for instances with a disrupted vertical domain.

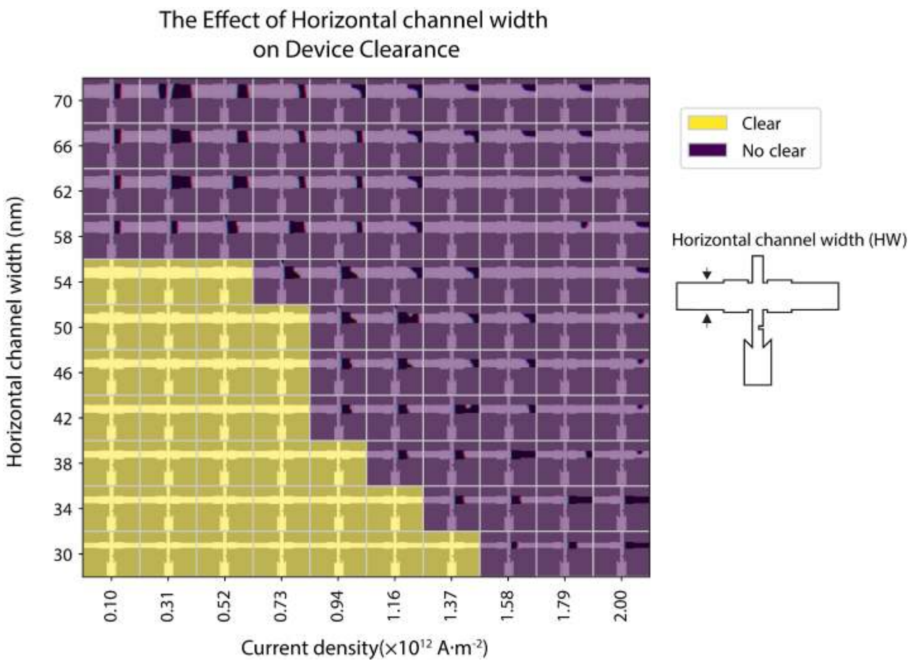

Figure 4.14. The effect of the horizontal channel width of the clearance stage

4.11.5 The Effect of the Center Notch Width on the Initialization Stage

The notch in the vertical track, "center notch", plays a crucial role in the initialization stage because it acts as an energy barrier to selectively pin domain walls and enable the expansion of the magnetic domain in the vertical channel.

Figure 4.15 shows the effect of the center notch width (CW) on the initialization stage. This data suggests a working window for the initialization stage of the device for notch widths between 7 and 12 nm in a 20nm nano-track.

According to this figure, if the notch is deep, the energy barrier is so high that even the leading domain wall cannot pass it. If the current density is high enough, the magnetic domain is destroyed at the notch (top right). If it is not high enough to destroy the domain, none of the domain walls can pass the notch, and we end up with a magnetic domain behind the center notch.

On the other hand, if the notch is shallow and the current density is high enough, both domain walls pass the notch, and we can't fill the vertical domain (bottom right).

The rest of the cases can be explained by considering the current density and the depth of the notch. The interplay of the energy barriers for two domain walls with the current density force allows for the selective domain wall pinning and initialization stage.

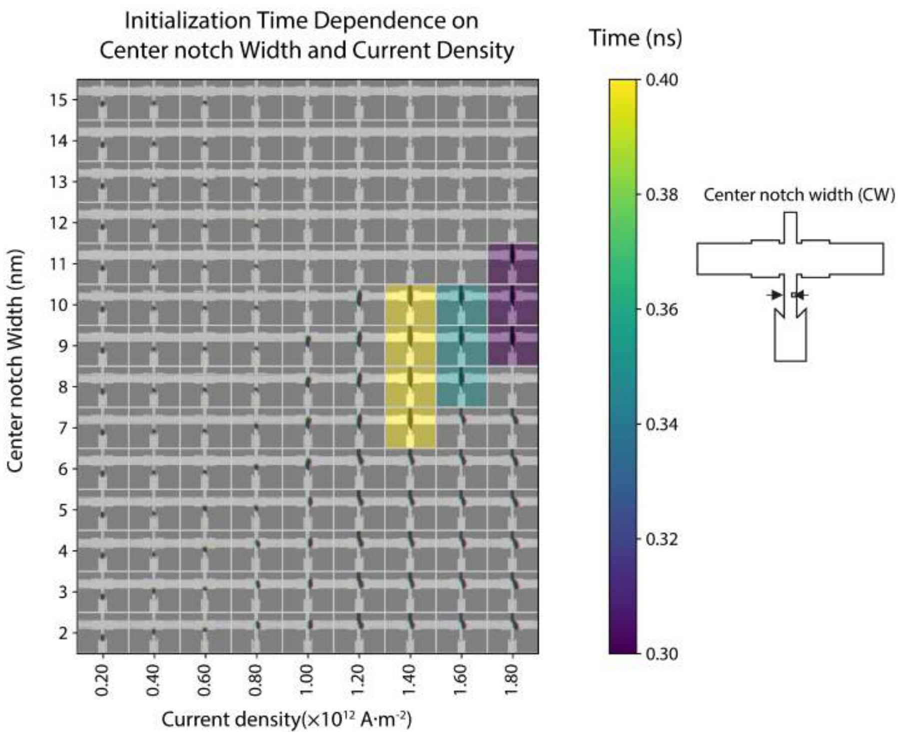

Figure 4.15. The effect of the central notch width and current density on the initialization stage

4.11.6 The Effect of the Center Notch Height on the Initialization Stage

The center notch high (CH) effect on the initialization stage is shown in Figure 4.16. All other geometric specifications are at nominal values. Since the center notch dimensions only affect the initialization stage, we don't study its influence on the vertical domain stability.

The initialization stage works with a high range of center notch heights from 4 to 14 nm. From Figure 4.10 and Figure 4.12 it is evident that current densities lower than 1.2×10^{12} A m^{-2} do not work for the initialization stage. Thus, the failed initialization stage at these current values in Figure 4.16 is not due to the CH.

An interesting effect of big CH is the reduction in the pinning force of the back domain wall due to the closer distance between the central notch and horizontal channel.

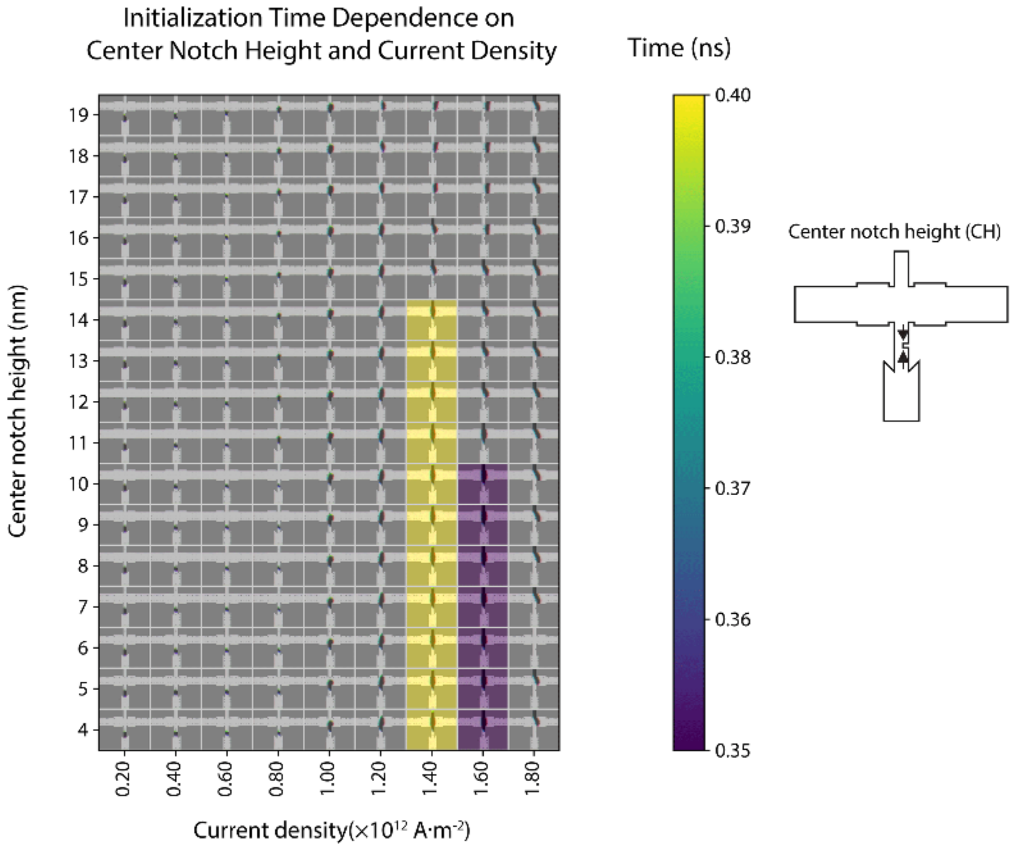

Figure 4.16. The effect of the center notch height and current density on the initialization stage

4.11.7 The Effect of Side-notch Distance

The side notches are essential in stabilizing the vertical magnetic domain against the current-induced force in the horizontal channel. Here we study the distance of the side notches from the vertical channel (SD). Side notches are symmetrical, i.e., they have the same distance from the vertical channel and have the same size.

Figure 4.17 shows the effect of side notch distance (SD) on the initialization stage for 60 nm wide side notches on a 50 nm horizontal track with a 20 nm wide vertical track. This figure shows that there is a working window for SD values. According to this result, the closer side notches help stabilize the vertical channel. As the applied current increases, the effect of SD diminishes because the current is strong enough to extend the magnetic domain.

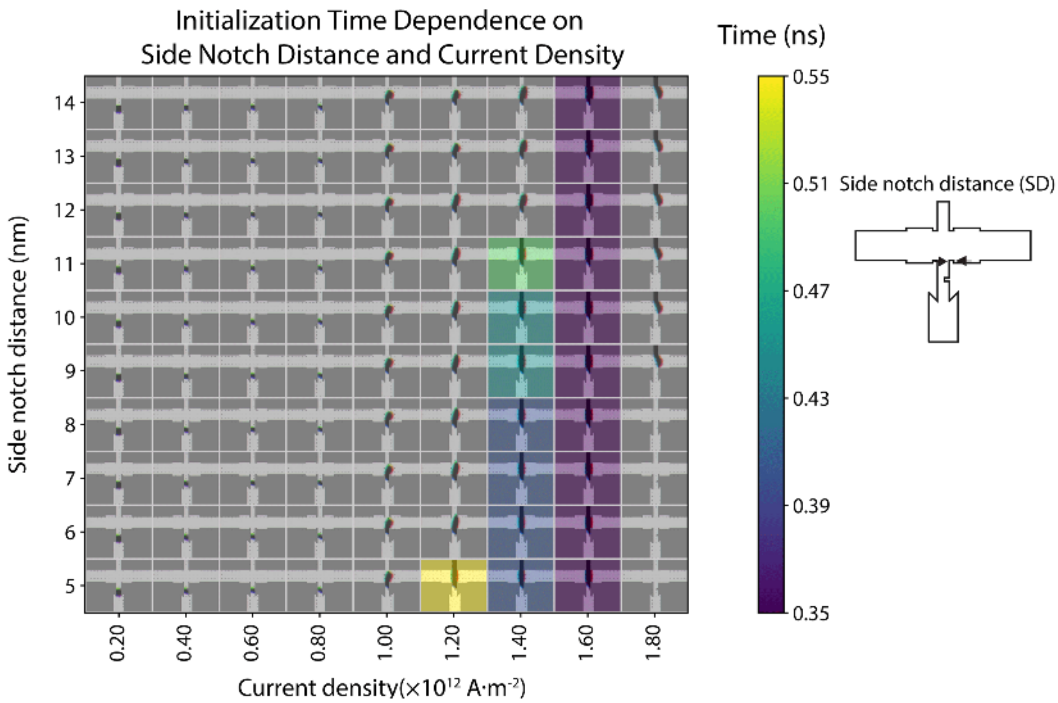

Figure 4.17. The effect of the side notch distance on the initialization stage

Figure 4.18 shows the effect of SD on the stability of the vertical domain in the transfer stage. The clear threshold for the disruption of the magnetic domain shows that SD does not have a significant effect on the stability of the vertical domain.

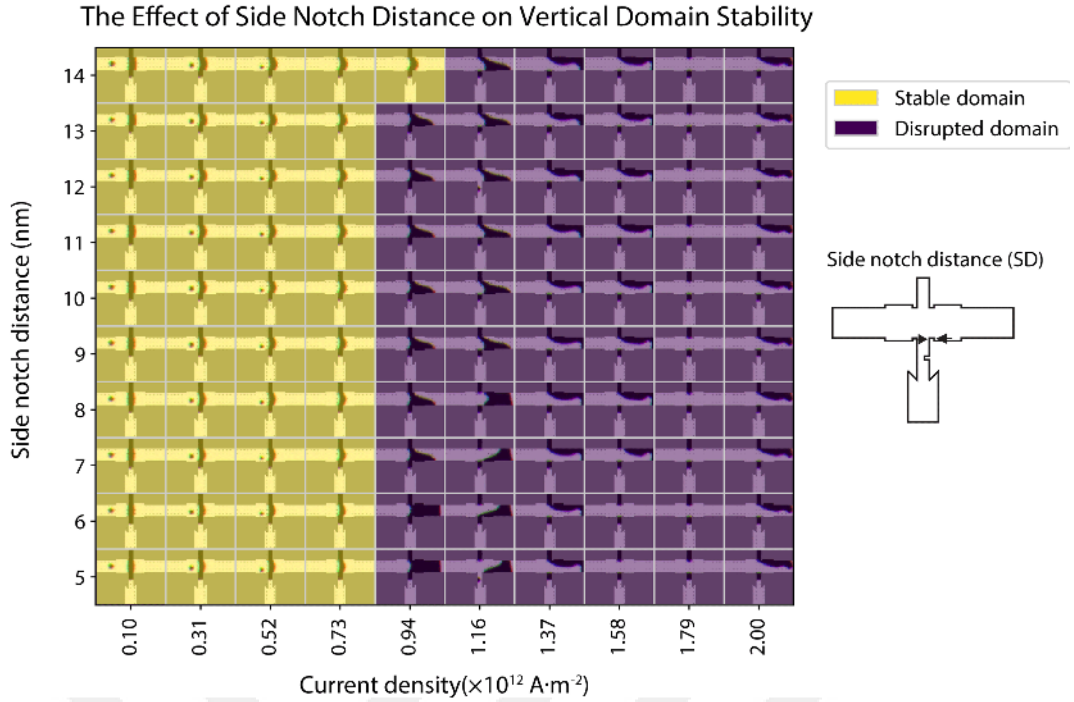

Figure 4.18. The effect of the side notch distance on the stability of the vertical domain

Although SD doesn't significantly affect the stability of the vertical domain in the transfer stage, it affects the clearance stage. If SD is too big, the area between the side notch and vertical domain acts as a pinning site and prevents the device's clearance stage. This effect is shown in Figure 4.19 as the clearance fails for almost all SD>9 nm. For these reasons, we have chosen SD = 8 nm as the nominal value for the side notch distance from the vertical domain.

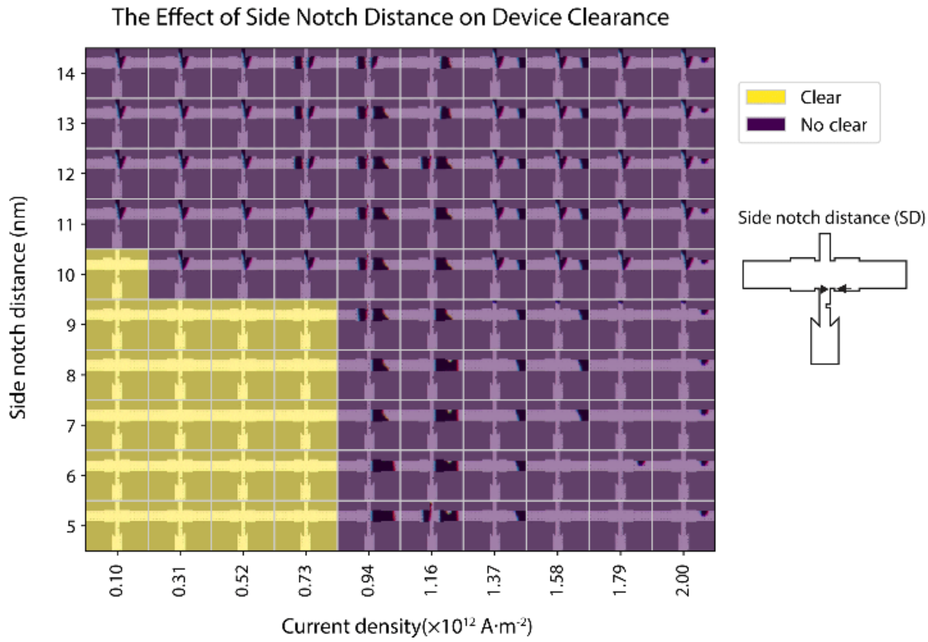

Figure 4.19. Effect of the side notch distance (SD) on the clearance stage

4.11.8 The Effect of the Side Notch Height

Side notch height (SH) produces the potential step for the vertical domain in the transfer stage. It is expected to affect the transfer stage and not have much effect in the initialization stage. This expectation is confirmed by studying the initialization stage for different SH values. Figure 4.20 shows the independence of the initialization on SH, as we see that for working currents, the initialization stage is successful for almost all values of SH.

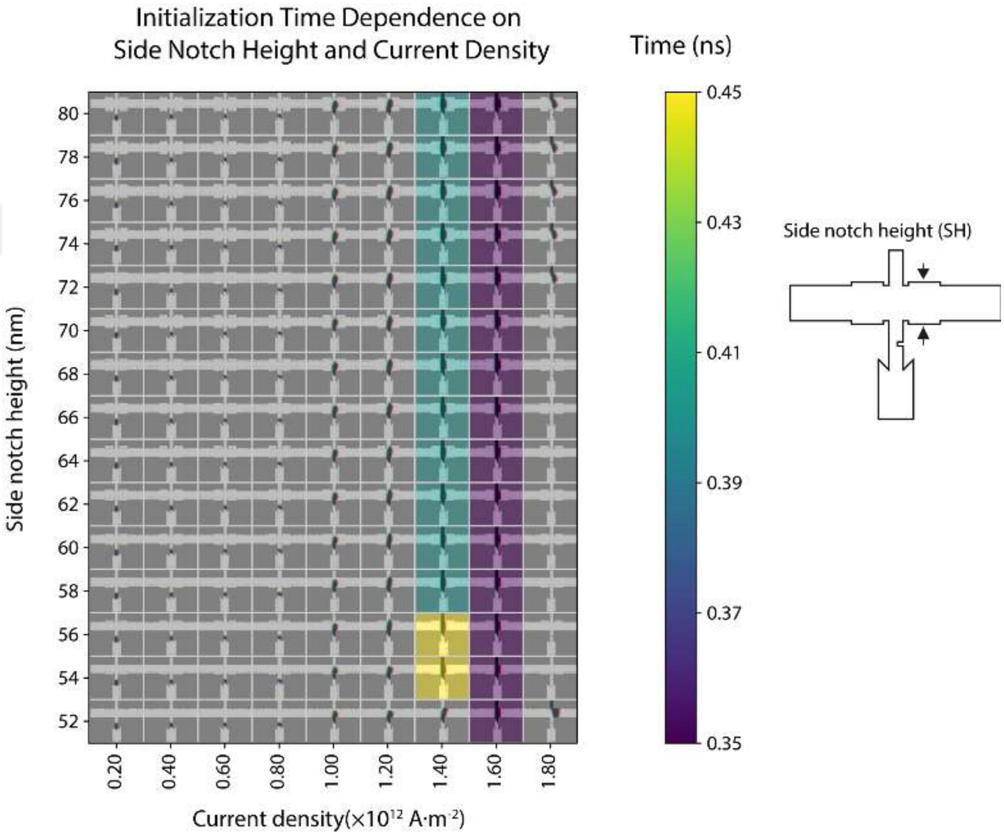

Figure 4.20.The effect of the side notch heights on the initialization stage time

Figure 4.21 shows the effect of the side notch height on the stability of the vertical domain while the other dimensions are kept at their nominal values. This figure shows that the higher SH increases the stability of the magnetic domain. This happens because higher SH introduces a bigger energy barrier to the vertical domain wall.

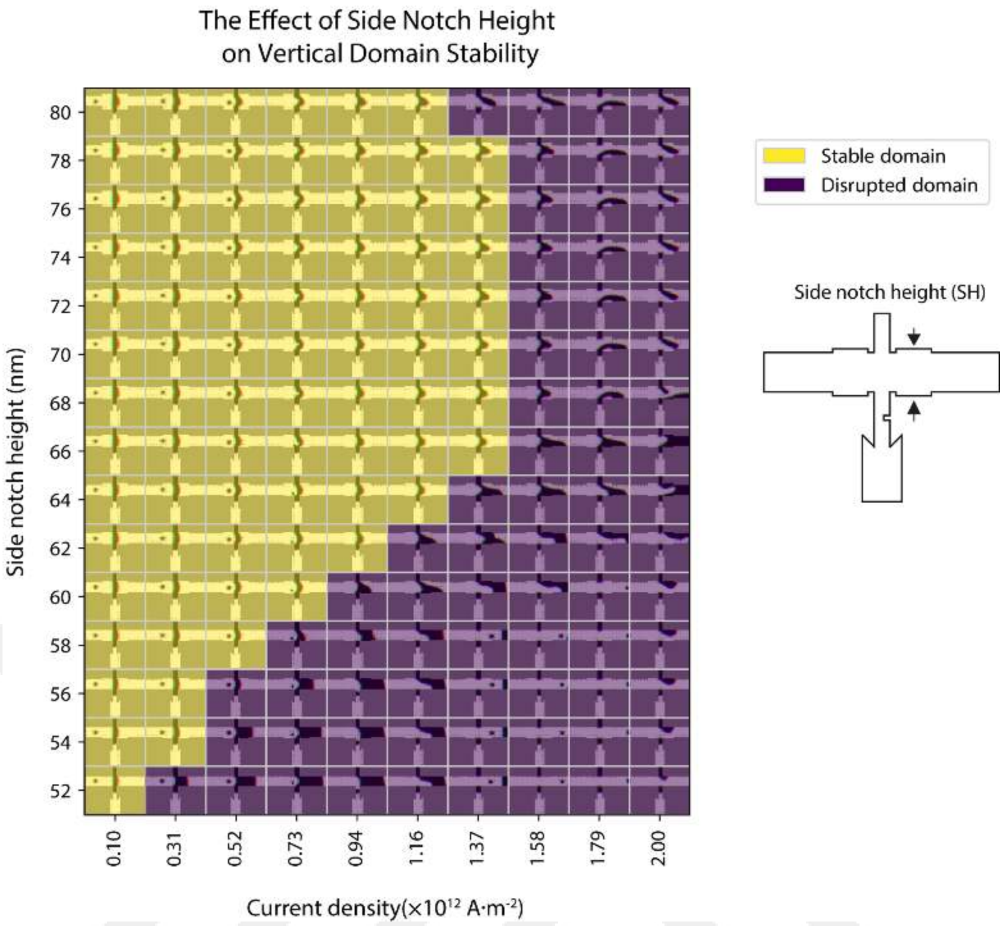

Figure 4.21. Effect of the side notch height on the stability of the vertical domain

4.12 Damping and Non-adiabaticity of Spin Transfer Torque

The damping parameter (α) and the non-adiabaticity of the spin-transfer torque (ξ) play crucial roles in the dynamics of the current-driven magnetic systems. Their difference is also important because it plays as the precession-like force in the motion of skyrmions and domain walls, resulting in the traverse motion of skyrmions, also known as the skyrmion Hall effect (SKHE). The effect of this difference on the motion of skyrmions has been studied more than its effect on the domain walls in the literature.

Figure 4.22 shows the effect of these two parameters on the initialization stage. There is a window of operation for α and ξ and both parameters are subject to tolerance. This working window gets wider for higher values of these parameters.

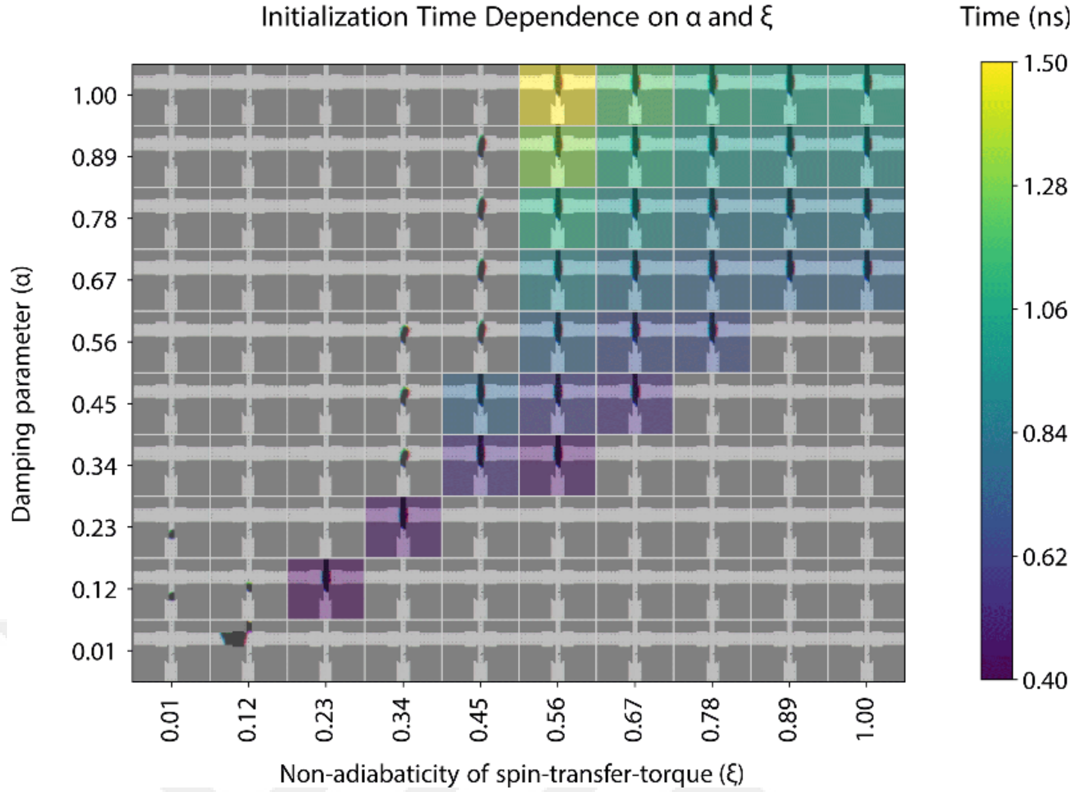

Figure 4.22. Initialization time dependence on the damping parameter(α) and the non-adiabaticity of the spin-transfer torque(ξ)

Figure 4.23 Shows the effect of α and ξ on the transmission stage. According to this figure, we have a wider range for the values of these parameters, which increases the experimental viability of the device.

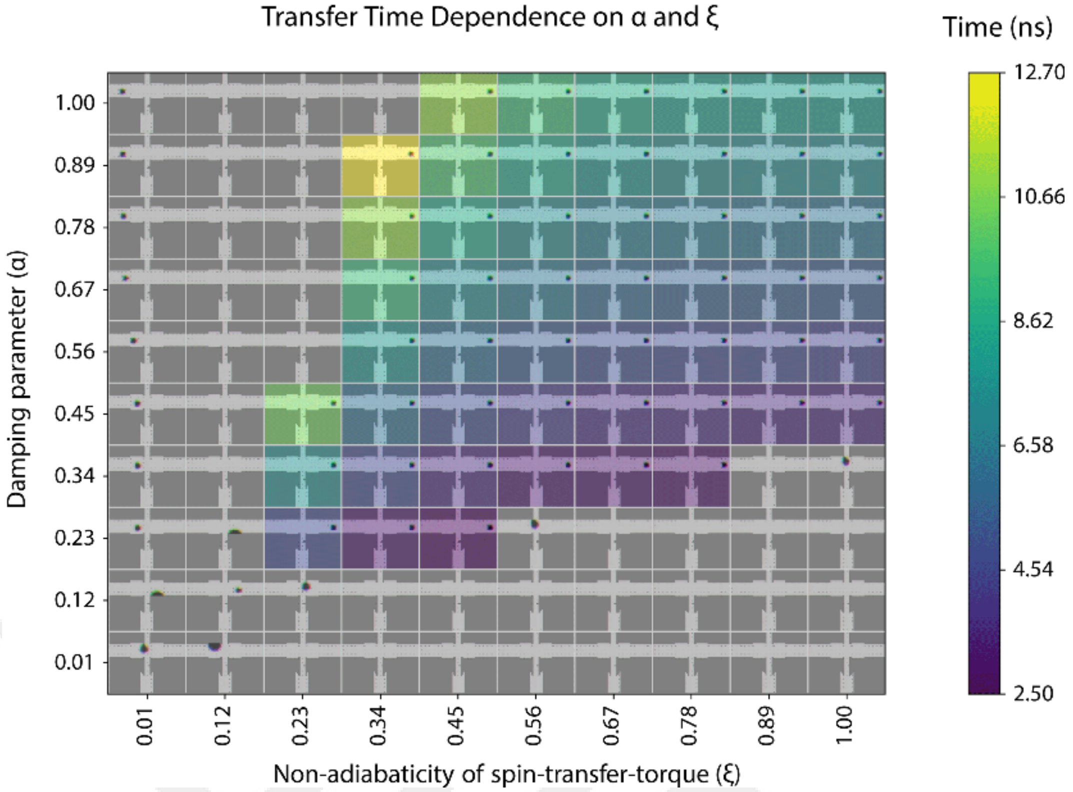

Figure 4.23. Transfer time dependence on the damping parameter(α) and the non-adiabaticity of the spin-transfer torque(ξ)

Another insight from Figure 4.22 and Figure 4.23 is the effects of α and ξ on the operation time of each stage. According to equation (2.109) the following ratio:

$$\frac{1+\xi\alpha}{1+\alpha^2} \tag{4.12}$$

plays the main role in the movement of the magnetic structure in the direction of the current as it is the coefficient of the damping-like term in the LLG equation. This is also confirmed by checking that the times of operation for the working cases are higher for the top left cases where $\xi < \alpha$ and lower for the bottom right cases where $\xi > \alpha$.

4.13 The Effect of Polycrystallinity

Polycrystalline regions arise in fabrication because of changes in growth directions. The form of these regions follows the Voronoi tessellations. Voronoi tessellations are regions that have equidistance boundaries from their center and the center of their adjacent region. The magnetic parameters are randomly distributed between regions. Two main magnetic parameters that affect the working of the device are the saturation magnetization (M_s), and perpendicular magnetic anisotropy (PMA) value or direction. The effect of the polycrystallinity has been investigated in simple geometries before [144, 145]. The inverter gate of this chapter has a more complex geometry and might causr a more critical dependence on polycrystallinity. Figure 4.24 shows a sample change in the magnetic parameters from polycrystallinity. This figure shows the deviation from initial value of each parameter based on the Gaussian noise. The value for each region is a sample from the distribution of the gaussian distribution

$$X = \mathcal{N}(X_{initial}, \sigma^2) \tag{4.13}$$

Where X is the value of the magnetic parameter in each region, $X_{initial}$ is the nominal value of the magnetic parameter and σ is the standard deviation of the Gaussian noise. The nominal value for the PMA is $K_{u1(initial)} = 8 \times 10^5 \; J \, m^{-3}$ and for saturation magnetization is $M_{s(initial)} = 5.8 \; \times 10^5 \; A \, m^{-1}$. For Figure 4.24 $\sigma_k = 0.1 \; K_{u1(initial)}$ and $\sigma_M = 0.05 \; M_{s(initial)}$. The effects of the changes in material parameters in the operation of the device are interesting and complex. The changes in PMA mostly affect the speed of skyrmion motion and the changes in the saturation magnetization mostly realize in the changes in the sizes of the skyrmion when moving in the track. The safe margins for the PMA and M_s are the noises with 5% of the standard deviation from the nominal value i.e., $\sigma_k = 0.05 \; K_{u1(initial)}$ and $\sigma_M = 0.05 \; M_{s(initial)}$. Supplementary Movie S4.8 shows the block stage for %5 change of the saturation magnetization. Supplementary Movie S4.9 shows the transfer stage for the same distribution. Supplementary movie S4.10 shows the block stage for the 5% change in the PMA. Supplementary movie S4.11 shows the pass stage for the 5% change in the PMA.

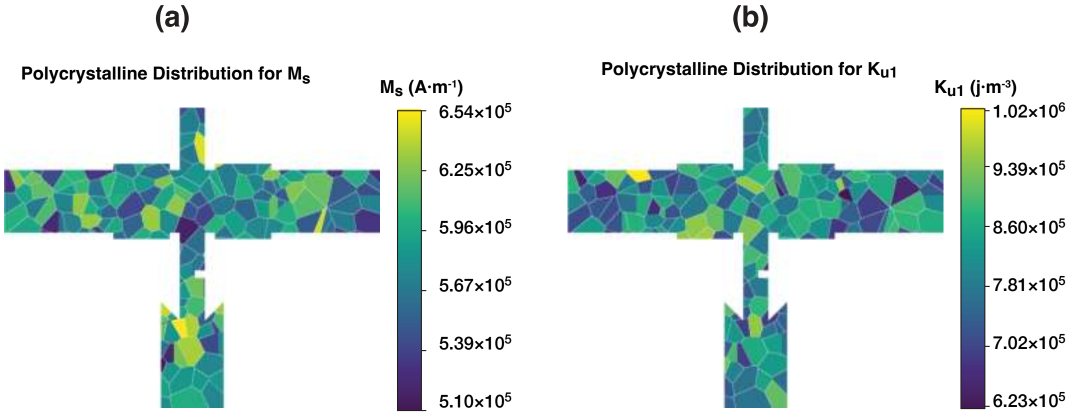

Figure 4.24. The effect of polycrystallinity on the value of saturation magnetization and PMA. (a) The Voronoi tessellation values for saturation magnetization taken from a sample of Gaussian distribution with the mean of $M_{s(initial)} = 5.8 \times 10^5\, A\, m^{-1}$ and standard deviation of $\sigma_M = 0.05\, M_{s(initial)}$. (b) (a) The Voronoi tessellation values for PMA taken from a sample of Gaussian distribution with the mean of $K_{u1(initial)} = 8 \times 10^5\, J\, m^{-3}$ and standard deviation of $\sigma_k = 0.1\, K_{u1(initial)}$ [94]

4.14 The Effect of Sidewall Roughness and Geometric Noise

In a real setting the borders of the device are not smooth and are subjected to have geometric noise. Since the geometry is an important factor in the working of the device, the effect of the sidewall roughness also needs to be investigated. The sidewall roughness with different feature sizes have been added to the device and the functioning of the device is investigated under these noises. The device's operation is confirmed to be robust under sidewall roughness up to 6 nm. Random sparse pinning sites with these sizes also are shown to not hinder the operation of the device. Figure 4.25 shows the operation of the device with sidewall roughness in key moments. Supplementary movie S4.12 shows the operation for 0→1 case and supplementary movie S4.13 shows the operation of the device for the case 1→0.

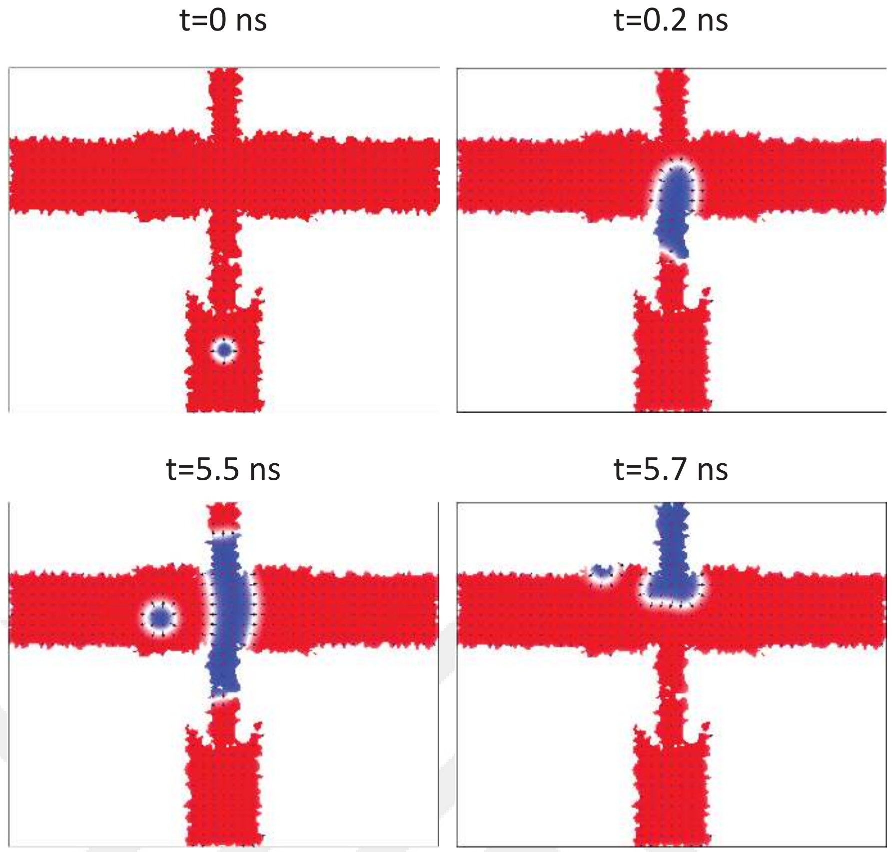

Figure 4.25. Device operation under 6nm sidewall roughness and pinning sites.

4.15 Summary

This chapter introduced the inverter gate as a vital part of a complete skyrmionic logic system. A detailed device blueprint was provided, including the geometric dimensions and materials. Followed by an energy analysis, sequential snapshots of the work cycle of the device and an overview of the time domain evolution of the magnetization profile for both cases of high and low inputs have been presented. The energy analysis part split the energy consumption into two components: magnetic energy and Joule heating energy. The magnetic energy integral computed the device's lower bound energy consumption. This energy amounted to hundreds of $k_B T$ at room temperature (T = 300K).

On the other hand, the Joule heating energy amounted to much larger energy of ~60 fJ. A thermal stability calculation showed that an equilibrium temperature of ~300 K is reached with a proper passive heat sink. This temperature has been used in finite temperature modeling to demonstrate robust operation at room temperature. The device cascadability as the essential feature for the skyrmionics logic system of the next chapter was touched upon, and a cascaded version of two inverter gates was also presented. This cascaded version of the gates produced the AND operation.

The rich physics of the magnetic inverter gate was discussed by deriving the equation of motion of a domain wall under the LLG equation and spin-polarized current. We showed that in the special case of $\xi = \alpha$ that eliminates the precession-like term of the LLG equation, the shape of a magnetic texture is invariant, and the motion directly depends on the current density, and depends inversely on saturation magnetization. The highly non-trivial effect of geometry affects the motion or change the shape. These geometry effects are used in this study to produce the intended operations. Furthermore, a justification for the discussion of a generalized force between magnetic textures was also provided. These forces are mainly the repulsive forces of: skyrmion-skyrmion, skyrmions-domain walls, skyrmion-boundary, and boundary-domain wall. A detailed discussion about the development of the magnetic textures based on these forces and their ties to the magnetic energy was then provided.

Geometric dimensions are crucial parameters for the operation of the device. The acceptable tolerances of these values and the working stages affected by these dimensions were discussed by phase diagrams showing the sweeps of these values. These studies show that the nominal values used for these dimensions are all subject to tolerances comparable to the magnitude of these values. Noises from fabrication process also can adversely affect the device operation. Polycrystallinity and sidewall roughness are among the most important fabrications noises. The effects of these two sources of noises were also discussed in this chapter.

A common simplification for the current driven motion of the skyrmions we have used is considering $\xi = \alpha$, which might not necessarily hold in the real conditions. Here we also swept the values of these parameters to study their combined effect. The $\xi = \alpha$ eliminates the precession-like torque in the LLG equation. Thiele has shown that for textures with non-zero topological charge, the precession-like term leads to the traverse motion named the skyrmion Hall effect in the literature. Here we demonstrated a tolerance for both parameters and their deviation from the equality constraint. Interestingly, this tolerance is much broader for the transmission stage than the initialization stage. We showed that the INVERTER gate's functionality is retained even when its geometry is subject to tolerance, bringing it closer to real-world implementations. Further reduction of energy consumption can be achieved by replacing magnetic and nonmagnetic metals with their insulating or semiconducting counterparts. Thus, Joule heating resulting from the electric current flow in the device could be reduced by 3-4 magnitudes. Magnetic layers with lower magnetic moments could also help reduce the power consumption of skyrmion inverter logic.

This chapter went through the detailed specification and studies of the inverter gate. The next chapter will be devoted to the scalable skyrmionics logic system. The inverter gate lies at the heart of this system and together with the next chapter, cascaded skyrmion logic circuit and system functionalities can be achieved.

Chapter 5

SKYRMION LOGIC SYSTEM

5.1 Introduction

The last chapter focused on the physical properties of the INVERTER gate. The focus of the last chapter was on the inverting properties of the INVERTER, hence the name of the gate. The subsection 4.6.2 touched upon changing the perspective to the cascaded version of two INVERTER gates to produce an AND gate. This was an important milestone. Although the cascadability of the INVERTER gate has been shown, there are remaining steps that needs to be taken to make a system.

The geometry of the INVERTER gate resides inside a rectangular plane of 300 nm × 240 nm. This geometry works only when the gates are put together without rotation. Moreover, the concatenation of the gates is not straightforward and needs deliberate placement. For an automated system, a more symmetrical shape is needed. In this chapter we change the INVERTER gate's geometry from a rectangle to a square with input/output channels in the middle of the square.

Although the INVERTER gate has shown to have cascadability, this is not enough for a logic system as the notion of universality is important for a system of gates. In this chapter we prove that the INVERTER gate together with AND and OR gates are universal. Section 5.2 is devoted to the universality of the INVERTER, OR and AND gates. Moreover, the INVERTER gate, while universal, is not enough for producing a system. Other blocks are required for this aim. In this chapter all these blocks are introduced too. Section 5.4 introduces these blocks in detail. The geometry and mathematical equations of the blocks are explained in 5.4.

We have used the term "gate" for the INVERTER gate as it acts as a gate i.e., an object with inputs and outputs that does Boolean algebraic operation on the inputs and puts the results in the output. In this chapter, we use the INVERTER as a part of a larger system. We call these parts of the system "blocks" and the cascaded object made from them a "gate". Thus, the INVERTER by itself is a block and when put together to make an object that has inputs and outputs, we call that object a “gate”. For example, in section 5.2 a NOR gate is made from two INVERTER blocks.

This rest of the materials in this chapter are devoted to the protocol of emulation, and the emulation and simulation software.

5.2 Universality of the INVERTER Operation with AND and OR

If the vertical input, horizontal input, and the output of the INVERTER block are labeled x, y, z respectively. The function of this block is:

$$z = \bar{x}y, \tag{5.1}$$

where the presence of a skyrmion in a time interval Δt represents Boolean' 1', and the absence of a skyrmion is '0'. By combining two blocks where the horizontal input of the first block is Boolean' 1', for the output of the second gate, we can write:

$$o = \bar{u}z = \bar{u}(\bar{x}1) = \bar{u}\bar{x} = \overline{u + x} \tag{5.2}$$

which is the NOR gate. The INVERTER block design is a very general architecture such that one INVERTER covers the Boolean AND in equation 5.1 and two INVERTER blocks cover the Boolean NOR in equation 5.2. This proves that the INVERTER is a universal gate set. The implication of this result is that the combination of the INVERTER blocks can produce arbitrary skyrmionics logic systems.

Figure 5.1 (a) shows the INVERTER block. The signals of equation (5.1) are denoted with arrows that shows the flow of the skyrmion in the specified direction. Under the block, the circuit schematic of the block and the truth table of the block are also shown. The circuit schematic of the INVERTER block consists of an AND gate with an inverted input as equation (5.1) shows. The hollow circuit at the x input denotes the inversion in the schematics of digital electronics. Hence the hollow circle at the x input of the schematics of the block. The truth table shows the output for different combinations of the input.

Figure 5.1 (b) shows the magnetic configuration for different rows of the truth table. The snapshots are taken to capture the critical moments of the magnetic configurations and they do not represent the end-of-cycle moment of the block since at the clearance stage the middle part of the block will be cleared, and the vertical magnetic domain will not exist.

Figure 5.1 (c) shows the cascaded INVERTER blocks as denoted by the equation (5.2). Under the geometric representation of the cascaded blocks, the circuit schematics and the truth table of the cascaded blocks are shown.

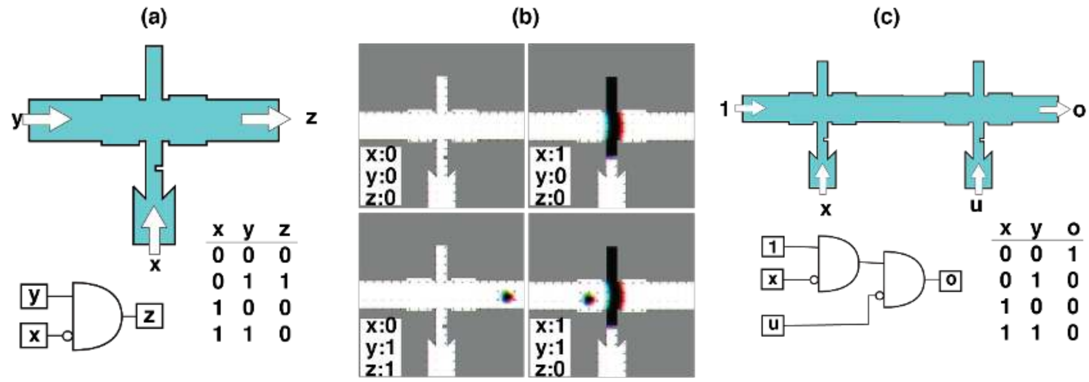

Figure 5.1.The cascading of INVERTER blocks. (a) inputs and output of the INVERTER. (b) the modeling situations for different inputs. (c) NOR gate from cascading two INVERTER blocks.

5.3 Block Model

Although the mathematical proof of the universality of the INVERTER block and a cascade of two blocks to make a NOR gate was provided in the last section, crucial steps to reach a complete system are still missing. Here we define a box model for the blocks of the skyrmion logic system. All the blocks of this system follow this box model.

5.3.1 Block Model

Figure 5.2 shows the black box model of a skyrmion logic block. Each block is a square with four input/output channels. Channels have the same width and are centrally aligned on the sides of the square. As this figure shows, the channels are indexed 0/1/2/3 for the positions of top/right/bottom/left. According to the labels of Figure 5.1, for the INVERTER block, x is at channel i_2, y is at channel i_3, and z is at channel i_1. Not all the channels need to be used in each block. For example, Channel i_0 of the INVERTER block is NULL and does not accept inputs or outputs.

The sizes of the blocks in this study are of 300 nm $\times$ 300 nm and each channel has a width of 50 nm.

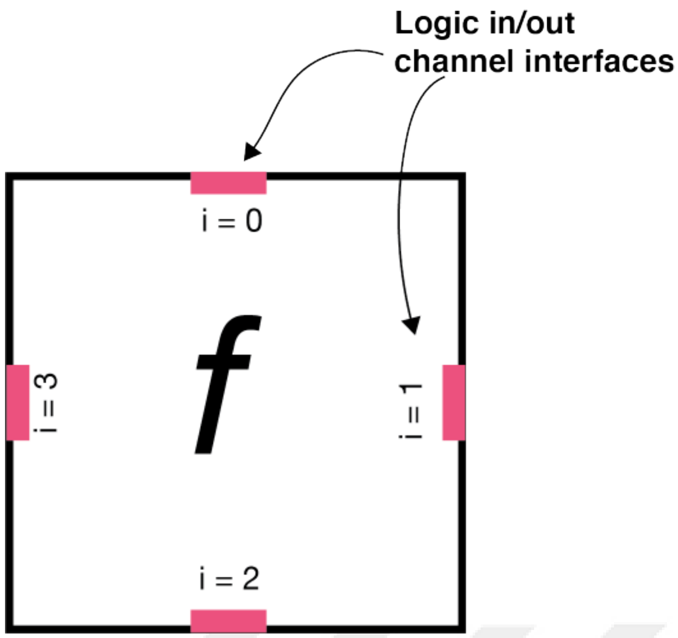

Figure 5.2. The black box model of the skyrmion logic block. Each block is a square with four channels that have the same width and are at the center of the sides of the block.

5.3.2 The Logic Function of a Block

The logic function of a block can be described by relations between the values of the channels at the end of a work cycle based on their values at the beginning of the operation cycle. The INVERTER block has the following state equation:

$$\begin{cases} i_0(T) = NULL \\ i_1(T) = \overline{i_2(0)}i_3(0) \\ i_2(T) = 0 \\ i_3(T) = 0 \end{cases} \tag{5.3}$$

This equation indicates the values of the INVERTER block's channels at the end of an operation cycle, i.e., at time t = T. If a skyrmion exists at i_2, in the beginning of operation, it will fill up the vertical channel and later cleared up. Thus, the value of channel i_2 will always be zero at the end of the operation. Similarly, if a skyrmion exists at the i_3 channel in the beginning, it would not exist there at the end of the work cycle. The output channel is i_1. We have already established the logic operation of the INVERTER block in equation (5.1). This result is shown again in (5.3) in terms of block channel indices.

5.4 Blocks

We have established the concept of the black box block with the input/output channels. The individual blocks, their geometry, and other specifications are introduced in this section. All the blocks that are necessary for the system will be presented here. Other blocks can also be added to the system later.

5.4.1 INVERTER and Its Variations

INVERTER

INVERTER block was introduced in the last chapter.

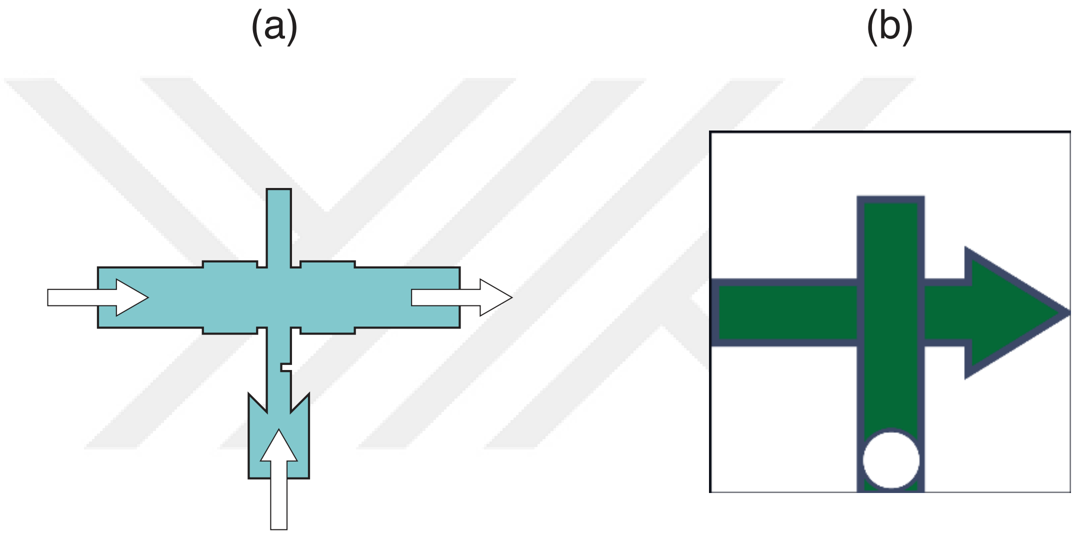

Figure 5.3.The geometry, skyrmion flow and schematics of the inverter block. (a) the geometry of the inverter block with the direction of the flow of the skyrmions (b) the schematic of the inverter block. The white circle in the schematic shows the inverted input.

Equation (5.3) shows the INVERTER block's state equation.

$$\begin{cases} i_0(T) = NULL \\ i_1(T) = \overline{i_2(0)} i_3(0) \\ i_2(T) = 0 \\ i_3(T) = 0 \end{cases}$$

FLIPPED INVERTER

The FLIPPED INVERTER is the inverter block where the flow of the skyrmion in the horizontal track is from right to left. Although the existence of the flipped version of the inverter block is not essential to a universal Boolean logic system, it helps a more concise design as in some instances the designs can get unnecessarily large without it.

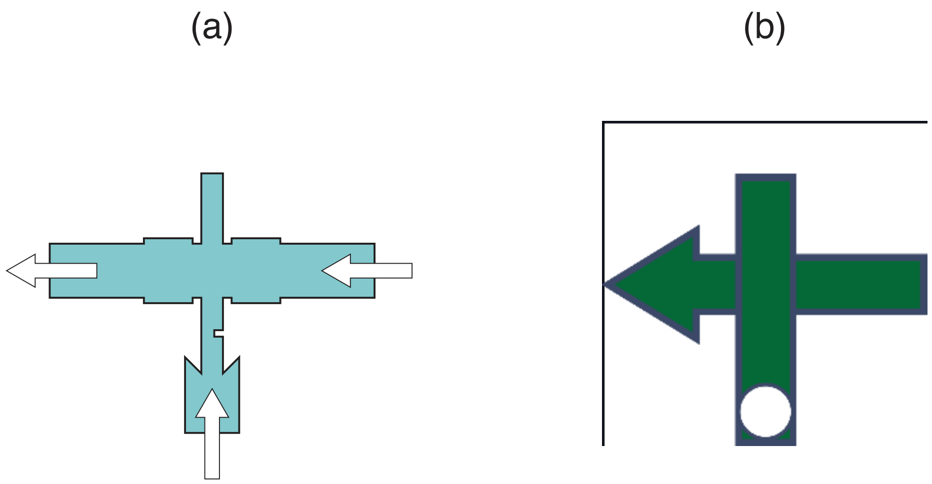

Figure 5.4.The geometry, skyrmion flow and the schematic of the flipped inverter block.

FLIPPED INVERTER block has the following state equation:

$$\begin{cases} i_0(T) = NULL \\ i_1(T) = 0 \\ i_2(T) = 0 \\ i_3(T) = \overline{i_2(0)}i_1(0) \end{cases} \quad (5.4)$$

INVERTER-TRANSFER

The vertical skyrmion is lost in the operation of the INVERTER block. The loss of the vertical skyrmion might not be desirable in some cases. Adding a channel at the top of the INVERTER block allows for the reuse of the vertical channel's skyrmion.

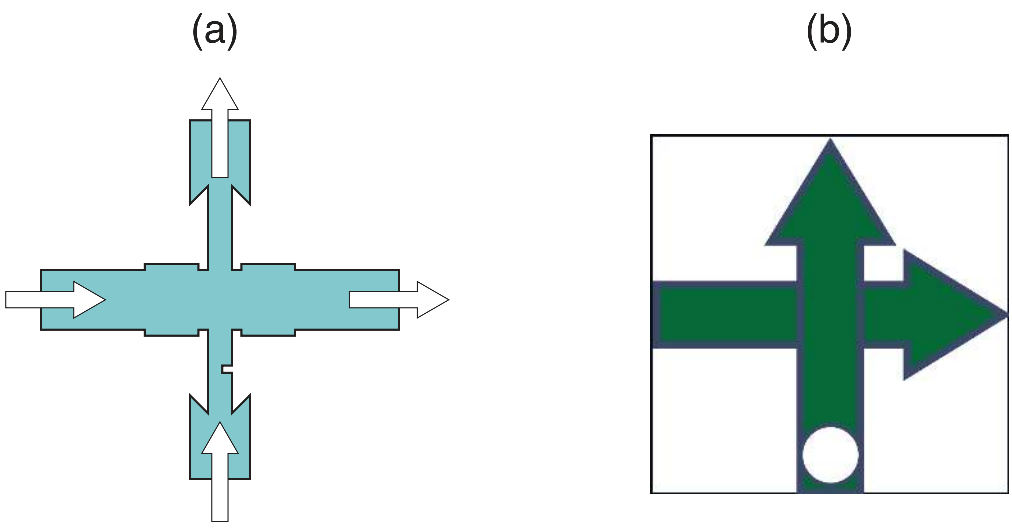

Figure 5.5.The INVERTER-TRANSFER geometry, skyrmion flow and schematic

The INVERTER-TRANSFER block has the following state equation:

$$\begin{cases} i_0(T) = i_2(0) \\ i_1(T) = \overline{i_2(0)}\, i_3(0) \\ i_2(T) = 0 \\ i_3(T) = 0 \end{cases} \tag{5.5}$$

5.4.2 Junctions

The geometry of the JUNCTION blocks is similar to that of the INVERTER-TRANSFER block. Only the timing of the spin polarized current, i.e., the stages of the operation are different.

JUNCTION UP-RIGHT:

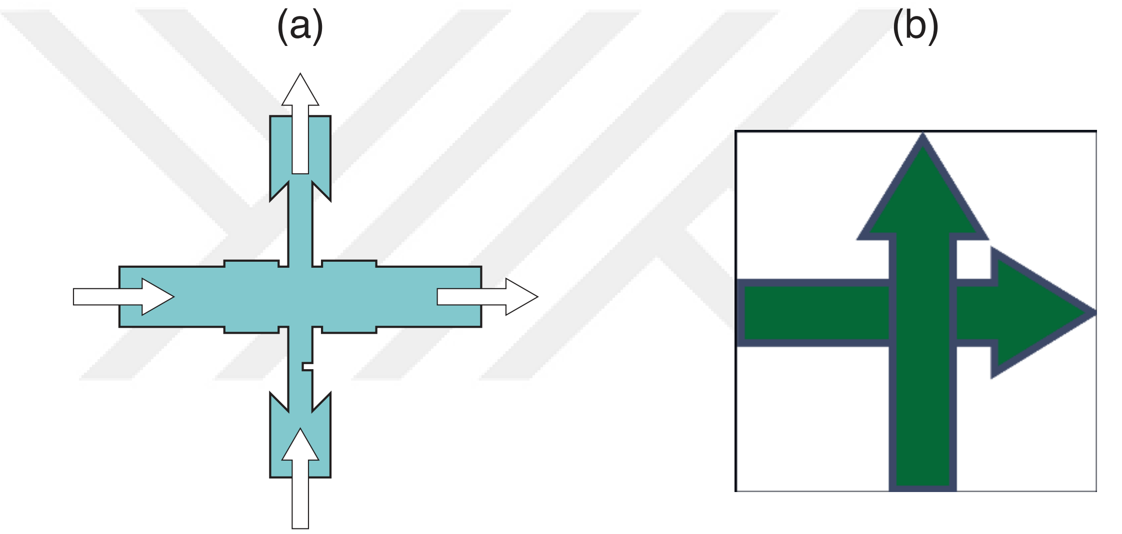

Figure 5.6. The geometry and schematic of the JUNCION UP-RIGTH block

The state equation of the JUNCTION UP-RIGHT is:

$$\begin{cases} i_0(T) = i_2(0) \\ i_1(T) = i_3(0) \\ i_2(T) = 0 \\ i_3(T) = 0 \end{cases} \tag{5.6}$$

JUNCTION UP-LEFT

This block moves two skyrmion from bottom to top and right to left.

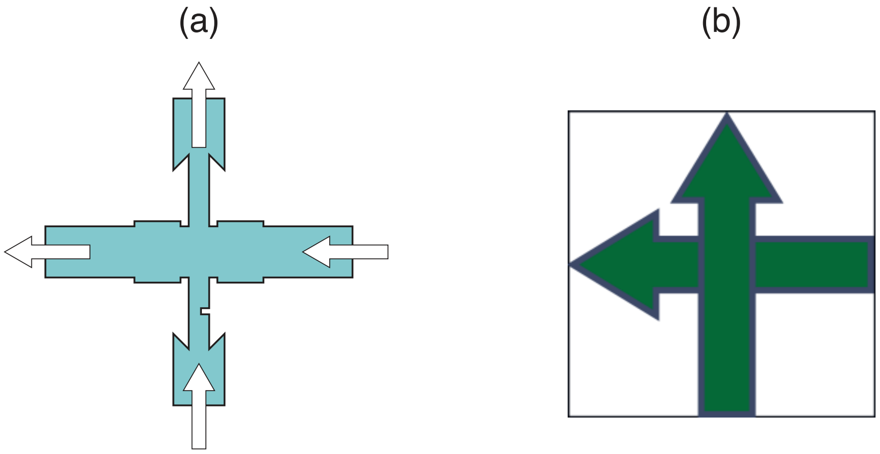

Figure 5.7. The geometry, skyrmion flow and the schematic of the JUNCTION UP-LEFT block.

The state equation for the JUNCTION UP-LEFT block is:

$$\begin{cases} i_0(T) = i_2(0) \\ i_1(T) = 0 \\ i_2(T) = 0 \\ i_3(T) = i_1(0) \end{cases} \tag{5.7}$$

5.4.3 Duplicator

Duplication of skyrmions is an important operation and a DUPLICATOR block is essential for an operational skyrmion logic system as it produces the fan-out operation. A skyrmion is entered from the left channel of the duplicator and two skyrmions emerge from right and bottom channels.

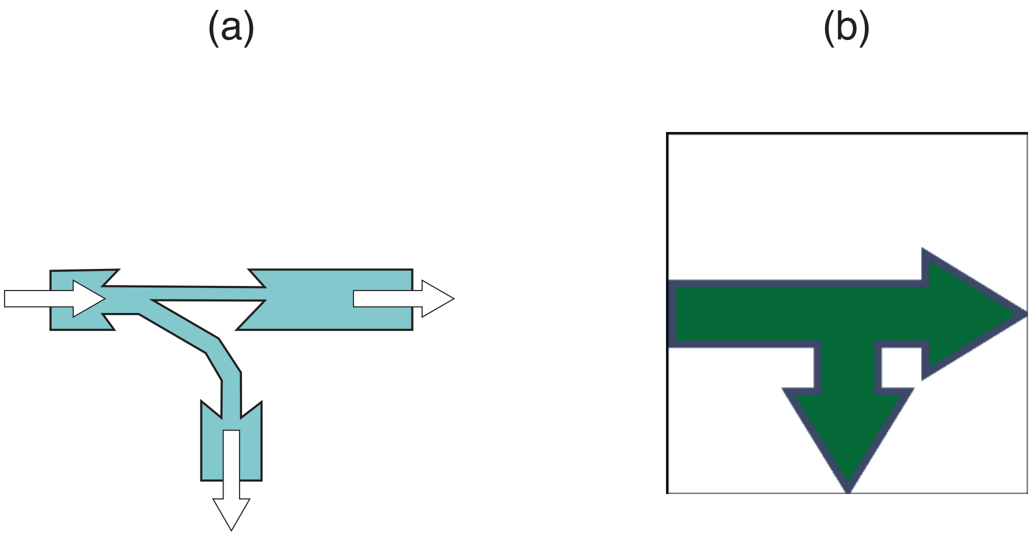

Figure 5.8. The DUPLICATOR geometry, skyrmion flow and schematic

The state equation of the DUPLICATOR block is:

$$\begin{cases} i_0(T) = NULL \\ i_1(T) = \ i_3(0) \\ i_2(T) = i_3(0) \\ i_3(T) = \ 0 \end{cases} \tag{5.8}$$

5.4.4 Transfer

The TRANSFER block is a simple track that a skyrmion moves from left to right in it.

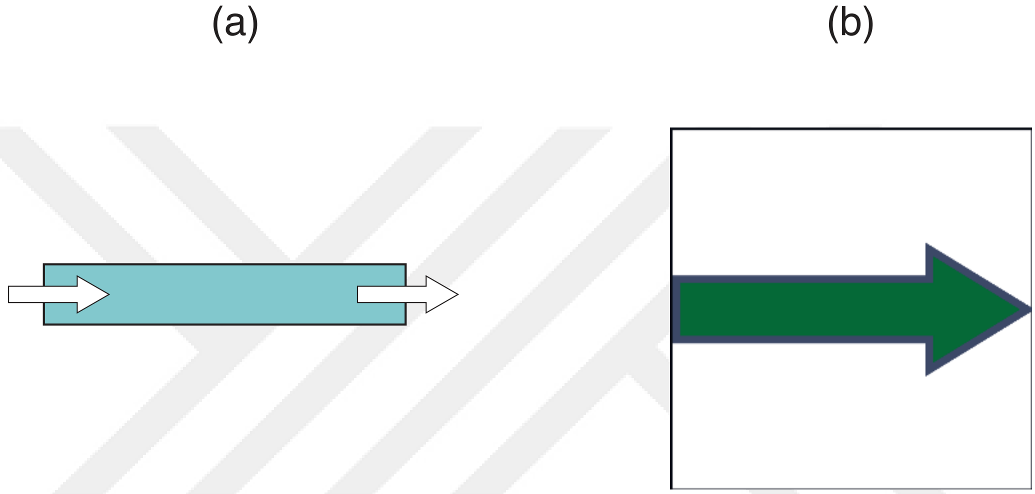

Figure 5.9.The geometry and schematic of the TRANSFER block.

The state equation for the TRANSFER block is:

$$\begin{cases} i_0(T) = 0 \\ i_1(T) = \ i_3(0) \\ i_2(T) = 0 \\ i_3(T) = \ 0 \end{cases} \tag{5.9}$$

5.4.5 Deflectors

LEFT-DOWN DEFLECTOR

The LEFT-DOWN DEFLECTOR moves the skyrmion from left channel to the bottom channel.

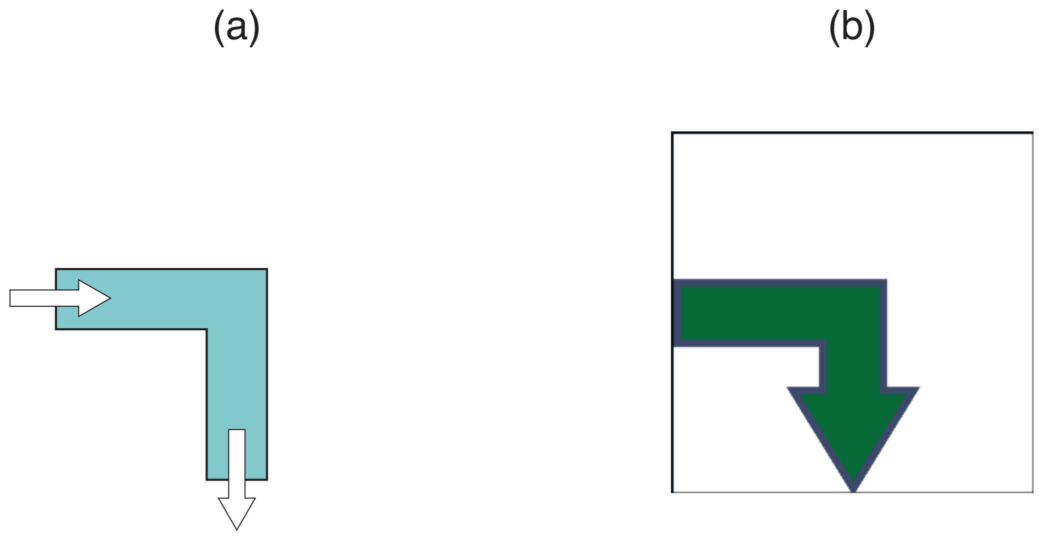

Figure 5.10. Geometry and schematic of the LEFT-DOWN DEFLECTOR block

The state equation of the LEFT-DOWN DEFLECTOR is:

$$\begin{cases} i_0(T) = NULL \\ i_1(T) = NULL \\ i_2(T) = i_3(0) \\ i_3(T) = \ \ 0 \end{cases} \tag{5.10}$$

BOTTOM-LEFT DEFLECTOR

The BOTTOM-LEFT DEFLECTOR moves a skyrmion from the bottom channel to the left channel.

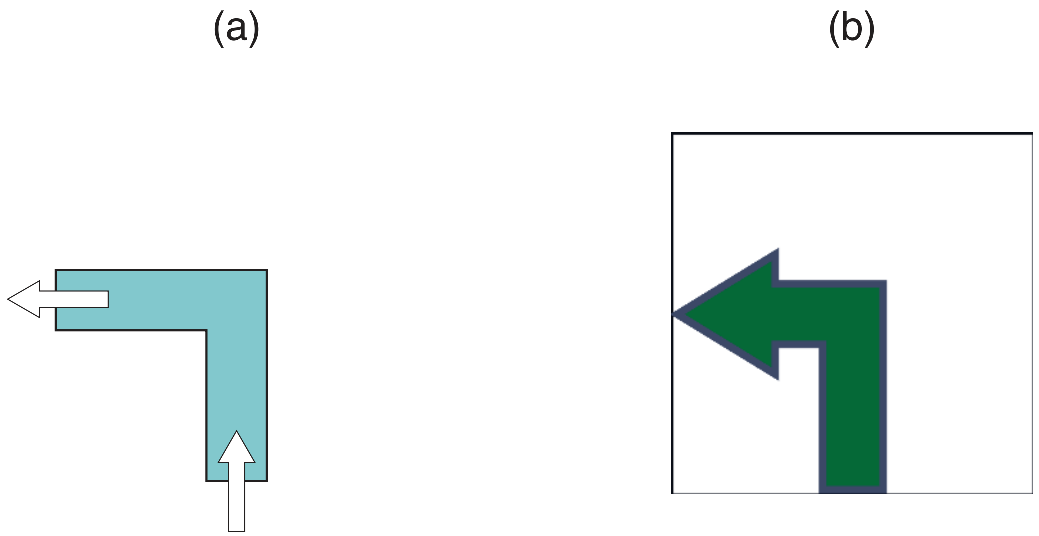

Figure 5.11. The geometry, skyrmion flow and schematics of the bottom-left deflector block

The state equation of the BOTTOM-LEFT DEFLECTOR is:

$$\begin{cases} i_0(T) = NULL \\ i_1(T) = NULL \\ i_2(T) = 0 \\ i_3(T) = i_2(0) \end{cases} \quad (5.11)$$

LOGIC '1'

The LOGIC '1' block outputs a skyrmion at the channel 1.

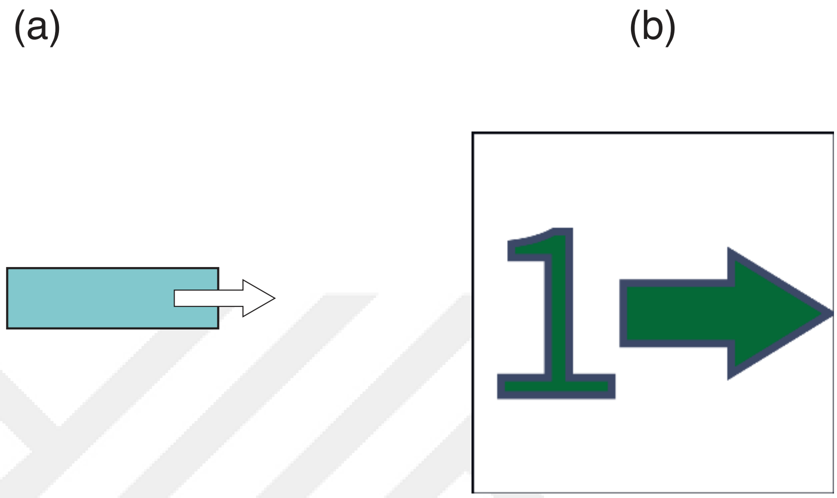

Figure 5.12. The geometry, skyrmion flow and schematic of the LOGIC '1' block.

The state equation of the LOGIC '1' block is:

$$\begin{cases} i_0(T) = NULL \\ i_1(T) = 1 \\ i_2(T) = NULL \\ i_3(T) = NULL \end{cases} \quad (5.12)$$

LOGIC '0'

The LOGIC '0' block's geometry is similar to that of the LOGIC '1' block, The output of the block is no skyrmion. This block could be substituted with an EMPTY block, but for the similarity of the design and the fact that the value of the block can be changed in the runtime, a similar geometry and structure is needed for the LOGIC '1' and LOGIC '0' blocks.

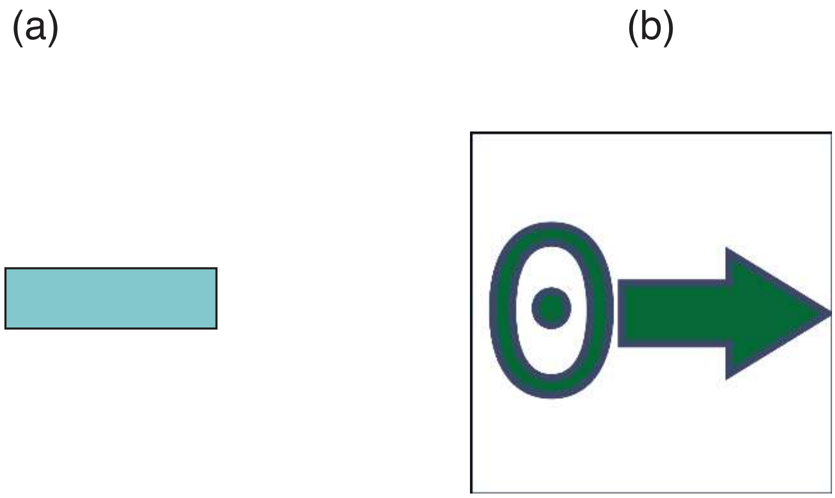

Figure 5.13. The geometry and schematic of the LOGIC '0' block

The state equation of LOGIC '0' is:

$$\begin{cases} i_0(T) = NULL \\ i_1(T) = 0 \\ i_2(T) = NULL \\ i_3(T) = NULL \end{cases} \tag{5.13}$$

5.5 Block Rotation

The blocks and their geometries are designed such that the black box view of the blocks has a 4-fold rotational symmetry, i.e., each block can be rotated 90 degrees and the channels match the neighboring block. It is trivial that not all channels of all blocks are used. Indeed, only the INVERTER-TRANSFER block is making use of all the channels. Rotating a block changes the geometry. Figure 5.14 shows the change in the geometry and schematics of the INVERTER-TRANSFER block under +90° rotation.

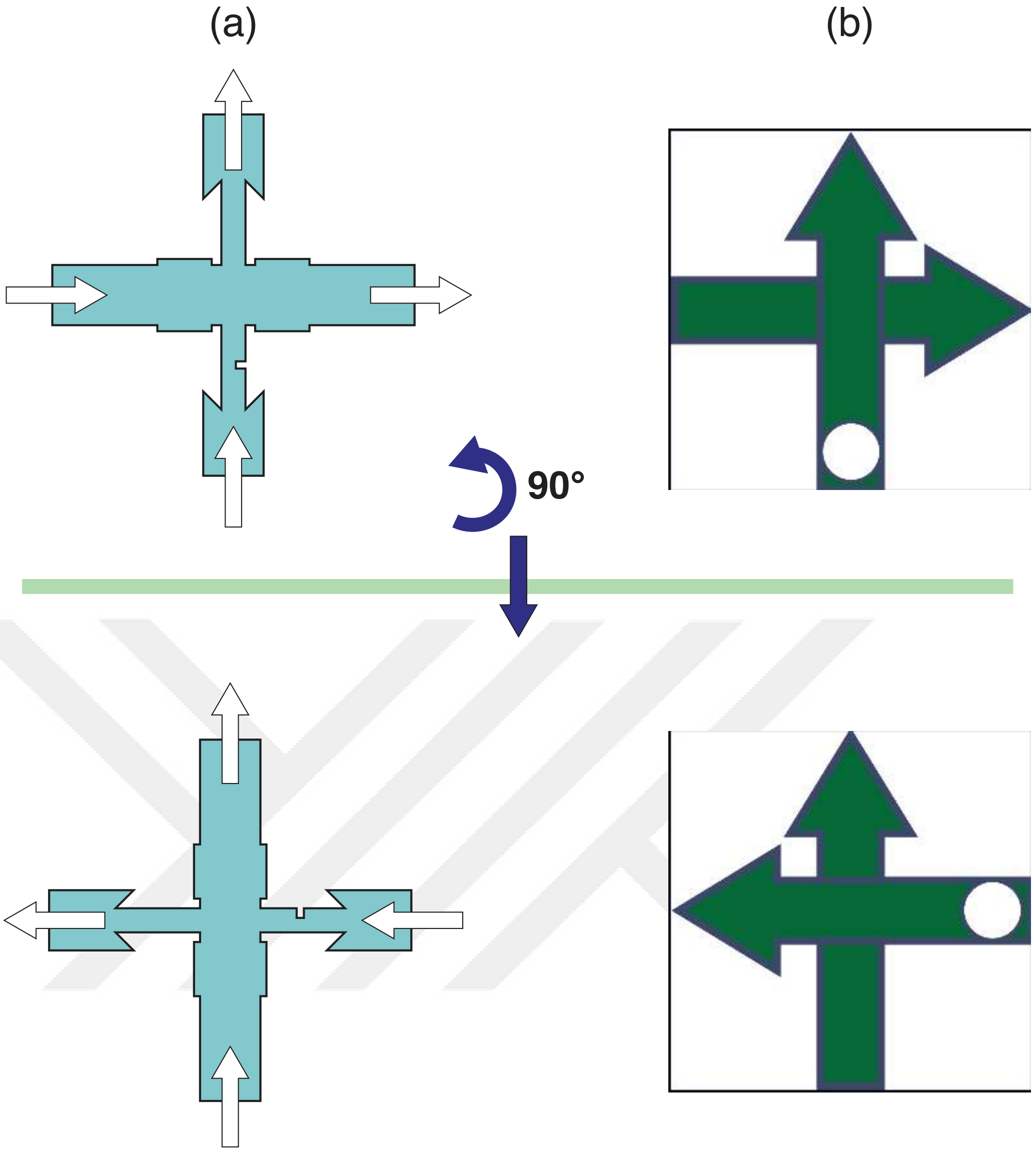

Figure 5.14. +90° rotation of the INVERTER-TRANSFER block

The rotation also changes the state equation of the block by permuting the channels indices:

$$new\ index = \left(old\ index - \frac{rotation}{90}\right) mod\ 4 \tag{5.14}$$

This means that the channel i_0 of a block becomes the channel i_3 of the rotated version since $(0-1) mod\ 4 = 3$. Equation (5.14) is essential to the emulation of the logic system.

Having rotation greatly reduces the redundancy of the system. Since rotation does not provide the flipped version functionality, if a flipped version is necessary, the flipped block needs to be designed and included in the gate set.

5.6 Propagation Scheme

At this stage we investigate the block-propagation scheme. We show how blocks are connected to make a larger geometry and how this geometry translates into the physical model. We also show how applying current density pulses in the tracks translate into the activation of specific blocks. In the next section we see the emulation of the gate of this section.

5.6.1 Matrix Structure

A skyrmion logic gate is constituted of a m×n matrix of blocks where m is the number of rows and n is the number of columns. The NOR gate of Figure 5.1 is a 1×2 matrix of blocks. If we want to have separate blocks for inputs of the NOR gate, the structure becomes a 2×3 matrix as Figure 5.15 shows.

The top part of Figure 5.15 shows the schematics and geometry of the NOR gate with inputs 0, 1. The bottom part shows two snapshots of the micromagnetic simulations of this gate.

The small inset numbers at the bottom-right side of each block show the execution order of the block. Execution order means that the electric current values in the tracks are adjusted such that the block with the specified execution order is enabled.

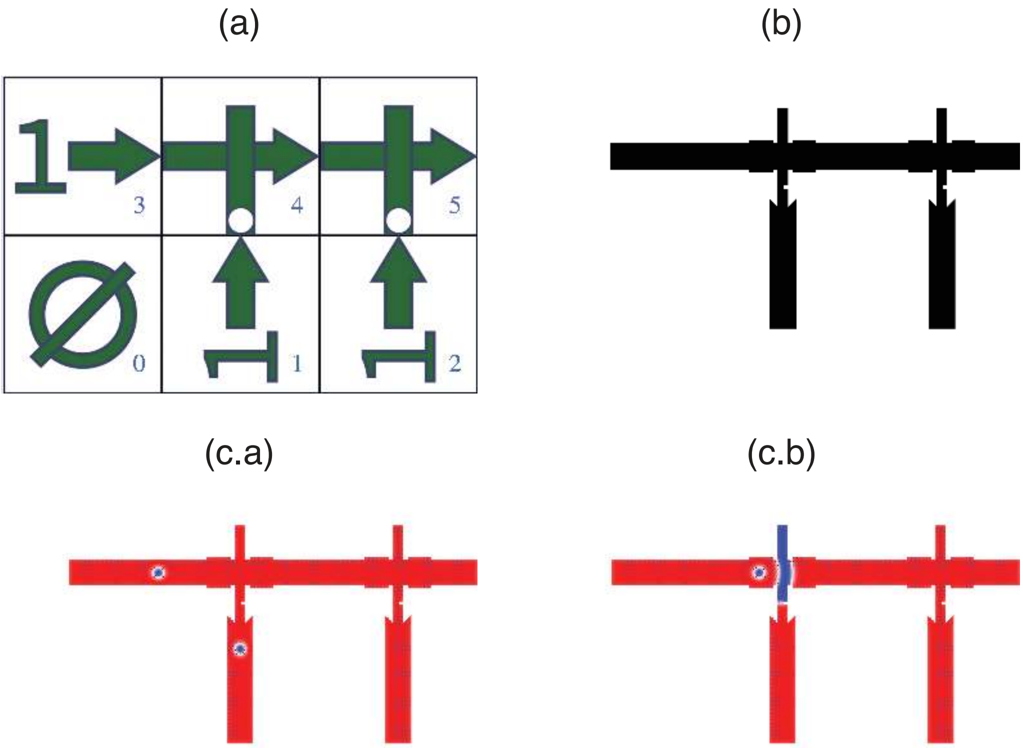

Figure 5.15. The matrix structure of the gate. (a) the schematics of the blocks with their execution order and labels. (b) The geometry of the schematics of part (a). (c.a) the physical model after the execution of the 3rd block. (c.b) the physical model in the middle of the execution of 4th block.

5.6.2 Pulse Activation of Blocks

We have seen that the block abstraction of the gate matrix helps the design and the structure, but still a procedure for activation of individual blocks is not clarified. The block is activated when the spin polarized current flows in its tracks. In reality, the main constituent of the gate is not a block but a track. We can activate each block by sending current pulses in the tracks that is a part of the block. We can consider a matrix of three inverters that produce an OR gate as Figure 5.16 shows.

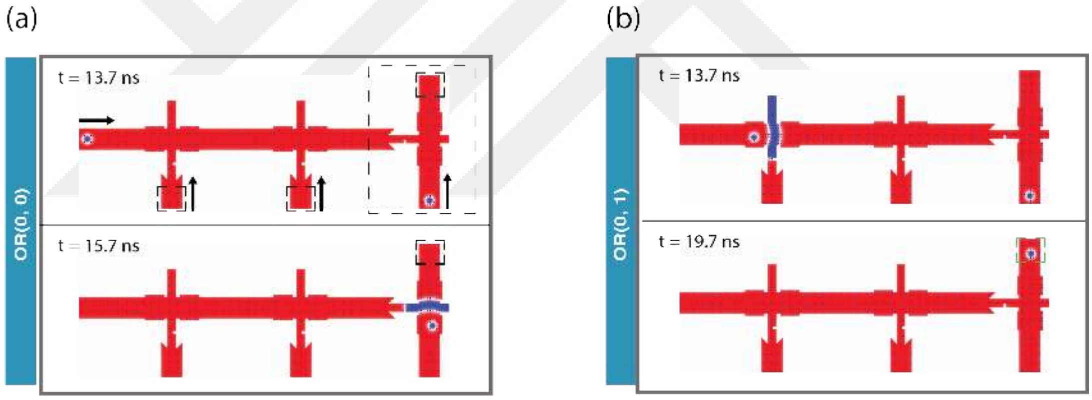

Figure 5.16. The OR gate made from three INVERTER blocks. An OR gate can be made from three inverter gates. (a) the OR gate with two '0' inputs. The inputs and outputs are delineated with dashed small boxes. The larger box shows the rotated INVERTER block. (b) same structure when one of the inputs equals '1'.

The OR gate in Figure 5.16 is composed of three INVERTER blocks concatenated horizontally with the rightmost block rotated -90 degrees. These blocks constitute an integrated geometry with four interconnected tracks:

1- The horizontal track
2- The input1 vertical track
3- The input2 vertical track
4- The output track.

Figure 5.17 shows the current profiles in these tracks over time. The dotted vertical lines delineate the runtime of the three blocks. The operation is started at 0ns by applying the current of 1.4×10^{12} A m^{-2} for 0.46 ns to the input1. Then the transfer stage of this block begins, corresponding to the 0.3×10^{12} A m^{-2} pulse profile for 6 ns in the horizontal track. Then the clearance stage of the first INVERTER block begins, corresponding to applying 3.5×10^{12} A m^{-2} for 0.2 ns in the vertical track of the first INVERTER and the left side notch of the INVERTER. The same pattern happens for the other two INVERTER blocks.

Since the work cycle of a combination of the blocks finishes after the work cycle of every block has ended, a configured combination of pulses for the interconnected tracks can produce the effect of the sequential running of blocks.

We can define a combination of pulse profiles for the arbitrary order of blocks. If we cut the current profiles of Figure 5.17 from the dashed lines, we get three pulse profiles for each block. By reordering these pulse profiles, we can reorder the block execution.

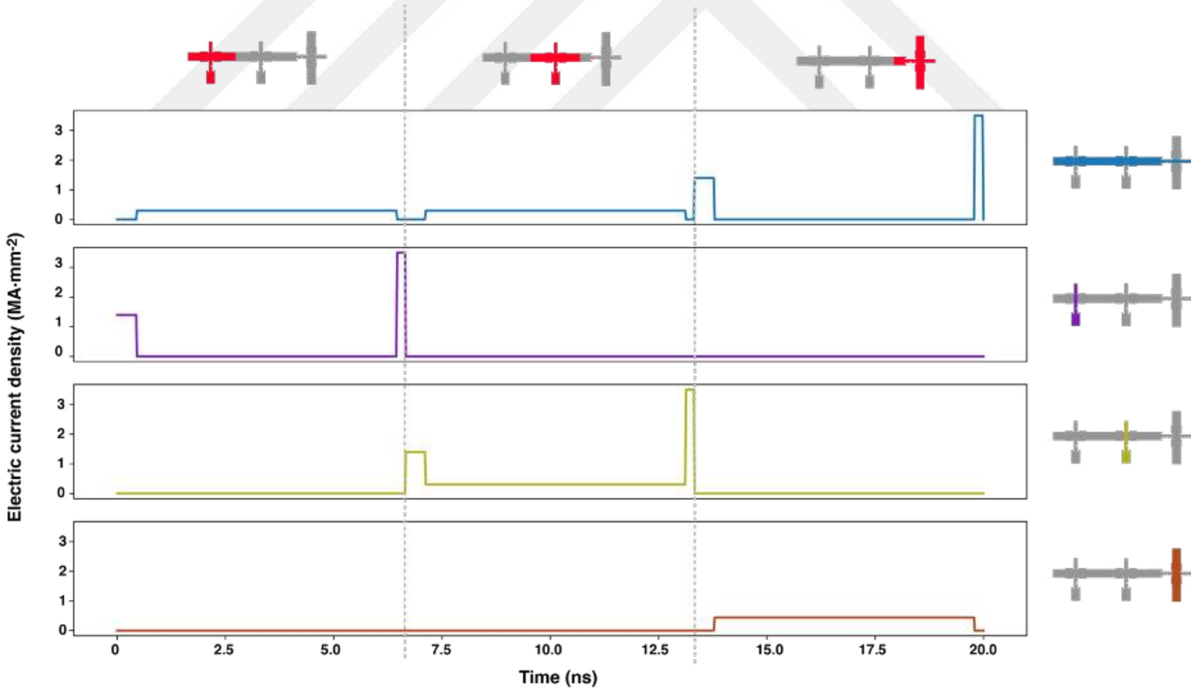

Figure 5.17. Selective current pulses for block-by-block activation. Each row shows a track and the values of current density flowing in that track. the dashed lines delineate the activated blocks. The active tracks and blocks are specified with color.

The computational complexity of the physical models necessitates a system for predicting the behavior of any design. Such a system helps designing the desired gates by predicting the behavior of the matrix of the blocks. In this section we go through the emulation concepts and progress.

5.6.3 State

The state of the matrix of blocks consists of four nodes for each block. These nodes are shared among adjacent blocks. The state of NOR gate of the Figure 5.15 and the propagation of this state is shown in Figure 5.18. Each row of this figure shows the state of the gate after the execution of the specified block.

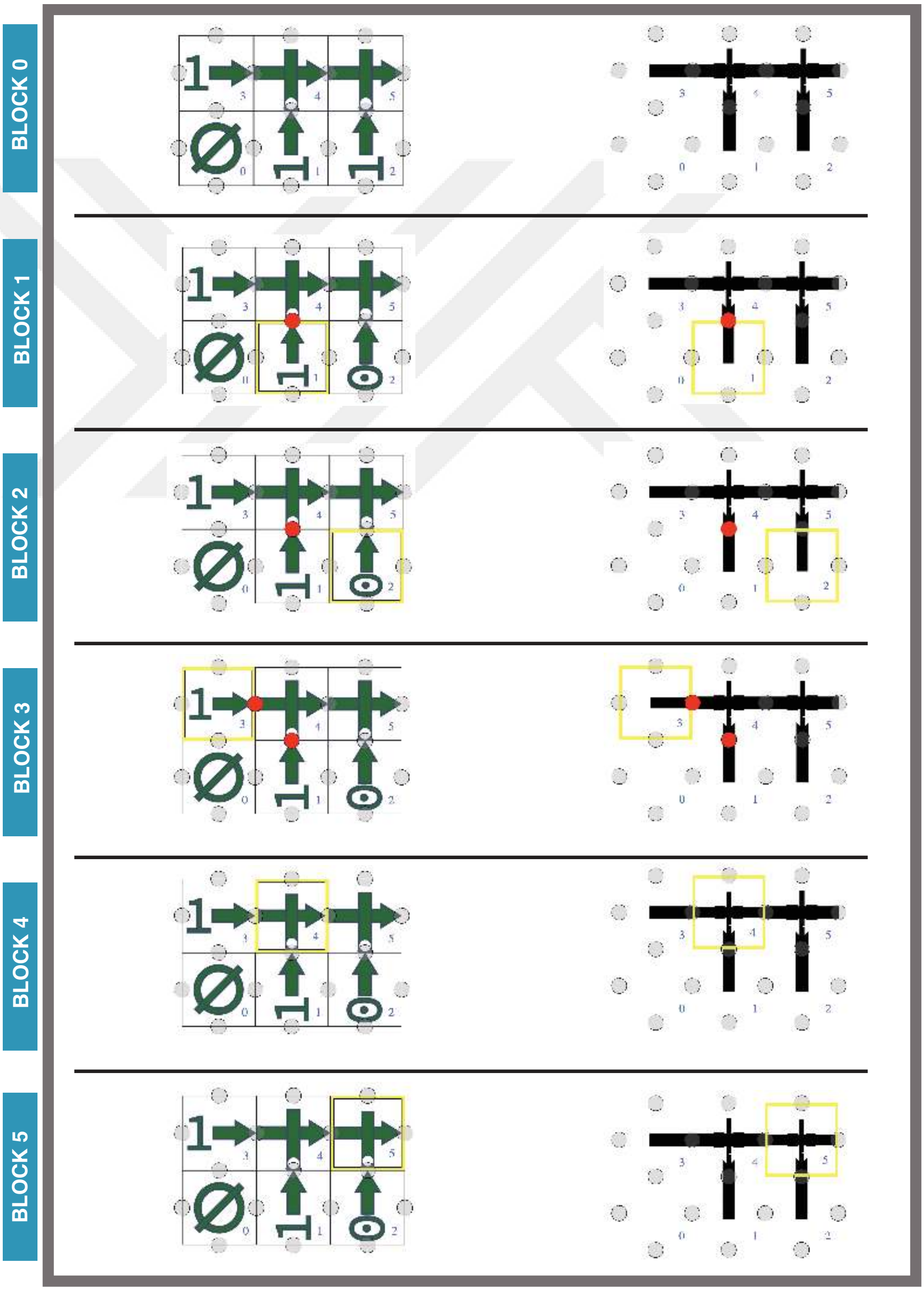

Figure 5.18. The state propagation of the NOR(1,0) gate. Each row shows

the state after the execution of the block for the row. The active block is delineated with a yellow box.

In the Figure 5.18 the schematics of the NOR gate is shown on the left column and the geometry of this gate is shown on the right column. If there is an absence of a skyrmion at a node, its value is '0' and shown with gray (lighter for black and white print). On the other hand, if there is a skyrmion on the node, its value is '1' and it is filled with red (darker for black and white print).

The state propagates according to the equations (5.3) to (5.13) with the modifier equation (5.14) applied to rotated blocks. To better understand the state propagation, each row of Figure 5.18 is explained here:

BLOCK0: This is an empty block and does not provide input-output channels. It does not influence the nodes. Therefore, the nodes remain '0'. Since this block is empty, the execution doesn't have a meaning for this block, and it is not delineated with yellow borders in the figure.

BLOCK1: This block is the left input block. The block is a ONE block and is supposed to have node 1 as '1' after the execution. The block has a rotation of +90 and according to equation (5.14) the node i_0 of the rotated block must have a skyrmion. This skyrmion is produced after the block execution. This skyrmion is shown with the red circle.

BLOCK2: This block is the right input block. The block is a ZERO block and does not produce a skyrmion at the output.

BLOCK3: This block is the probing skyrmion and is a ONE block. It produces a skyrmion at its i_0 node. The produced skyrmion is shown by a red circle at the node.

BLOCK4: The skyrmions from BLOCK1 and BLOCK3 are at the bottom and left inputs of the BLOCK4. This block is an INVERTER block and according to its state equation i.e., the equation (5.3), all the nodes are zero at the end of its execution.

BLOCK5: This block is also an INVERTER block and according to equation (5.3) the nodes of this block must be zero at the end of the execution cycle.

5.7 Emulator and Simulation Maker Software

The Emulator and simulation maker software is developed in Python. It has three main capabilities:

1- Emulation of the behavior of the block matrix (Emulator)

2- Producing the simulation script for the simulation of the matrix of the block (Sim)

3- Emulation of higher abstraction of the system by providing a connection via the netlist and higher-order connections (MiddleSim)

5.7.1 The File Structure

The top-level directory the package consists of the following:

1- The python scripts (simulator.py, emulator.py, helpers.py, imaging.py) These files contain the python package scripts, classes and functions for other functionalities.

2- The resources folder (resources): This folder contains all the platform-specific and peripheral files that are copied with the simulation files. User can change the contents of this folder Based on the platform used or the programs that process the output of the simulation.

3- The blocks set folder (gate_sets): This folder contains the directories of different versions of the block set (versionX/gates/) in each of the versions the block folders reside with the following content:

- the block geometry file (gate.png)
- the current density region files (jx.png)
- the block simulation file (base.txt)
- the block logic file (gate.py).

Each new block added to the block set must have this set of files.

5.7.2 Emulation

The simulator is a Python package and must be used in Python environment. The installed package is imported as follows. The numpy package is necessary to be imported as a dependency of the simulator too. The matplotlib package is required for the display of icons or output signals.

```
from skyrmions.helpers import *
```

```
from skyrmions.simulator import *
from skyrmiions.emulator import *
import numpy as np
import matplotlib.pyplot as plt
print("All packages imported successfully")
```
… All packages imported successfully

Then the available blocks are read into the memory using the read_gates('version_folder') function:

```
blocks = read_gates('version4')
```
… … The names of blocks will be printed here…

To see the schematics of all blocks in the block set we can run use the block.show_icon() method. The figure size and the number of rows and columns :

```
i =1
plt.figure(figsize=(12,10))
for name, block in blocks.items():
    plt.subplot(3,5,i)
    block.show_icon()
    i +=1
```
… …The schematics of blocks will show here

To see the geometries of the blocks we use the block.show() method. The following snippet shows the geometries of blocks:

```
i =1
plt.figure(figsize=(12,10))
for name, block in blocks.items():
    plt.subplot(3,5,i)
    block.show()
    i +=1
```
… …The geometries of blocks will show here

The functionality of a gate can be checked with the run() function of the gate. This function implements the state equation of the gate such as the equations (5.3) to (5.13). For example, the functionality of the INVERTER block can be checked with for the inputs $i_0 = 0$, $i_1 = 0$, $i2 = 0$, and $i_3 = 1$ which indicates a block with a horizontal skyrmion and without a vertical skyrmion and without any rotation:

```
inp = [0, 0, 0, 1] #This is [i_0, i_1, i_2, i_3]
out = blocks['inverter'].run(inp, rot=0)
print(out)
```
… [0, 1, 0, 0]

The out variable contains the evaluated result. For a 90 clockwise rotated gate with the same input to be '1' we need to change the position of the existing skyrmion to i_0 and put the rotation of the gate to

```
23 inp = [1, 0, 0, 0] #This is [i_0, i_1, i_2, i_3]
24 out = blocks['inverter'].run(inp, rot=-1)
25 print(out)
…  [0, 0, 1, 0]
```

To evaluate a matrix of gates we first specify the matrix with the 2D array of blocks, their rotations, and their order of execution:

```
26 block_array = np.array([[blocks['one'], blocks['inverter'],
   blocks['inverter']]])
27 block_rotations = np.array([[0, 0, 0]])
28 simulation_order = np.array([[0, 1, 2]])
…
```

To put this specification into a simulation object we use the *Simulation* class.

```
29 sim = Simulation(block_array,1200)
30 sim.gate_rotations = block_rotations
31 sim.order = simulation_order
32 sim.input_nodes = [(0, 1, 2), (0, 2, 2)]
33 sim.output_nodes = [(0, 2, 1)]
34 sim.show_schematics()
```

…

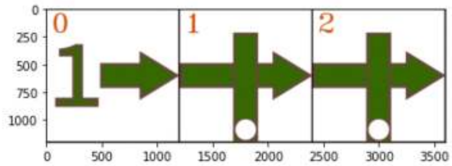

Line 29 puts the block array into a simulation object. The number '1200' is the pixel width of the version of blocks we are using. In lines 30 and 31 the rotations and orders for each block are inserted into the simulation object. In the lines 32 and 33 the input and output nodes of the structure are defined. Each node is determined by a 3 tuple of (row_number, col_number, channel_number). Line 32 defines two inputs for the middle INVERTER block (row_number=0, column_number=1, channel_number=2) and right INVERTER block (row_number=0, column_number=1, channel_number=2). Line 33 defines the channel 1 of the right INVERTER block as the output.

Using these definitions for the inputs and outputs, we get the truth table of the structure using the truth_table() function.

```
35 print('ab  o')
36 print('=======')
37 sim.truth_table()
```

```
…   ab o
    =======
    00 1
    01 0
    10 0
    11 0
```

This is the truth table for the NOR gate. Thus, by running the *truth_table()* function we check the functionality of our designed device. Checking the functionality at this stage has a much less computational cost than simulating the structure with Mumax3. Thus, before continuing to do the physical simulation we do this step to ensure that the design is supposed to produce the intended results.

5.7.3 Automated Simulation Script

The Mumax3 simulation script for matrix structures can get very complicated and large because of the large number of current density regions and the block cascading and rotation. Thus, an automated simulation script producing function is a part of the library.

To have a valid simulation, we need to specify the inputs for the input nodes. We do this by adding input blocks.

```
block_array = np.array(
[[blocks['one'], blocks['inverter'], blocks['inverter']],
 [blocks['empty'], blocks['zero'], blocks['one']]])
block_rotations = np.array([[0, 0, 0],
                            [0, 1, 1]])
simulation_order = np.array([[3, 4, 5],
                             [0, 1, 2]])
sim = Simulation(block_array,1200)
sim.gate_rotations = block_rotations
sim.order = simulation_order
sim.show_schematics()
```

…

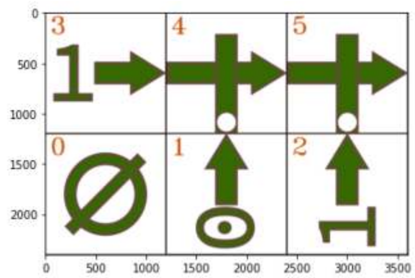

It is also possible to check the functionality of this structure before the simulation by *propagate()* and *put_snapshot(executed_block_number)* function.

```
sim.propagate()
sim.put_snapshot(2)
```

...

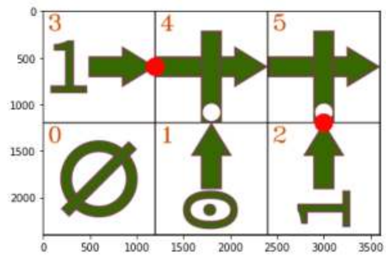

The red circles denote the existence of a skyrmion at the node. The propagate runs all the blocks to the last. Thus, by visualizing the final state of the simulation, we can see the result of the emulation. We can do this by *put_state()* function that visualizes the current state of the structure.

```
sim.put_state()
```

...

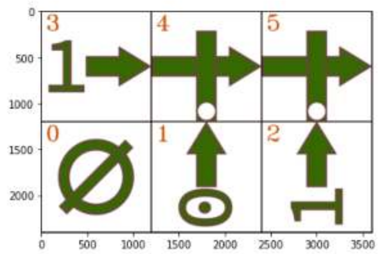

Now that the expected result of the simulation matches the expectation, the simulation script can be produced.

```
sim.save_simulation('NOR0_1')
```

This produces a folder named NOR0_1 containing the main simulation file (NOR0_1.mx3), the geometry file (gate.png), and the region files (jx.png: where x is the region number). Depending on user-defined contents of the *resources* folder of the package, other files such as the files needed to run the simulation on a specific platform, or the files needed to put the results in a movie can also exist in this folder.

5.7.4 Emulation for Larger Structures

Although the emulator makes the test design of structures much easier, larger structure test and debugging might also be time consuming without an easier design tool. Moreover, reusing the already designed structures such as AND, OR, NOR, XOR, XNOR in the emulation is also a desirable option to have. This feature is implemented via the MiddleSim application class. The output of the full adder gate implemented by the MiddleSim class is shown in Figure 5.19. The APIs of the MiddleSim class are similar to the Sim class, except that the Mumax3 simulation file cannot be produced from the MiddleSim class.

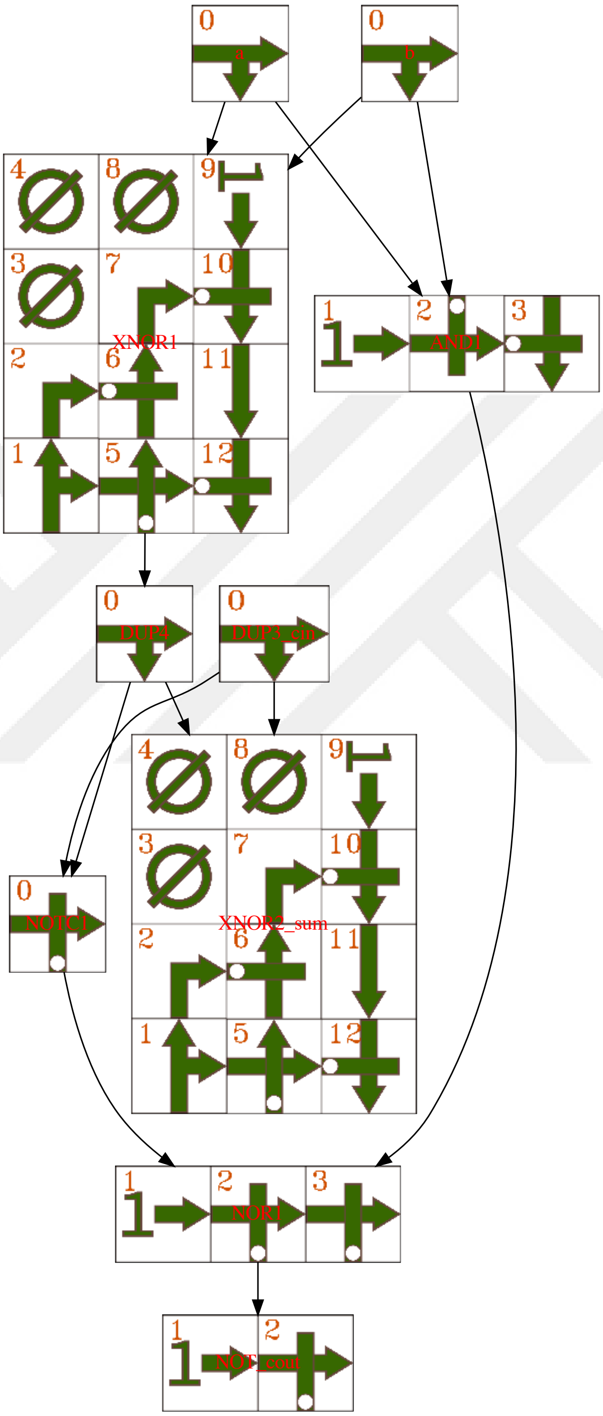

Figure 5.19. The MiddleSim implementation of a full adder gate. The arrows show the skyrmion route connection between the gates. The inputs and outputs of each gate are specified in the code and the arrows show the connection to the inputs from the outputs.

5.7.5 Skyrmion Gate Structure Design Recipe

The gist of the design and simulation library is mostly covered up to here. We can use this library for the efficient design and simulation of skyrmion logic gates. For this aim, the following steps can be taken:

1- Write the function in terms of the conventional gates we have designed by blocks. Such as AND, OR, NAND, NOR, XNOR, XOR, etc.,

2- Build this structure as a MiddleSim class object.

3- Get the truth table of the MiddleSim object and compare it to the intended truth table.

4- Make a Sim object from the MiddleSim design and get the truth table of the sim object and compare it to the intended truth table.

5- Add the specific inputs and produce the Mumax3 simulation files and run them to make sure that the simulation results match the Sim object results.

Step 5 is the most time-consuming step of all. Thus, deliberation for the first 4 steps is essential to reach the correct result at stage 5.

5.8 Gate Library

The Boolean logic system consists of several main gates like AND, NAND, OR, NOR, NOT, XOR, and XNOR. Since these gates are central to the Boolean logic systems. Their structure based on the block set and their simulation results in the form of movies is also provided into the accompanying materials to this thesis.

5.9 Full Adder

Full adder is an essential part of a CPU. The *MiddleSim* structure of a full adder is shown in Figure 5.19. The Sim Object structure of it is shown in Figure 5.20. The design Figure 5.20 can be changed in terms of the routing blocks if one wishes.

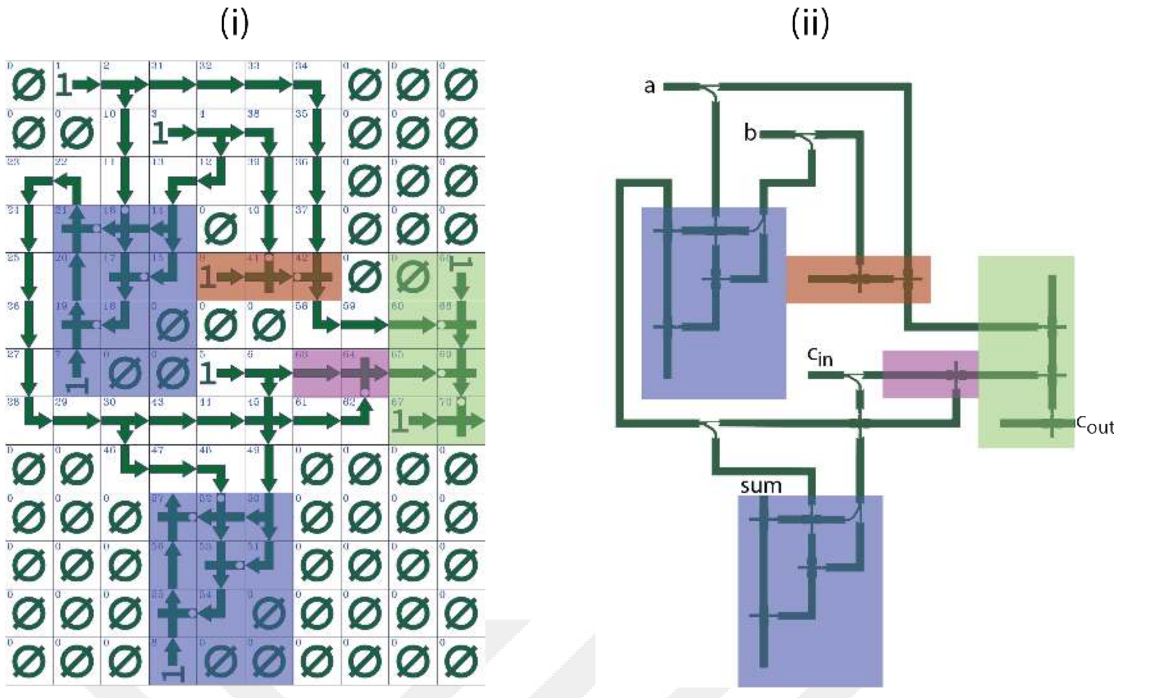

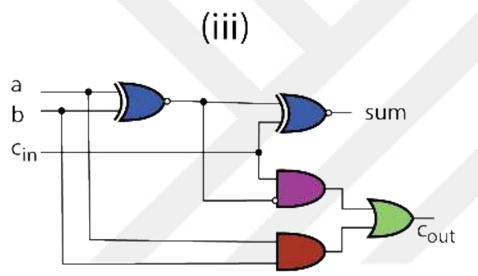

c_{in}	a	b	c_{out}	sum
0	0	0	0	0
0	0	1	0	1
0	1	0	0	1
0	1	1	1	0
1	0	0	0	1
1	0	1	1	0
1	1	0	1	0
1	1	1	1	1

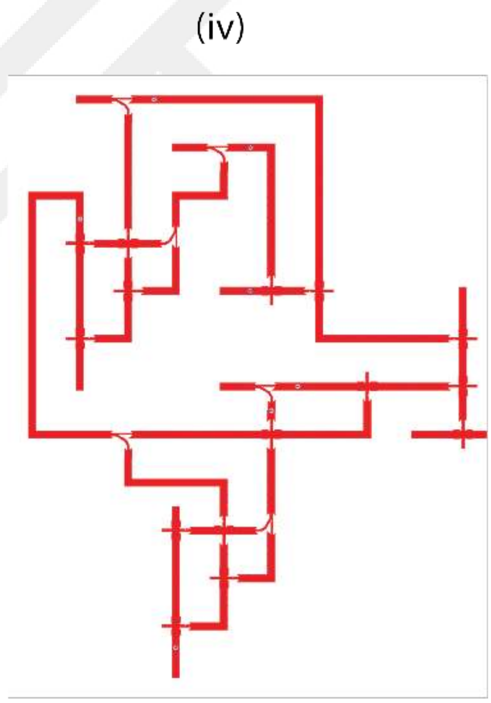

Figure 5.20. The full adder. (i) the emulator view of the full adder. Logic gates are delineated with colored blocks; blue: XNOR, brown: AND, green: OR, magenta: INVERTER. (ii) The physical geometry with the same blocks, (iii) the digital circuit representation with the same color coding and the truth table (iv) the snapshot of the magnetization profile at the end of the execution cycle of block 21.

5.10 Summary

This chapter consists of the description of the skyrmion logic system, block model, simulation, and emulation of the skyrmion logic system.

The universality of the INVERTER block with two input was first proved mathematically. Universality is an essential aspect of the core logic block of any logic system capable of producing arbitrary logic. Thus, proving that INVERTER block is universal, proves that an arbitrary logic function can be made from INVERTER blocks. Non-logic blocks such as JUNCTION, TRANSFER, DUPLICATOR, etc., are also essential part of the system as they provide fan-in and fan-out for the INVERTER blocks.

A general abstraction of a block is necessary for emulating the behavior of the system. This general model as introduced in section 5.3 is a square block with 4 channels that can be used as input/output. Then, individual blocks and their state equations are introduced in section 5.4. The rotational symmetry of the block model allows for 90-degree rotations of each block that leads into 4 different state equation for each block.

Concatenating the blocks produces a system with tracks for guiding skyrmions. The timing of the application spin-polarized electric current in these tracks makes the execution of individual blocks possible. This propagation scheme is explained in 5.6.

Executing individual blocks enables us to have a higher-level abstraction of the logic where the existence of a skyrmion at a channel means logic '1' and the absence of the skyrmion means logic '0'. These enable us to emulate the behavior of a skyrmion logic matrix. section 5.6 also explains the emulation procedure. The rest of the chapter is devoted to the software library for facilitating the emulation, producing complex simulation scripts and the instructions for extending the software library. Section 5.9 also introduces the full adder as one of the most essential functions of digital logic. Implementing the full adder using skyrmion logic is crucial to show that the system can go beyond the simple logic gates and do arithmetic operations.

Chapter 6

CONCLUSION

6.1 Discussion

This work is about the skyrmionics logic system. The existing proposals were not at system level, and they had issues of non-universality and non-scalability. This was largely because most of skyrmionics research was centered around the physics aspects of skyrmions. Furthermore, the software tools for the modular design of skyrmion circuits were missing. This work first finds a way to modularize the skyrmion logic circuit system. This was achieved by producing a universal INVERTER gate, designing routing and fan-out elements, and then putting them into compatible geometric blocks. This opened a system perspective to the skyrmionics logic, that was missing before.

The design and characterization of these skyrmionics devices requires a systematic approach to the simulation process. Because of the minimalist approach of micromagnetic simulation software, a package for making systematic simulations and its data processing was needed. This software was developed in this work.

Even with the compatible blocks that are confirmed by simulations to work individually, putting these blocks together in arbitrary manners and testing the outcome without doing the physical simulation is not only convenient but crucial for the design process of skyrmion logic. Moreover, producing the simulation scripts and files that are executable by micromagnetic software is challenging without an automated tool as the number of files and the length of the simulation scripts get unwieldly. This software is designed in this work using Python programming language. The Python package for these tasks can be installed using the following command:

```
pip install skyrmions
```

Skyrmionics has gained an intensive attention in the recent years because of its benefits such as ultralow power consumption, non-volatility of signals, the potential for in-memory computation architectures, the potential to combine different schemes of computations such as reservoir computation and Boolean computation.

This work presents skyrmionics as a serious candidate for technological use. This is done by proving that a system view for skyrmionics is possible. Moreover, it makes the skyrmionics system design accessible to the computer science or engineering researchers by providing tools that do not need scientific knowledge of skyrmions or magnetism.

The work of this thesis lies in the scope of Boolean logic. Boolean logic has been the dominant computation scheme. The modern computers are founded on the Boolean logic and von-Neumann architecture. Because of the ultra-low power and non-volatility of skyrmions, artificial intelligence can benefit from more analog/digital computational schemes. The role of skyrmionics in neuromorphic, memristive or reservoir computing is also gaining attention. While the focus of this work is on Boolean logic design, the blocksets can also be extended to include these types of computational schemes.

Skyrmionics while having many advantages still has several unsolved questions to answer. The most important step is the experimental demonstration of logic operations. While the skyrmion hosting materials, interactions with geometry, and the movements induced by spin-polarize currents are shown experimentally, more of experimental evidence is needed to reach the realization of the logic system proposed by this thesis.

It would also benefit to look at the skyrmionics and specially this work in the light of the technology readiness level (TRL). TRL is a 9-level scale for estimating the technology maturity and enables assessing the readiness of schemes for technological use. TRL1 is the observation and report of basic principles of a technology. The studies before this thesis lie in this level as the basic principles of skyrmionics logics in terms of individual logic gates are shown. TRL2 is the technology concept and application formulation. This thesis pushes the skyrmionics logic into TRL2 as the modular design and design tools of this thesis offer. To push the skyrmionics into the next level i.e., TRL3, the experimental proof of concept is needed. The experimental proof of concept will be the next step to this study.

6.2 Future Works

This work set up a ground for future skyrmionics works. The future works on this subject will be extensive and needs more innovation. Here the possible future work is divided into three main categories.

1) The software aspect of this work can be developed into more mature and extensive packages.

- The phase diagram and simulation arrangement part of the software can be extended to have more capabilities. The current features of the software are the 2-parameter sweeps, customized function application on the results, batch simulation running, and tabular data processing. These features can be extended to have 3-parameter sweeps too.
- The tools for VHDL/Verilog RTL schematics with skyrmion logic device layouts will be a required and valuable extension for this package. An interpreter of HDL to the blockset of skyrmion logic is essential to reach this goal.
- The Mumax3 micromagnetic software allows for 256 regions as it uses 8-bits to define the region numbers. This limits the size of the designs of the package that could be simulated. This number must be increased. This increase is needed by refactoring the Mumax3/Cuda interface in Mumax3 source code.

2) Library of skyrmion devices and their parametric studies:

- Although the material parameters, current values, timings, the geometries to demonstrate the skyrmion logic system are presented in this thesis, the research can be complemented with more extensive focus on current-bias, material parameters, material noise effects, finite temperature effects, geometric changes, external field, and gate timing and bandwidth.

3) Studies of skyrmion devices with insulating magnetic thin films and 2D interfaces:

- Eliminating Joule heating in realistic material models (finite but very high resistance, band structure effects that cause second or higher harmonic excitations of spin oscillations with current)
- Designing and testing blocks and gates for other types of materials such as FGT ($Fe_xGe_yTe_z$)/Pt, FGT (magnetic)/Bi_2Se_3 (doped, semi-metallic), YIG/Pt, YIG ($Y_3Fe_5O_{12}$) or $Tm_3Fe_5O_{12}$ (magnetic)/Bi_2Se_3 (doped, semi-metallic)

BIBLIOGRAPHY

1. Kim, N.S., et al., *Leakage current: Moore's law meets static power*. computer, 2003. **36**(12): p. 68-75.
2. Thompson, S.E. and S. Parthasarathy, *Moore's law: the future of Si microelectronics*. Materials today, 2006. **9**(6): p. 20-25.
3. Wolf, S., et al., *Spintronics: a spin-based electronics vision for the future*. Science, 2001. **294**(5546): p. 1488-1495.
4. Diény, B., *Giant magnetoresistance in spin-valve multilayers*. Journal of Magnetism and Magnetic Materials, 1994. **136**(3): p. 335-359.
5. Fert, A., V. Cros, and J. Sampaio, *Skyrmions on the track*. Nature nanotechnology, 2013. **8**(3): p. 152-156.
6. Chen, T.C. and H. Chang, *Magnetic bubble memory and logic*, in *Advances in computers*. 1978, Elsevier. p. 223-282.
7. O'Dell, T., *Magnetic bubble domain devices*. Reports on Progress in Physics, 1986. **49**(5): p. 589.
8. Bobeck, A.H., P.I. Bonyhard, and J.E. Geusic, *Magnetic bubbles—An emerging new memory technology*. Proceedings of the IEEE, 1975. **63**(8): p. 1176-1195.
9. Bogdanov, A. and D. Yablonskii, *Thermodynamically stable" vortices" in magnetically ordered crystals. The mixed state of magnets*. Zh. Eksp. Teor. Fiz, 1989. **95**: p. 182.
10. Bogdanov, A. and U. Rößler, *Chiral symmetry breaking in magnetic thin films and multilayers*. Physical review letters, 2001. **87**(3): p. 037203.
11. Rößler, U., A. Bogdanov, and C. Pfleiderer, *Spontaneous skyrmion ground states in magnetic metals*. Nature, 2006. **442**(7104): p. 797.
12. Mühlbauer, S., et al., *Skyrmion lattice in a chiral magnet*. Science, 2009. **323**(5916): p. 915-919.
13. Yu, X., et al., *Real-space observation of a two-dimensional skyrmion crystal*. Nature, 2010. **465**(7300): p. 901.
14. Woo, S., et al., *Observation of room-temperature magnetic skyrmions and their current-driven dynamics in ultrathin metallic ferromagnets*. Nature materials, 2016. **15**(5): p. 501.
15. Birch, M., et al., *Real-space imaging of confined magnetic skyrmion tubes*. Nature communications, 2020. **11**(1): p. 1726.
16. Sampaio, J., et al., *Nucleation, stability and current-induced motion of isolated magnetic skyrmions in nanostructures*. Nature nanotechnology, 2013. **8**(11): p. 839.
17. Berger, L., *Prediction of a domain-drag effect in uniaxial, non-compensated, ferromagnetic metals*. Journal of Physics and Chemistry of Solids, 1974. **35**(8): p. 947-956.
18. Hung, C.Y. and L. Berger, *Exchange forces between domain wall and electric current in permalloy films of variable thickness*. Journal of applied physics, 1988. **63**(8): p. 4276-4278.
19. Salhi, E. and L. Berger, *Current‐induced displacements of Bloch walls in Ni‐Fe films of thickness 120–740 nm*. Journal of applied physics, 1994. **76**(8): p. 4787-4792.
20. Slonczewski, J.C., *Current-driven excitation of magnetic multilayers*. Journal of magnetism and magnetic materials, 1996. **159**(1-2): p. L1-L7.
21. Beach, G.S., et al., *Dynamics of field-driven domain-wall propagation in ferromagnetic nanowires*. Nature materials, 2005. **4**(10): p. 741-744.
22. Ono, T., et al., *Propagation of a magnetic domain wall in a submicrometer*

magnetic wire. Science, 1999. **284**(5413): p. 468-470.

23. Nakatani, Y., A. Thiaville, and J. Miltat, *Faster magnetic walls in rough wires*. Nature materials, 2003. **2**(8): p. 521-523.
24. Vernier, N., et al., *Domain wall propagation in magnetic nanowires by spin-polarized current injection*. EPL, 2004. **65**(4): p. 526.
25. Tsoi, M., R. Fontana, and S. Parkin, *Magnetic domain wall motion triggered by an electric current*. Applied physics letters, 2003. **83**(13): p. 2617-2619.
26. Cowburn, R., et al., *Domain wall injection and propagation in planar Permalloy nanowires*. Journal of applied physics, 2002. **91**(10): p. 6949-6951.
27. Petit, D., et al., *Domain wall pinning and potential landscapes created by constrictions and protrusions in ferromagnetic nanowires*. Journal of Applied Physics, 2008. **103**(11): p. 114307.
28. Marrows, C., *Spin-polarised currents and magnetic domain walls*. Advances in Physics, 2005. **54**(8): p. 585-713.
29. Kläui, M., et al., *Controlled and reproducible domain wall displacement by current pulses injected into ferromagnetic ring structures*. Physical review letters, 2005. **94**(10): p. 106601.
30. Ravelosona, D., et al., *Threshold currents to move domain walls in films with perpendicular anisotropy*. Applied physics letters, 2007. **90**(7): p. 072508.
31. Thiaville, A., et al., *Micromagnetic understanding of current-driven domain wall motion in patterned nanowires*. Europhysics Letters, 2005. **69**(6): p. 990.
32. Fukami, S., et al., *Micromagnetic analysis of current driven domain wall motion in nanostrips with perpendicular magnetic anisotropy*. Journal of Applied Physics, 2008. **103**(7): p. 07E718.
33. Thiaville, A., et al., *Dynamics of Dzyaloshinskii domain walls in ultrathin magnetic films*. Europhysics Letters, 2012. **100**(5): p. 57002.
34. Yoshimura, Y., et al., *Soliton-like magnetic domain wall motion induced by the interfacial Dzyaloshinskii–Moriya interaction*. Nature Physics, 2016. **12**(2): p. 157-161.
35. Emori, S., et al., *Current-driven dynamics of chiral ferromagnetic domain walls*. Nature materials, 2013. **12**(7): p. 611-616.
36. Allwood, D., et al., *Submicrometer ferromagnetic NOT gate and shift register*. Science, 2002. **296**(5575): p. 2003-2006.
37. Allwood, D.A., et al., *Magnetic domain-wall logic*. Science, 2005. **309**(5741): p. 1688-1692.
38. Parkin, S.S., M. Hayashi, and L. Thomas, *Magnetic domain-wall racetrack memory*. Science, 2008. **320**(5873): p. 190-194.
39. Franken, J., H. Swagten, and B. Koopmans, *Shift registers based on magnetic domain wall ratchets with perpendicular anisotropy*. Nature nanotechnology, 2012. **7**(8): p. 499-503.
40. Luo, Z., et al., *Current-driven magnetic domain-wall logic*. Nature, 2020. **579**(7798): p. 214-218.
41. Thiele, A., *Steady-state motion of magnetic domains*. Physical Review Letters, 1973. **30**(6): p. 230.
42. Bogdanov, A. and A. Hubert, *Thermodynamically stable magnetic vortex states in magnetic crystals*. Journal of magnetism and magnetic materials, 1994. **138**(3): p. 255-269.
43. Heinze, S., et al., *Spontaneous atomic-scale magnetic skyrmion lattice in two dimensions*. Nature Physics, 2011. **7**(9): p. 713.
44. Yu, X., et al., *Near room-temperature formation of a skyrmion crystal in thin-films of the helimagnet FeGe*. Nature materials, 2011. **10**(2): p. 106-109.
45. Münzer, W., et al., *Skyrmion lattice in the doped semiconductor Fe 1− x Co x*

Si. Physical Review B, 2010. **81**(4): p. 041203.

46. Yu, X., et al., *Skyrmion flow near room temperature in an ultralow current density*. Nature communications, 2012. **3**: p. 988.
47. Schulz, T., et al., *Emergent electrodynamics of skyrmions in a chiral magnet*. Nature Physics, 2012. **8**(4): p. 301-304.
48. Iwasaki, J., M. Mochizuki, and N. Nagaosa, *Universal current-velocity relation of skyrmion motion in chiral magnets*. Nature communications, 2013. **4**(1): p. 1463.
49. Tchoe, Y. and J.H. Han, *Skyrmion generation by current*. Physical Review B, 2012. **85**(17): p. 174416.
50. Woo, S., et al., *Observation of room temperature magnetic skyrmions and their current-driven dynamics in ultrathin Co films*. arXiv preprint arXiv:1502.07376.
51. Yu, X., et al., *Current-induced nucleation and annihilation of magnetic skyrmions at room temperature in a chiral magnet*. Advanced Materials, 2017. **29**(21): p. 1606178.
52. Schott, M., et al., *The skyrmion switch: turning magnetic skyrmion bubbles on and off with an electric field*. Nano letters, 2017. **17**(5): p. 3006-3012.
53. Hsu, P.-J., et al., *Electric-field-driven switching of individual magnetic skyrmions*. Nature nanotechnology, 2017. **12**(2): p. 123-126.
54. Yu, G., et al., *Room-temperature creation and spin–orbit torque manipulation of skyrmions in thin films with engineered asymmetry*. Nano letters, 2016. **16**(3): p. 1981-1988.
55. Hrabec, A., et al., *Current-induced skyrmion generation and dynamics in symmetric bilayers*. Nat Commun, 2017. **8**: p. 15765.
56. Büttner, F., et al., *Dynamics and inertia of skyrmionic spin structures*. Nature Physics, 2015. **11**(3): p. 225.
57. Iwasaki, J., M. Mochizuki, and N. Nagaosa, *Current-induced skyrmion dynamics in constricted geometries*. Nature nanotechnology, 2013. **8**(10): p. 742.
58. Koshibae, W. and N. Nagaosa, *Creation of skyrmions and antiskyrmions by local heating*. Nature communications, 2014. **5**(1): p. 1-11.
59. Everschor-Sitte, K., et al., *Skyrmion production on demand by homogeneous DC currents*. New Journal of Physics, 2017. **19**(9): p. 092001.
60. Legrand, W., et al., *Room-temperature current-induced generation and motion of sub-100 nm skyrmions*. Nano letters, 2017. **17**(4): p. 2703-2712.
61. Zhang, X., Y. Zhou, and M. Ezawa, *Antiferromagnetic skyrmion: stability, creation and manipulation*. Scientific reports, 2016. **6**(1): p. 24795.
62. Caretta, L., et al., *Fast current-driven domain walls and small skyrmions in a compensated ferrimagnet*. Nature nanotechnology, 2018. **13**(12): p. 1154-1160.
63. Soumyanarayanan, A., et al., *Tunable room-temperature magnetic skyrmions in Ir/Fe/Co/Pt multilayers*. Nature materials, 2017. **16**(9): p. 898-904.
64. Jiang, W., et al., *Direct observation of the skyrmion Hall effect*. Nature Physics, 2017. **13**(2): p. 162-169.
65. Zhang, X., Y. Zhou, and M. Ezawa, *Magnetic bilayer-skyrmions without skyrmion Hall effect*. Nature communications, 2016. **7**(1): p. 1-7.
66. Barker, J. and O.A. Tretiakov, *Static and dynamical properties of antiferromagnetic skyrmions in the presence of applied current and temperature*. Physical review letters, 2016. **116**(14): p. 147203.
67. Legrand, W., et al., *Room-temperature stabilization of antiferromagnetic skyrmions in synthetic antiferromagnets*. Nature materials, 2020. **19**(1): p. 34-42.

68. Zhou, Y. and M. Ezawa, *A reversible conversion between a skyrmion and a domain-wall pair in a junction geometry*. Nature communications, 2014. **5**: p. 4652.
69. Jiang, W., et al., *Blowing magnetic skyrmion bubbles*. Science, 2015. **349**(6245): p. 283-286.
70. Yu, G., et al., *Room-temperature skyrmion shift device for memory application*. Nano letters, 2016. **17**(1): p. 261-268.
71. Zhang, X., et al., *Skyrmion-skyrmion and skyrmion-edge repulsions in skyrmion-based racetrack memory*. Scientific reports, 2015. **5**: p. 7643.
72. Wang, X., et al., *Current-induced skyrmion motion on magnetic nanotubes*. Journal of Physics D: Applied Physics, 2019. **52**(22): p. 225001.
73. Hamamoto, K., M. Ezawa, and N. Nagaosa, *Purely electrical detection of a skyrmion in constricted geometry*. Applied Physics Letters, 2016. **108**(11): p. 112401.
74. Crum, D.M., et al., *Perpendicular reading of single confined magnetic skyrmions*. Nature communications, 2015. **6**(1): p. 1-8.
75. Maccariello, D., et al., *Electrical detection of single magnetic skyrmions in metallic multilayers at room temperature*. Nature nanotechnology, 2018. **13**(3): p. 233-237.
76. Zhang, X., M. Ezawa, and Y. Zhou, *Magnetic skyrmion logic gates: conversion, duplication and merging of skyrmions*. Sci Rep, 2015. **5**: p. 9400.
77. Xing, X., P.W. Pong, and Y. Zhou, *Skyrmion domain wall collision and domain wall-gated skyrmion logic*. Physical Review B, 2016. **94**(5): p. 054408.
78. He, Z., S. Angizi, and D. Fan, *Current-induced dynamics of multiple skyrmions with domain-wall pair and skyrmion-based majority gate design*. IEEE Magnetics Letters, 2017. **8**: p. 1-5.
79. Wang, X., et al., *Efficient skyrmion transport mediated by a voltage controlled magnetic anisotropy gradient*. Nanoscale, 2018. **10**(2): p. 733-740.
80. Zhang, Z., et al., *Skyrmion-based ultra-low power electric-field-controlled reconfigurable (SUPER) logic gate*. IEEE Electron Device Letters, 2019. **40**(12): p. 1984-1987.
81. Walker, B.W., et al., *Skyrmion logic clocked via voltage-controlled magnetic anisotropy*. Applied Physics Letters, 2021. **118**(19): p. 192404.
82. Luo, S., et al., *Reconfigurable skyrmion logic gates*. Nano letters, 2018. **18**(2): p. 1180-1184.
83. Chauwin, M., et al., *Skyrmion logic system for large-scale reversible computation*. Physical Review Applied, 2019. **12**(6): p. 064053.
84. Song, M., et al., *Logic device based on skyrmion annihilation*. IEEE Transactions on Electron Devices, 2021. **68**(4): p. 1939-1943.
85. Li, S., et al., *Magnetic skyrmion-based artificial neuron device*. Nanotechnology, 2017. **28**(31): p. 31LT01.
86. Huang, Y., et al., *Magnetic skyrmion-based synaptic devices*. Nanotechnology, 2017. **28**(8): p. 08LT02.
87. Prychynenko, D., et al., *Magnetic skyrmion as a nonlinear resistive element: a potential building block for reservoir computing*. Physical Review Applied, 2018. **9**(1): p. 014034.
88. Song, K.M., et al., *Skyrmion-based artificial synapses for neuromorphic computing*. Nature Electronics, 2020. **3**(3): p. 148-155.
89. Liang, X., et al., *Antiferromagnetic skyrmion-based logic gates controlled by electric currents and fields*. Applied Physics Letters, 2021. **119**(6): p. 062403.
90. Cheghabouri, A.M. and M.C. Onbasli, *Direct current-tunable MHz to multi-GHz skyrmion generation and control*. Scientific Reports, 2019. **9**(1): p. 9496.
91. Cheghabouri, A.M., F. Katmis, and M.C. Onbasli, *Cascadable direct current*

driven skyrmion logic inverter gate. Physical Review B, 2022. **105**(5): p. 054411.
92. Arash Mousavi Cheghabouri, M.C.O. *Domain Wall-Gated, Cascaded and Low-Power Skyrmion Logic Gates with Robust Operation*. in *2022 Joint MMM-INTERMAG*. 2022. Underline Science Inc.
93. Onbasli, M.C. and A. Mousavi Cheghabouri. *Paving the way for Boolean logic by skyrmion based programmable logic devices*. in *APS March Meeting Abstracts*. 2022.
94. Onbasli, M.C., A. Mousavi Cheghabouri, and F. Katmis, *The Effect of Polycrystallinity on Skyrmion Logic Devices*. Bulletin of the American Physical Society, 2023.
95. Onbaşli, M.C., et al., *Theory and Modeling of Spintronics of Nanomagnets*, in *Fundamentals of Low Dimensional Magnets*. 2023, CRC Press. p. 325-342.
96. Richardson, O.W., *A mechanical effect accompanying magnetization*. Physical Review (Series I), 1908. **26**(3): p. 248.
97. Einstein, A., *Experimenteller nachweis der ampereschen molekularströme*. Naturwissenschaften, 1915. **3**(19): p. 237-238.
98. Einstein, A. and W. De Haas, *Experimental proof of the existence of Ampère's molecular currents*. Koninklijke Nederlandse Akademie van Wetenschappen Proceedings Series B Physical Sciences, 1915. **18**: p. 696-711.
99. Barnett, S.J., *Magnetization by rotation*. Physical review, 1915. **6**(4): p. 239.
100. Stancil, D.D. and A. Prabhakar, *Spin waves*. Vol. 5. 2009: Springer.
101. Russell, H.N. and F.A. Saunders, *New regularities in the spectra of the alkaline earths*. The Astrophysical Journal, 1925. **61**: p. 38.
102. Landé, A., *Über den anomalen Zeemaneffekt (Teil I)*. Zeitschrift für Physik, 1921. **5**(4): p. 231-241.
103. Gilbert, T. and J. Kelly. *Anomalous rotational damping in ferromagnetic sheets*. in *Conf. Magnetism and Magnetic Materials, Pittsburgh, PA*. 1955.
104. Gilbert, T.L., *A phenomenological theory of damping in ferromagnetic materials*. IEEE transactions on magnetics, 2004. **40**(6): p. 3443-3449.
105. Weiss, P., *Hypothesis of the molecular field and ferromagnetic properties*. J. phys, 1907. **4**(6): p. 661-690.
106. Van Vleck, J.H., *The theory of electric and magnetic susceptibilities*. 1965: Oxford University Press.
107. Ising, E., *Beitrag zur theorie des ferro-und paramagnetismus*. 1924, Grefe & Tiedemann.
108. Dirac, P.A. *The quantum theory of the electron*. in *Proceedings of the Royal Society of London A: Mathematical, Physical and Engineering Sciences*. 1928. The Royal Society.
109. Heisenberg, W., *Mehrkörperproblem und Resonanz in der Quantenmechanik*. Zeitschrift für Physik, 1926. **38**(6): p. 411-426.
110. Dzyaloshinsky, I., *A thermodynamic theory of "weak" ferromagnetism of antiferromagnetics*. Journal of Physics and Chemistry of Solids, 1958. **4**(4): p. 241-255.
111. Moriya, T., *Anisotropic superexchange interaction and weak ferromagnetism*. Physical Review, 1960. **120**(1): p. 91.
112. Akulov, N., *Zur theorie der magnetisierungskurve von einkristallen*. Zeitschrift für Physik, 1931. **67**(11): p. 794-807.
113. Kronmüller, H., *General micromagnetic theory*. Handbook of Magnetism and Advanced Magnetic Materials, 2007.
114. Zhang, S. and Z. Li, *Roles of nonequilibrium conduction electrons on the magnetization dynamics of ferromagnets*. Physical review letters, 2004. **93**(12): p. 127204.

115. Vansteenkiste, A., et al., *The design and verification of MuMax3*. AIP advances, 2014. **4**(10): p. 107133.
116. Donahue, M.J. and M. Donahue, *OOMMF user's guide, version 1.0*. 1999.
117. Ezawa, M., *Giant skyrmions stabilized by dipole-dipole interactions in thin ferromagnetic films*. Physical review letters, 2010. **105**(19): p. 197202.
118. Yu, X., et al., *Magnetic stripes and skyrmions with helicity reversals*. Proceedings of the National Academy of Sciences, 2012. **109**(23): p. 8856-8860.
119. Chen, G., et al., *Out-of-plane chiral domain wall spin-structures in ultrathin in-plane magnets*. Nature communications, 2017. **8**: p. 15302.
120. Pappas, C., et al., *Chiral paramagnetic skyrmion-like phase in MnSi*. Physical review letters, 2009. **102**(19): p. 197202.
121. Neubauer, A., et al., *Topological Hall effect in the A phase of MnSi*. Physical review letters, 2009. **102**(18): p. 186602.
122. Moreau-Luchaire, C., et al., *Additive interfacial chiral interaction in multilayers for stabilization of small individual skyrmions at room temperature*. Nature nanotechnology, 2016. **11**(5): p. 444.
123. Boulle, O., et al., *Room-temperature chiral magnetic skyrmions in ultrathin magnetic nanostructures*. Nature nanotechnology, 2016. **11**(5): p. 449.
124. Das, S., et al., *Observation of room-temperature polar skyrmions*. Nature, 2019. **568**(7752): p. 368.
125. Iwasaki, J., M. Mochizuki, and N. Nagaosa, *Universal current-velocity relation of skyrmion motion in chiral magnets*. Nature communications, 2013. **4**: p. 1463.
126. Schulz, T., et al., *Emergent electrodynamics of skyrmions in a chiral magnet*. Nature Physics, 2012. **8**(4): p. 301.
127. Fook, H.T., W.L. Gan, and W.S. Lew, *Gateable skyrmion transport via field-induced potential barrier modulation*. Scientific reports, 2016. **6**: p. 21099.
128. Milde, P., et al., *Unwinding of a skyrmion lattice by magnetic monopoles*. Science, 2013. **340**(6136): p. 1076-1080.
129. Kortright, J.B., et al., *Soft-x-ray small-angle scattering as a sensitive probe of magnetic and charge heterogeneity*. Physical Review B, 2001. **64**(9): p. 092401.
130. Woo, S., et al., *Spin-orbit torque-driven skyrmion dynamics revealed by time-resolved X-ray microscopy*. Nature communications, 2017. **8**: p. 15573.
131. Pollard, S.D., et al., *Observation of stable Néel skyrmions in cobalt/palladium multilayers with Lorentz transmission electron microscopy*. Nature communications, 2017. **8**: p. 14761.
132. Woo, S., et al., *Current-driven dynamics and inhibition of the skyrmion Hall effect of ferrimagnetic skyrmions in GdFeCo films*. Nature communications, 2018. **9**(1): p. 959.
133. Purnama, I., et al., *Guided current-induced skyrmion motion in 1D potential well*. Scientific reports, 2015. **5**: p. 10620.
134. Jin, C., et al., *Dynamics of antiferromagnetic skyrmion driven by the spin Hall effect*. Applied Physics Letters, 2016. **109**(18): p. 182404.
135. Kang, S., et al., *The spin structures of interlayer coupled magnetic films with opposite chirality*. Scientific reports, 2018. **8**(1): p. 2361.
136. Kang, W., et al., *Skyrmion-electronics: an overview and outlook*. Proceedings of the IEEE, 2016. **104**(10): p. 2040-2061.
137. Romming, N., et al., *Writing and deleting single magnetic skyrmions*. Science, 2013. **341**(6146): p. 636-639.
138. Yuan, H. and X. Wang, *Skyrmion creation and manipulation by nano-second current pulses*. Scientific reports, 2016. **6**: p. 22638.

139. Nakatani, Y., et al., *Electric field control of Skyrmions in magnetic nanodisks*. Applied Physics Letters, 2016. **108**(15): p. 152403.
140. Heinonen, O., et al., *Generation of magnetic skyrmion bubbles by inhomogeneous spin Hall currents*. Physical Review B, 2016. **93**(9): p. 094407.
141. Beach, G., M. Tsoi, and J. Erskine, *Current-induced domain wall motion*. Journal of magnetism and magnetic materials, 2008. **320**(7): p. 1272-1281.
142. Büttner, F., I. Lemesh, and G.S. Beach, *Theory of isolated magnetic skyrmions: From fundamentals to room temperature applications*. Scientific reports, 2018. **8**(1): p. 4464.
143. Wang, X., H. Yuan, and X. Wang, *A theory on skyrmion size*. Communications Physics, 2018. **1**(1): p. 1-7.
144. Gong, X., H. Yuan, and X. Wang, *Current-driven skyrmion motion in granular films*. Physical Review B, 2020. **101**(6): p. 064421.
145. Kim, J.-V. and M.-W. Yoo, *Current-driven skyrmion dynamics in disordered films*. Applied Physics Letters, 2017. **110**(13): p. 132404.